Title
Femtosecond Velocity Map Imaging of Atomic and Molecular Dynamics

Author
Doughty, Benjamin Lee

Publication Date
2010

Peer reviewed|Thesis/dissertation

Femtosecond Velocity Map Imaging of Atomic and Molecular Dynamics

by

Benjamin Lee Doughty

A dissertation submitted in partial satisfaction of the

requirements for the degree of

Doctor of Philosophy

in

Chemistry

in the

Graduate Division

of the

University of California, Berkeley

Committee in charge:

Professor Stephen R. Leone, Chair

Professor Daniel M. Neumark

Professor Dmitry Budker

Fall 2010

Femtosecond Velocity Map Imaging of Atomic and Molecular Dynamics

Abstract

Femtosecond Velocity Map Imaging of Atomic and Molecular Dynamics

by

Benjamin Lee Doughty

Doctor of Philosophy in Chemistry

University of California, Berkeley

Professor Stephen R. Leone, Chair

Excited state photoelectron angular distributions (PADs) are measured in two-color two-photon ionization experiments on autoionizing resonances in atomic and molecular targets. Atomic krypton is excited to $4s^1 4p^6 6p^1$ configurations, which decay on the femtosecond timescale. By ionizing these states with a delayed 801 nm probe pulse, the population decay and photoionization dynamics are simultaneously measured directly and in real time. In the case of the $4s^1 4p^6 6p^1$ excitation, two slightly split $J = 1$ autoionizing states are populated, one with a singlet multiplicity and the other a triplet. A novel approach to separate the overlapping resonance contributions to the total PAD is demonstrated using femtosecond time-resolution to isolate the individual PADs of each state by way of their different autoionization lifetimes. The measured PAD for the singlet state is decomposed into the ratio of radial dipole matrix elements and relative phase difference between the two states. The triplet PADs are predicted to result in anisotropies independent of the nature of the atom or excited state from which the detected electron originates. Measurement of the anisotropy from this state shows a significant deviation from the predictions, which is most likely a result of configuration mixing from Fano and spin-orbit interactions. In another set of experiments, transiently populated superexcited states (SESs) in molecular oxygen are prepared and probed by 805 nm pulses as the autoionization and predissociation relaxation channels compete. Three neutral product channels are detected and formed on the femtosecond time scale, assigned as predissociation products of different vibrational SESs. The decay lifetime of the $v = 1$ SES agrees excellently with lifetimes extracted from high-resolution experiments that probe the ionic core spectral line widths of the vibrational levels. Results also reveal a long lived state that is unassigned and whose spectroscopic signature is observed as a depletion in the autoionization signal by the 805 nm probe up to several hundred picosecond time delays. Future work is needed to identify this feature.

To my family

Contents

List of Figures

List of Tables

Acknowledgments

Reflecting on the years spent in graduate school and all that has been worked on, the constant challenges of experimental science, and the moments of frantic data collection I immediately think of the numerous people who were there to help me through it all. My thoughts are drawn foremost to my graduate advisor Stephen R. Leone whose immeasurable guidance and patience has made an everlasting impression on me. The work presented in this thesis would not have been possible without him and the opportunities he has given me. I am eternally grateful to him for setting such an excellent example of what a scientist should be in the lab and as a person.

I would like to thank Louis Haber for patiently teaching me the nitty-gritty of experimental physical chemistry. Louis is a scientist I look up to and is a continual source of reference, inspiration, and friendship. Daniel Strasser significantly motivated many of the adaptations and improvements to the experiment such that a new realm of experimental possibilities has opened up for exploration. I have a deep appreciation for his critical approach to science; it has made me think through problems before rushing into solve them and has made me a better scientist because of it. I have had the pleasure to work with a talented young undergraduate researcher, Christina (Tina) Hackett. I have learned so much by working with her and I hope she has taken the same experiences and knowledge from lab work that I did when I was in her shoes. I am excited to think of the future directions Christine Koh is taking this experiment. I have complete confidence the experiment will blossom under her care.

Zhi-Heng 'don't tell me your problems' Loh has served as a scientific sounding board since moving to campus. He is a wealth of knowledge that will be missed and always appreciated. Phillip Nagel was the best office mate I could have asked for and a great friend throughout the years. I will always look back on House runs and scientific discussions with fondness. Naturally, this invokes memories and appreciation of numerous people working at Lawrence Berkeley National Lab that I have had the pleasure of interacting with. This includes Oliver Gessner, Oleg Kornilov, Mark Abel, Thomas Pfeifer, Kyungwon Kwak, and Andy Caughey. After my lab was relocated to the UC Berkeley campus I had the opportunity to befriend and learn from Amy Cordones, Erik Hosler, Teresa Bixby, and Allison Pymer. Lunch breaks to House of Bolts were always pleasurable... when they remembered to get me. I cannot forget the administrative help of Kathleen Fowler, Adam Bradford, and Mary Holloway who helped wade through the seas of paperwork which allowed me to focus on my experiments.

Tessa Calhoun is the source of my sanity. I never would have dreamed that going to graduate school would lead me to the woman of my dreams. I cannot thank Tessa enough for putting up with me all these years. I must also credit her for showing me the good and the bad of LaTeX, the program with which this thesis was compiled. Greg Dallinger, my former roommate and great friend, has always lightened the atmosphere and made graduate school a little more fun. I will always remember the late night

homework collaborations our first year. Kami Myers should also be acknowledged here as she is really the reason I even applied to Berkeley. I could not ask for a better friend.

I would also like to thanks Professor Martin Vala at the University of Florida who pulled the necessary strings to get me into Berkeley and started me down the path of experimental physical chemistry. While at Berkeley I have had the pleasure to work closely with Eric Granlund in the College of Chemistry machine shop in designing and constructing a new front end of the experiment upon moving to campus. The numerous talented workers in the wood and electrical shops are largely responsible for the short downtime after moving the instrument to campus. Dennis Merritt of Spectra Physics has helped solve numerous technical issues with the laser system used in the experiments performed. My family has supported me throughout the years and should also be acknowledged here for their efforts. I would finally like to thank Professor Daniel Neumark and Dmitry Budker for taking time out of their busy schedules to serve on my qualifying exam and thesis committees.

Chapter 1

Introduction

Photoelectron spectroscopy is a powerful tool to probe the electronic structure of gaseous, liquid and solid targets. It has proven to be an exceptionally intuitive means to test theories of atomic orbitals, molecular bonding, and band structure.[1–6] In the most general photoelectron experiments, light is allowed to interact with a sample that subsequently ejects an electron into the continuum and is then measured by some means. The process is described mathematically by the simple relation

$$E_K = h\nu - E_B \tag{1.1}$$

where E_K is the ejected electron kinetic energy, $h\nu$ is the incident photon energy, and E_B is the binding energy of the electron in the sample. Information on the electronic structure of the target is contained in the electron binding energy, which is measured in experiments using monochromatic light of known frequency to eject electrons with a measured kinetic energy. This is depicted in Figure 1.1 for the simplest case of discrete energy levels ionized to a single final electron continuum.

In this instance, the electronic structure of the system is directly probed by observation of the electron kinetic energy. Information pertaining to excited ion states of the system can be simultaneously obtained, allowing for the determination of the energetic location of resonances in two charge states. While the measurement of the photoelectron spectrum is a powerful tool to dissect the energetics of a system; simultaneous determination of the angular distribution of the ejected photoelectrons allows for even more insight into the electronic structure of the target and the dynamics of photo-ionization. For an ionization process with linearly polarized light the photoelectron angular distribution (PAD) can be written as an expansion of Legendre polynomials in the form[7–9]

$$I(\theta) = \sum_{K=0}^{N} C_{2K} P_{2K}(cos\theta) \tag{1.2}$$

where $I(\theta)$ is the photoelectron intensity as a function of angle relative to the light polarization, N is the number of photons contributing to the ionization process, C_{2K}

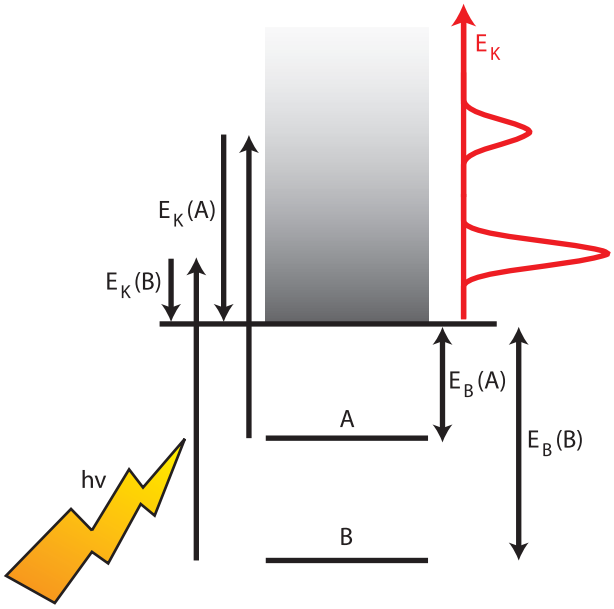

Figure 1.1: The principle of photoelectron spectroscopy is shown here. An incident photon with known energy, $h\nu$, interacts with a bound state electron ejecting it into the final continuum. The excess energy is imparted to the electron in the form of kinetic energy, E_K, which is the experimental observable. From the relation given in Eq. 1.1 the binding energy, E_B, of the discrete state is determined, which yields the electronic structure of the target.

are expansion coefficients, which contain information on the photoionization process, and P_{2K} are Legendre polynomials of order $2K$ as a function of the $cos\theta$. In the case of single photon ionization of a randomly oriented atomic target the PAD reduces to the form[7]

$$I(\theta) = C_0 P_0(cos\theta) + C_2 P_2(cos\theta) \tag{1.3}$$

which reduces further to

$$I(\theta) = \frac{\sigma}{4\pi}\left[1 + \beta_2 P_2(cos\theta)\right] \tag{1.4}$$

It is clear that the PAD in this instance is dependent on a single parameter, β_2, which is known as an anisotropy parameter. In the limit that the ionized electron experiences a symmetric potential upon leaving the ionic core, the anisotropy parameter is expressed as[9]

$$\beta_2 = \frac{l(l+1)D_{l-1}^2 + (l+1)^2 D_{l+1}^2 - 6l(l+1)D_{l+1}D_{l-1}cos\Delta}{(2l+1)(lD_{l-1}^2 + (l+1)D_{l+1}^2}. \tag{1.5}$$

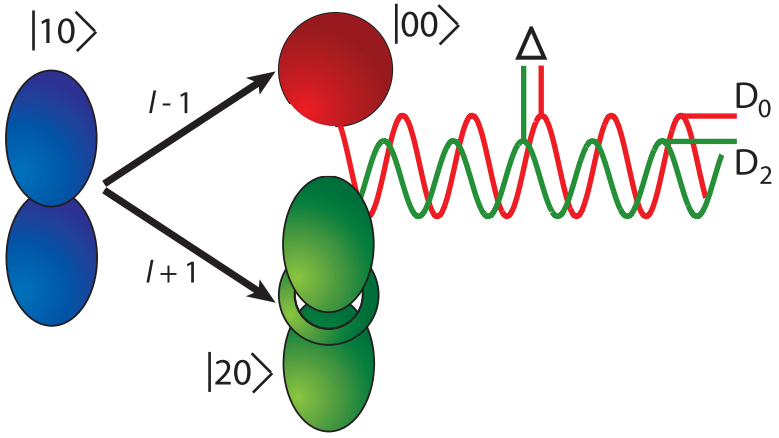

Figure 1.2: An illustration of the interference of outgoing partial waves in the final continuum that result in the PAD. In this case a P_z orbital (ie: $|lm\rangle = |10\rangle$) is ionized according to the $\Delta l \pm 1$ LS-coupling selection rules to $|20\rangle$ and $|00\rangle$ continuum partial waves (D and S waves, respectively). The difference in amplitude is a result of the radial dipole matrix elements, $D_{l\pm1}$, for S and D wave ionization. A phase shift between the two is a result of Coulomb phase shifts and scattering phase shifts of the different l partial waves.

Here, $D_{l\pm1}$ are radial dipole matrix elements connecting states with initial orbital angular momentum, l, to an outgoing electron partial wave with $l \pm 1$, and Δ is the total phase shift difference between the two possible outgoing photoelectron partial waves. The radial transition dipole matrix element is built from initial and final radial wavefunctions given by R_l and $R_{l\pm1}$, respectively, coupled by the electric field of the light with the transition dipole of the system and is given by

$$D_{l\pm1} = \langle R_{l\pm1} | e \cdot r | R_l \rangle \,. \tag{1.6}$$

The total phase shift difference is composed of two contributions: the Coulomb phase shift and the scattering phase shift. The third term in the numerator of Eq. 1.5 represents the interference of the two coherent outgoing electron partial waves. This is shown schematically in Figure 1.2. Here the two partial waves have different amplitudes determined by the transition dipole matrix elements. The phase shift between the two waves influences significantly the interference that is measured in the final PAD. The determination of these parameters represents a near complete determination of the photoionization dynamics.

In single photon ionization experiments, this microscopic information cannot typically be determined since a single anisotropy parameter contains several unknown quantities. However, the use of multiple photons to excite and ionize the system introduces an inherent alignment to the ensemble of targets and in some cases permits the determination of the ratio of radial dipole matrix element and phase shift difference

between the partial waves. Of particular interest is the angular distributions from a two photon ionization which is given by

$$I(\theta) = \frac{\sigma}{4\pi}\left[1 + \beta_2 P_2(cos\theta) + \beta_4 P_4(cos\theta)\right] \tag{1.7}$$

which at a glance seems to only add complexity by inclusion of higher order anisotropy parameters. However, several additional experimental observables become available, which permits the determination of the ratio of radial dipole matrix elements and the phase shift. For instance, in a two photon ionization experiment the frequency of the two photons can be different, allowing one to excite (or pump) various resonances, which may or may not be aligned. These states are then ionized (or probed) to eject electrons from the excited configuration. These electrons carry with them information about the excited state electronic character and the continuum to which the electrons are born. This includes influences on the excited state PADs by configuration and spin-orbit interactions.[7,10–26] Relaxation dynamics can be simultaneously measured when the probe photon is delayed in time. This allows for an in depth understanding of not only the photoionization dynamics, but also the relaxation dynamics of the excited state. By changing the frequency of the ionizing light the energy dependence of the dipole matrix elements and phase shifts can be measured and used to scrutinize theoretical models of photoionization.[7,22–24,27–29]

The experiments presented here are focused on preparing short lived excited states in atomic and molecular species with femtosecond pulses of extreme ultraviolet (EUV) light. The resulting photodynamics are investigated by measuring the PADs with a second femtosecond laser pulse that is delayed in time. This allows for the retrieval of the microscopic parameters that characterize photoionization while simultaneously tracking the excited state decay channels in real time. This includes preparation and ionization of autoionizing resonances in atomic krypton. The determination of the ratio of radial dipole matrix elements connecting the excited state to the final continuum partial waves and the phase shift difference between these waves is extracted in singlet $4s^1 4p^6 6p^1$ Rydberg states. In instances where LS-coupling selection rules break down, triplet states with the same electronic configuration are excited and aligned, which yield anisotropy parameters that deviate from predicted values in a single configuration model. This highlights the importance of configuration mixing in the intermediate and final states, as they contribute to the excited state decay and the resulting PADs. These excitations in krypton will be discussed in Chapters 3. Finally, the study of autoionizing states in atoms is extended to superexcited states in molecular oxygen where the purely electronic autoionization channel is competitive with neutral predissociation. This represents an opportunity to probe non-Born-Oppenheimer dynamics with temporal, energetic and angular resolution to track the photo-reaction as it evolves to yield a set of photo-products. The lifetimes of the excited states and the nascent neutral products formed by these states are discussed in an ion-core model of photodissociation and will be outlined in Chapter 4.

Chapter 2

Experimental Principles

2.1 Introduction

This chapter will address the experimental apparatus used to prepare and probe transiently excited atoms and molecules. To begin, aspects of the electronic structure of autoionizing excited states will be reviewed in the first sections. The static spectroscopy and terminology typically used to characterize autoionizing resonances and some theoretical framework will be considered first. The invaluable information extracted from these measurements and theories lay the foundation for pump-probe experiments. The decay of superexcited molecules is also briefly addressed as an extension of the kinetics of autoionization in atoms.

The preparation of the autoionizing states by a single high-energy photon allows for a well-defined excited state to be prepared and subsequently probed. This is accomplished by high-order harmonic generation with a tunable near-IR femtosecond laser. In this section, the layout of the experiment will be given and the apparatus characterized.

Finally, the detection scheme used to simultaneously measure the excited state decay processes, photoelectron kinetic energies and angular distributions is described. Event-counting velocity map imaging is discussed and its implementation is described. Single photon ionizations of rare gas atoms will then be considered as a reference for energy calibrations and to confirm the accuracy of the measured PADs. Finally, the temporal characteristics of the instrument are studied in resonant two-photon ionization of atomic helium.

2.2 Spectra and Dynamics of Autoionizing Resonances

High-resolution optical spectroscopy allows for the accurate characterization of excited atomic and molecular states. This includes obtaining information about the

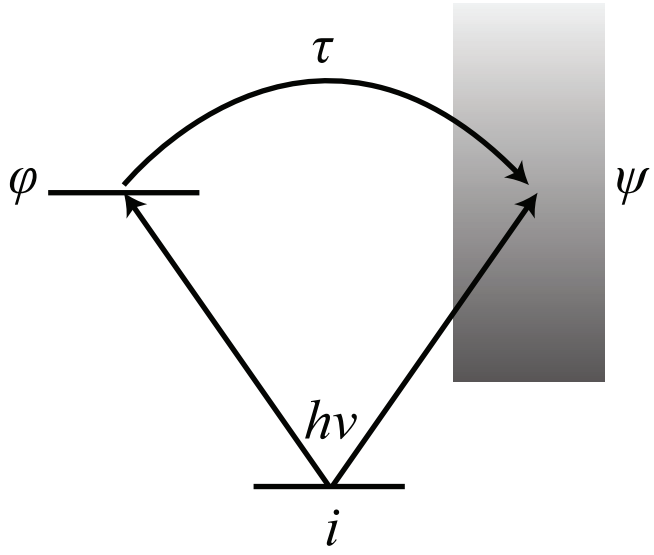

Figure 2.1: The ground state target, i, is excited with a photon of energy, $h\nu$, to simultaneously populate a discrete state, ϕ, and a width of continuum states, ψ, that are coupled. The modified discrete state autoionizes with a lifetime of τ. Since both channels evolve to the same final state, interferences are observed and manifested as asymmetric line shapes.

energies of excited states and cross sections and estimating perturbations on the resonances from nearby levels.[12–14,16,21,25,30–32] One can also infer dynamics from the measured spectra in great detail. For the absorption of light by an atomic system below the ionization threshold the spectral line shapes are Lorentzian. The width of these spectral lines represents the lifetime of the states as given by the uncertainty relation

$$\Delta E \Delta t \geq \hbar \tag{2.1}$$

where Δt corresponds to the lifetime of the state, ΔE is the spectral width of the absorption line and $\hbar$ is Planck's constant scaled by 2π. In the case of states that relax via fluorescence, the lifetimes are quite long (on the order of nanoseconds) such that the line widths are very narrow. When the frequency of light is tuned above the ionization threshold to populate a resonance embedded in the continuum, the state may autoionize to the continuum as depicted in Figure 2.1. In this case, the line shape is no longer observed to be Lorentzian, but rather takes on a peculiar asymmetric line shape. These resonances are also much broader and typically do not fluoresce. This is understood by considering the competitive relaxation channels available to the atomic state, specifically, autoionization versus fluorescence relaxation. The excited

state lifetime is written as

$$\frac{1}{\tau_{obs}} = \frac{1}{\tau_{ai}} + \frac{1}{\tau_{fl}}. \tag{2.2}$$

Here, the observed lifetime of the autoionizing resonance, τ_{obs}, is given as the sum of the inverse lifetimes for each decay pathway. Autoionization lifetimes, τ_{ai}, are often on the order of picoseconds to attoseconds[14,16,30–32] whereas the fluorescence lifetime, τ_{fl}, is on the order of hundreds of picoseconds to nanoseconds. The large differences in timescales of the two processes preclude fluorescence channels to contribute to the relaxation dynamics of the systems described here.

The line shapes of autoionizing resonances are described by configuration mixing of bound and continuum wavefunctions as described in the work of Fano.[14,16] In this theory, the resonant state is modified by an admixture of continuum states. This is described in the equation

$$\Phi = \phi + P \int dE' \frac{V_{E'} \psi_{E'}}{E - E'} \tag{2.3}$$

where Φ is the observable modified discrete state, ϕ is the unobserved pure discrete state before mixing with the continuum, $V_{E'}$ is the coupling strength between the discrete and continuum channels given as $\langle \phi | H | \psi_E \rangle$, and $\psi_{E'}$ are the continuum waves that are mixed in. It is the configuration interaction that mixes in neighboring states, including the continuum. The integral is a principle part integral as denoted by P. In writing the autoionizing states as an admixture, the line shape can be parameterized into observable parts, all of which yield insight into the resonance. The line shape is conveniently written as

$$I(\varepsilon) = \frac{(q + \varepsilon)^2}{1 + \varepsilon^2}. \tag{2.4}$$

The spectral line shape is given by $I(E)$ where q is the dimensionless Fano parameter (or profile index), $\varepsilon = 2(E - E_r - \delta E)/\Gamma$, and $\Gamma = 1/\tau_{ai}$, where E, E_r, δE, Γ and τ_{ai} are the excitation photon energy, resonance energy, energy shift of the resonant state, the spectral line width, and the autoionization lifetime, respectively. The δE parameter physically represents the shift in resonance energy relative to the unmodified state resonance energy. The profile index is given by

$$q = \frac{\langle \Phi | e \cdot r | i \rangle}{\pi \langle \phi | H | \psi_E \rangle \langle \psi_E | e \cdot r | i \rangle} \tag{2.5}$$

where, as before, $e \cdot r$ is the transition dipole operator, $|i\rangle$ is the ground state of the system. The q-parameter dictates the interference and line shape that is measured. A low value of q results in cross sections that are smaller than the off resonant direct ionization. These are characterized as window resonances as the transmission of light at these energies is greater than when off resonant. As q increases in magnitude, the interaction between the channels goes to zero and the line shape results in a

Lorentzian profile. Intermediate values of q give asymmetric line shapes with dips in the cross section on either side of the resonance depending on the sign. Several examples are given in Figure 2.2.

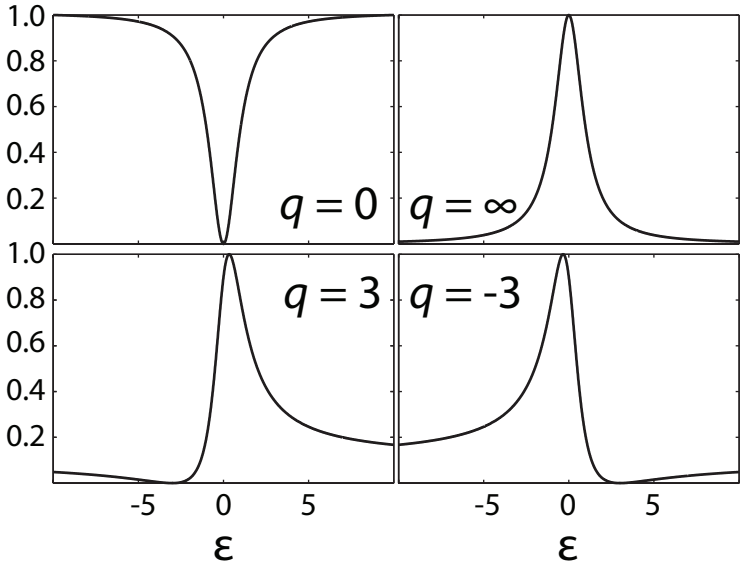

Figure 2.2: Various Fano lineshapes plotted versus ε for representative values of the Fano profile index, q

The results of a static absoption measurement typically fit the spectrum to this line shape, which can in principle completely characterize the excitation and decay. However, in densely packed spectral regions it is often difficult to distinguish between resonances.[12,21,31,32] To address this, parameterizations have been developed that fit the spectra of overlapping and interacting resonances. A popular parameterization is the Shore parameterization given by[30]

$$\sigma(E) = C(E) + \sum_{i}^{n} \frac{(E - E_i)(\Gamma_i/2)a_i + (\Gamma_i/2)^2 b_i}{(E - E_i)^2 + (\Gamma_i/2)^2}. \tag{2.6}$$

In this parameterization the cross section as a function of excitation energy, $\sigma(E)$, is expanded over n resonances. The total background cross section away from the autoionizing resonance is given by $C(E)$, the coefficients a_i and b_i are proportional to the products of dipole and Coulomb matrix elements connecting the ground state to the continuum and modified discrete state, respectively. The spectral width of the i^{th} state is Γ_i while the excitation energy of the state is E_i. Equation 2.6 reduces to a Fano line shape for an isolated resonance.

This form of the cross section necessarily requires high spectral resolution and the resonance energy spacing between states needs to be large enough that each can be

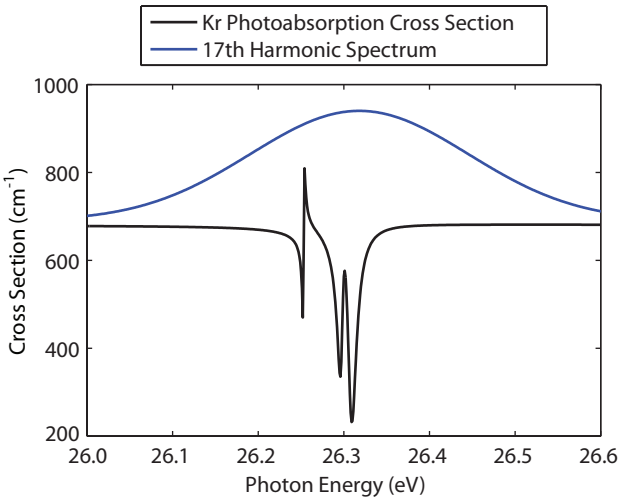

Figure 2.3: The photoexcitation cross section as a function of photon energy is illustrated as the black trace. The 17^{th} harmonic spectrum is overlaid in blue to show the region of excitation used in later experiments.

resolved. In cases where overlapping states cannot be resolved, inaccurate line widths and energies are extracted.[21] An example of this cross section parameterization is given in Figure 2.3 for excitation of atomic krypton to the $4s^1 4p^6 6p^1$ configurations as described by the experimental values obtained by Ederer.[12]

Measuring these features in real time with pump-probe techniques allows for a more direct determination of the lifetimes of the excited states by fitting the transient signal to a simple kinetic model. This results in fewer adjustable parameters in the fit and in some cases can improve the spectral separation of nearby states by probing them to different continua that are spectrally well resolved. The excited state is composed of admixtures of continuum and other nearby resonances. The composition of the excited state is reflected in the PADs from these states as will be discussed in Chapter 3. Thus, by exciting and probing autoionizing resonances with femtosecond time-resolution, the determination of the excitation, decay, and photoionization dynamics are measured.

2.2.1 Molecular Superexcited States

Within the framework of the Born-Oppenheimer approximation the nuclear motions are forced to track adiabatically on the surfaces defined by the electronic motions. In other words, nuclear motion is much slower than electronic motion, thus to a reasonable approximation, all the dynamics are governed by the electrons. As time-resolution has improved in experimental systems, this approximation is found to satisfy fewer and fewer situations. A realm of chemical dynamics known as non-

adiabatic dynamics is at the forefront of explorations in many femtosecond and attosecond laboratories. This includes the probing of conical intersections (molecular potential funnels), which are now thought to dominate excited state relaxations as a replacement for avoided-crossings in polyatomic molecules.[33,34] In the case of diatomic molecules, conical intersections are not possible due to the low dimensionality of the system, but highly excited states still show a breakdown of the Born-Oppenheimer approximation. This is apparent when molecular autoionizing states are excited. Often, neutral dissociation products are measured in addition to the autoionization product channel. These resonances are called superexcited states (SES). They are neutral excited states located energetically well above the ionization threshold.

The dynamics of these states differ from atomic measurements because at least one additional channel contributes to the total lifetime of the state. A modification to Equation 2.2 yields

$$\frac{1}{\tau_{obs}} = \frac{1}{\tau_{ai}} + \frac{1}{\tau_{nd}} + \frac{1}{\tau_{fl}} \tag{2.7}$$

where τ_{nd} is the dissociation lifetime for the neutral product. The mechanism and lifetime for the decay of these states is debated.[35–41] Some results suggest a slower predissociation mechanism, while others point to a fast cascading predissociation over many surfaces to form several neutral products. This problem is well suited for a time-resolved experiment to probe the excited state as it decays into neutral fragments and autoionizes. The measured rates of product formation from a time-resolved experiment can lend insight and help to address the difficulties encountered with aspects of static measurements. SESs in molecular oxygen are addressed in Chapter 4.

2.3 Optical Pumping of Highly Excited States

2.3.1 Principles

The optical excitation of autoionizing and superexcited resonances follow dipole selection rules. In the case of krypton, LS-coupling is not a good approximation for the excited states; instead J, M_J and parity, Π, govern the allowed transitions. All allowed transitions must have $\Delta J = 0, \pm 1$; for linearly polarized light $\Delta M_J = 0$. The parity of a photon is $\Pi_{h\nu} = -1$ (ie: it is odd) which requires that the parity of the state must change upon absorption of a photon.

The ground state of krypton is described in LS-coupling as a $^1S_0$. One-photon selection rules require that the excited state have $J = 1$, $M_J = 0$, and $\Pi_{ex} = -1$. The excited states in krypton relevant to the experiments presented here are are described in jj-coupling. In jj-coupling the j for each electron is considered rather than the total L or S. The individual j's are coupled to give the total angular momentum, J. These states are written as $(j_c, j_e)_J$. The electronic configuration

$4s^1 4p^6 6p^1$ has $j_c = 1/2$ for the core $4s^1$ electron. The $6p^1$ electron can have $j_e = 1/2$ and $j_e = 3/2$. The two possible ways to make a $J = 1$ state from the individual j-states are $(1/2, 1/2)_1$ and $(1/2, 3/2)_1$. These states correlate to LS-coupled states of different spin multiplicities; the $(1/2, 1/2)_1$ state is a triplet and the $(1/2, 3/2)_1$ is a singlet.

The resonance energies of these states are quite high; as an example the $(1/2, 3/2)_1$ state has a resonance energy of 26.32 eV as is shown in Figure 2.3. Multiphoton excitation of these resonances does not result in a well defined spectroscopic state (ie: one with a known J, M_J and Π_{ex}) since the excited state J can take on many values according to $\Delta J = \pm 1$ for the N-photon process. Synchrotron light sources yield high photon energies and fluxes that can excite these states, but the temporal pulse These autoionizing states have lifetimes on the order of hundreds of femtosecond to attoseconds; to resolve the decay in time, a shorter burst of light is needed. As an alternative to synchrotron slicing techniques and free electron lasers (FELs),[42–45] a table top instrument for the production of high energy photons with short temporal widths has been constructed based on high-oder harmonic generation (HHG).

2.3.2 High-Harmonic Generation

High-harmonic generation has generated the shortest bursts of light: 80 attosecond pulses.[46–50] While these pulses are extremely short, the difficulty in making and using the light for spectroscopic applications is significant. It is not necessary to use such short pulses to study electronic dynamics however, provided the dynamics studied occur on a longer time scale. Autoionization lifetimes can range from picoseconds to attoseconds so pulses of light in the femtosecond regime should be adequate to clock many of the decays. In instances where the lifetimes are not resolved, information on the PADs is still recovered, which yields the same information on the ionization dynamics as if it were well resolved in time.

High order harmonics are generated in this experiment by focusing the output of a Titanium:Sapphire laser into atomic argon. The laser is an amplified Spectra Physics Spitfire Pro pumped by a frequency doubled Evolution 30 Nd:YLF laser. The amplifier is seeded by a mode locked Tsunami oscillator pumped by a Millenia Nd:YVO_4 diode laser. The operating wavelength of the amplifier is tunable from $780 - 820$ nm. The repetition rate is 1 kHz and produces ~ 50 fs pulses. The strong field of the laser distorts the Coulomb potential of the argon, which allows the valence electron to tunnel ionize into the continuum. The free electron wavepacket propagates in the continuum as it is accelerated by the laser field. When the direction of the field reverses, the wavepacket is accelerated back to the ion core from which it was born. The electron can recombine with the ion releasing the excess kinetic energy it picked up in the continuum.[51,52] This generates only odd harmonics of the fundamental laser frequency due to the symmetry of the generation medium and periodicity of the HHG process which occurs every half laser cycle. To use these pulses of light in a pump-

probe experiment, an individual harmonic must be selected and focused into a target. The practical details of HHG and the experimental apparatus used to make and use them for spectroscopic applications are discussed in the following sections.

2.3.3 EUV Monochromator

Two different configurations to generate high order harmonics were used in the experiments presented. The krypton experiments used a pulsed jet of argon as the generation medium. The vacuum chamber is held near $10^{-3} - 10^{-4}$ Torr ($0.13 - 0.013$ Pa) with the use of a Leybold Roots blower. The HHG chamber is differentially pumped through a 1/4 inch aperture approximately 2 inches long which leads to a plane grating with a groove density of 600 lines/mm with a blaze angle of 3.4°. The distance between the gas jet and the center of the grating is 25.4 cm. The sum of the incidence and diffraction angles is 155°. The grating chamber is held at approximately 10^{-6} Torr (1.3×10^{-4} Pa) by a Shimadzu 400 L/s turbo pump backed by rotary vane mechanical pumps (Welsh). The angle of the grating is rotated relative to the incoming light to diffract the desired harmonic through the remainder of the monochromator. The grating is operated at first order diffraction for all experiments.

The selected harmonic is directed onto a gold coated plane mirror at an angle of 77° relative to normal incidence, 44.7 cm away from the grating. The chamber is held at vacuum by another 400 L/s Shimadzu turbo pump. This optic directs the light onto a gold toroidal mirror 50 cm away at an 83° incidence angle relative to normal incidence. The toroidal mirror is characterized by a 798 cm major and 13.9 cm minor radii of curvature. The toroidal mirror focuses the harmonic pulse into the interaction region 1094.7 cm away where it can be used as a pump or a probe pulse. The toroidal mirror chamber is held at an operational pressure of 10^{-8} Torr (1.3×10^{-6} Pa) with a Shimadzu 800 L/s turbo pump. A pair of slits are placed after the toroidal mirror to ensure only a single harmonic can enter the interaction region. These are made by affixing razor blades on a pair of linear translating feed-throughs with Torr-Seal.

An updated version of the experiment is used in the work performed on SESs in O_2. The revised experimental apparatus is depicted in Figure 2.4. Here the pulsed jet of argon is replaced with a gas cell. The 800 nm laser pulse is focused through two 200 μm holes over a 1.5 mm path length for HHG. The pressure is carefully optimized to maximize signal at the interaction region. Long term stability is enhanced in this configuration as no moving parts or intricate timing mechanisms are needed for operation. The gas cell is set to define the path of the rest of the monochromator, whereas in the previous pulsed valve configuration, the entire system needed frequent re-optimization for good harmonic yield. Also, the gas cell consumes much less gas and needs to only be pumped by a 3000 L/s Shimadzu turbo pump rather than a dedicated roots blower. The typical operating pressure in the chamber is 4×10^{-4} Torr (1.3×10^{-2} Pa) with a base pressure of 10^{-8} Torr (1.3×10^{-6} Pa).

The plane mirror is replaced in this configuration with a cylindrical mirror to focus

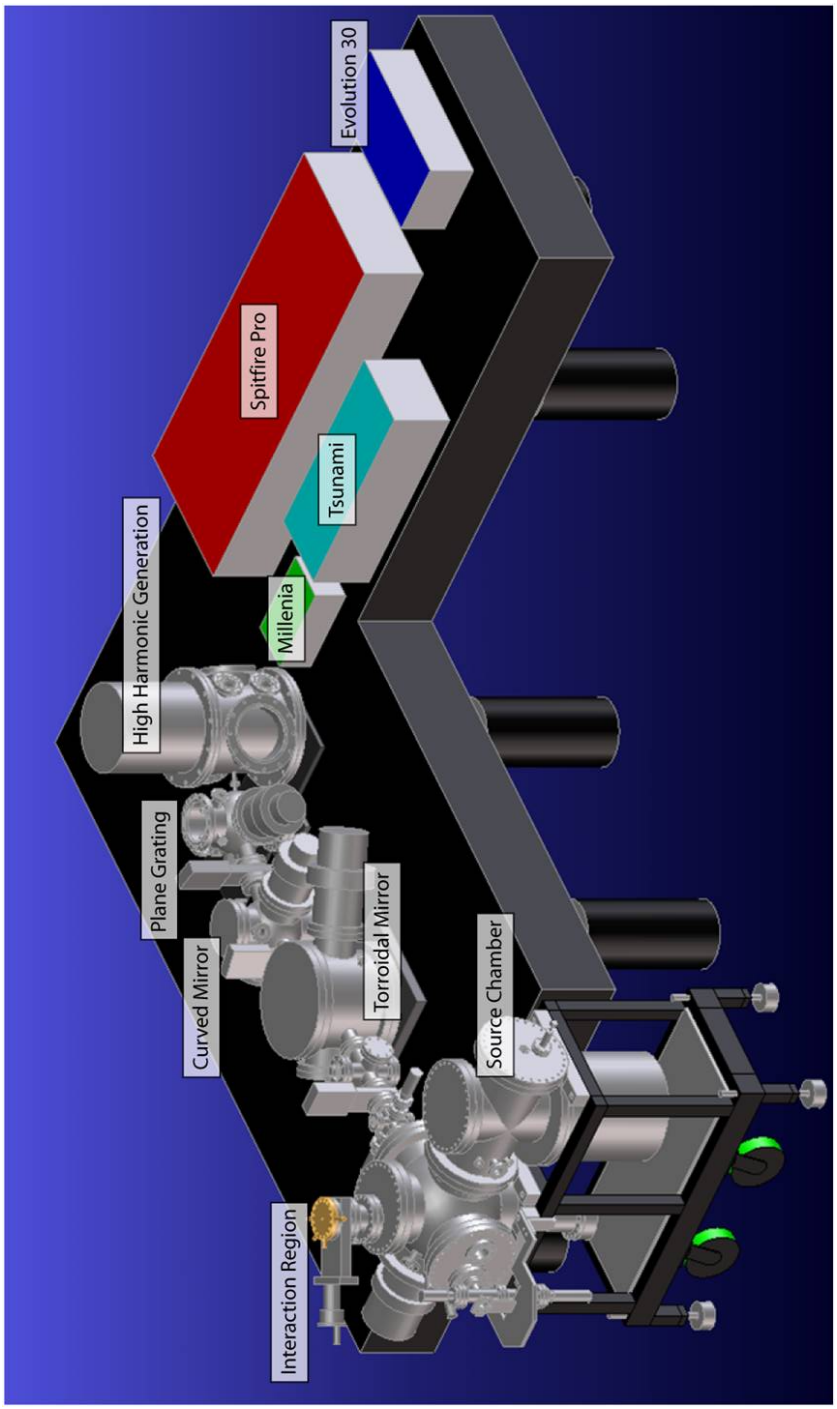

Figure 2.4: The experimental apparatus is illustrated here. The output of the Spitfire Pro femtosecond laser is split into a pump and a probe arm. The pump pulse is focused into a gas cell of 1.5 mm interaction length to generate high-order harmonics. The harmonics and residual fundamental co-propagate into a homebuilt monochromator. First, a plane grating (600 lines/mm) selects the harmonic order, a plane/cylindrical mirror directs the light onto a toroidal mirror, which focuses the individual harmonic in the interaction region. The interaction region intersects the pump and probe beams at $\sim 1^\circ - 2^\circ$ angle with an effusive beam of target gas. The ejected electrons are measured in a velocity map imaging spectrometer.

the beam along the horizontal axis. This improves the beam mode in the interaction region to a more Gaussian profile. The previous configuration without the cylindrical mirror had a beam focus resembling an ellipse. The improvement of the focal spot size in the interaction region increases pump-probe signal by about a factor of 10. The radius of curvature of this optical element is 500 cm. The harmonic beam intersects an effusive beam of target gas and a time delayed pump or probe pulse. The angle of intersection between the pump and probe pulses is approximately $1^\circ - 2^\circ$ which causes only slight temporal broadening.

The delayed pump/probe pulse can take on a variety of frequencies. The fundamental frequency can be doubled or tripled to generate 400 nm and 266 nm light. Also, a non-collinear optical parametric amplifier (NOPA) has been built which generates tunable light in the region of 500 nm $-$700 nm.[53] The pulse widths from the second and third harmonic generation tend to be longer, on the order of 70 fs $-$100 fs while the NOPA is capable of producing pulses of light on the order of 10 fs.[53] For the experiments described here, the fundamental 800 nm light is used as a probe exclusively due to higher power and to take advantage high ionization cross sections that produce low kinetic energy electrons. Future experiments using the flexibility of these tunable light sources are expected.

2.4 Velocity Map Imaging

Velocity map imaging (VMI) is a high throughput data acquisition technique capable of simultaneously determining the energy and angular distributions of ejected electrons or dissociated molecular ions. The configuration is based on the original design of Eppink and Parker.[54] In contrast to time-of-flight (TOF) electron spectrometers the collection efficiency of a VMI spectrometer is 100% and not limited by the the saturation of the detector current on multichannel scalars. The principle of VMI is shown in Figure 2.5. In general, electrons or ions are accelerated by a pair of electrostatic plates. Electric potentials are applied to these plates, which produce an electric field that acts as a lens to focus charged species with a given velocity to a specific radial distance from the center of a posititon sensitve detector. The electron cloud is projected onto an imaging quality microchannel plate (MCP) in a Chevron configuration coupled to a phoshpor screen (P47). A CCD (charge coupled device) camera reads out the bursts of light made when an electron hits the detector. The active area of the detector is 75 mm. Magnetic fields are eliminated by μ-metal shielding throughout the flight tube and by three orthogonal, home-wound, Helmholtz coils.

The detection of ionization events in the VMI spectrometer is improved over previous incarnations where the intensity of electron hits were measured in a frame averaged image;[27] in all experiments presented here, each electron is individually identified and its position recorded with sub-pixel resolution.[55] This eliminates substantial fluctuations of each hit intensity, which greatly improves the counting statistics and

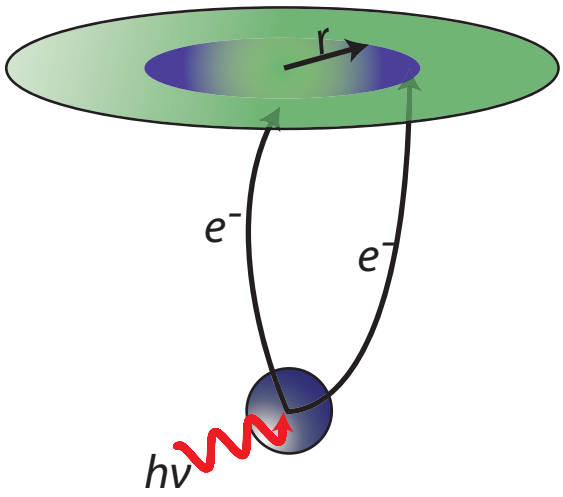

Figure 2.5: The principle of VMI is illustrated here. An ionization photon, $h\nu$, is incident on a target species. The ejected electrons are projected onto a 2-dimensional position sensitive MCP. All electrons with the same velocity are mapped to the same radius, r, from the center of the detector. The radius is proportional to the velocity of the outgoing electron or ion.

allows for a whole new set of experimental ideas to come to fruition. The details of the collection procedure and the characterization of the VMI spectrometer is expanded upon in the following sections.

2.4.1 Photoelectron Event Counting

Imaging MCPs can simultaneously measure many electron hits without saturation effects that plague conventional TOF spectrometers. If in each frame from the CCD camera each event is separated spatially, the centroid of each hit can be calculated. This relates the measured hit with a given intensity and two-dimensional spatial distribution (assumed to be Gaussian) to a single ionization event with precise x and y coordinates. This is best implemented with high frame rate cameras where many events are measured in each frame and event-counted. By particle counting, inherent fluctuations in the intensity of the light from each hit are effectively eliminated. The camera used in these experiments is an Imaging Source DMK21BF04 CCD camera. A region of interest is selected with 480×480 active pixels allowing for frame rates of 60 Hz to be read out to a computer through a fire-wire connection.

Each event signal intensity can vary many hundreds of percent from hit-to-hit. Particle counting eliminates these fluctuations completely so that limitations to the acquisition of the signal are from the high-harmonic source. By measuring each electron, the stability of the HHG source is easily assessed. Near shot-noise limited

signals (ie: $SNR \sim \sqrt{events}$) are frequently observed when the laser is optimized and warmed up for several hours. This allows for troubleshooting laser and HHG problems in addition to providing a baseline for proper instrumental operation if the number of events is large enough.

The acquisition of data is currently limited by the events that can fit on the MCP active area without spatial overlap of the hits. This is a signal dependent value, but for isotropic distributions tends to be about 100 events/frame. The data presented in all of the experiments discussed are carried out over several days of continuous integration. Improving the rep-rate of the camera closer to the rep-rate of the laser would improve counting statistics such that the HHG output is the limiting factor to data collection rates.

2.4.2 Single Photon Ionizations

The VMI spectrometer is calibrated to a set of single photon ionization events from atomic rare gas targets. Noble gases are used as they have well-defined ionization energies.[56] In some heavier elements fine structure elements become apparent but are also well characterized. Figure 2.6 shows some collected raw VMI images with a single selected harmonic pulse ionizing the target. These are collected all at the same electrostatic lens voltages to make a calibration curve used in a later described experiment. One can see that ionization of these gases results in not only significantly different electron kinetic energies, but also different angular patterns. The measured anisotropies will later be compared to literature values to establish that quantitative anisotropies are measured.

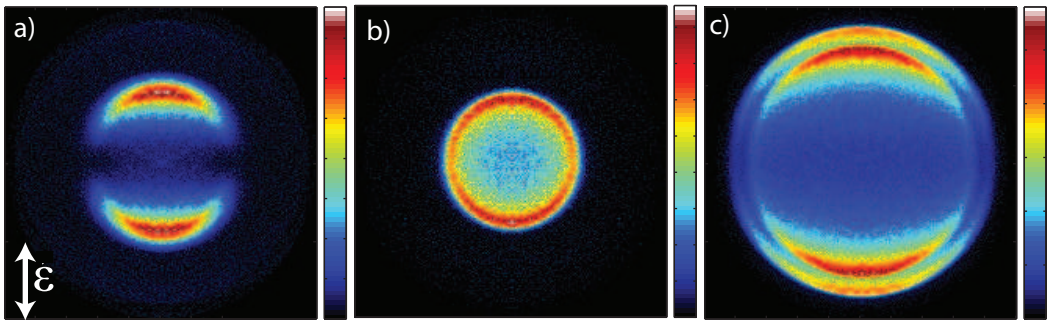

Figure 2.6: Single photon ionization of He with the 17^{th} harmonic, Ar with the 11^{th}, and Xe with the 11^{th} harmonic are shown in (a), (b), and (c), respectively.

First, the radial distributions of single photon ionization are considered. The radial distribution is defined by angular integration of the raw photoelectron image. Since the image is discrete (ie: the CCD camera bins the images) the radius at each

pixel takes on the convenient form

$$r = \sqrt{(x - x_c)^2 + (y - y_c)^2} \tag{2.8}$$

where r is the radius corresponding to the x and y pixels relative to the image center written as x_c and y_c. The r is calculated for every pixel in the image. The radial values are binned and the intensity of each pixel is added to the corresponding bin to build the total radial distribution. The radial distribution of the images shown in Figure 2.6 are shown in Figure 2.7(a). Since the binding energy is known for each

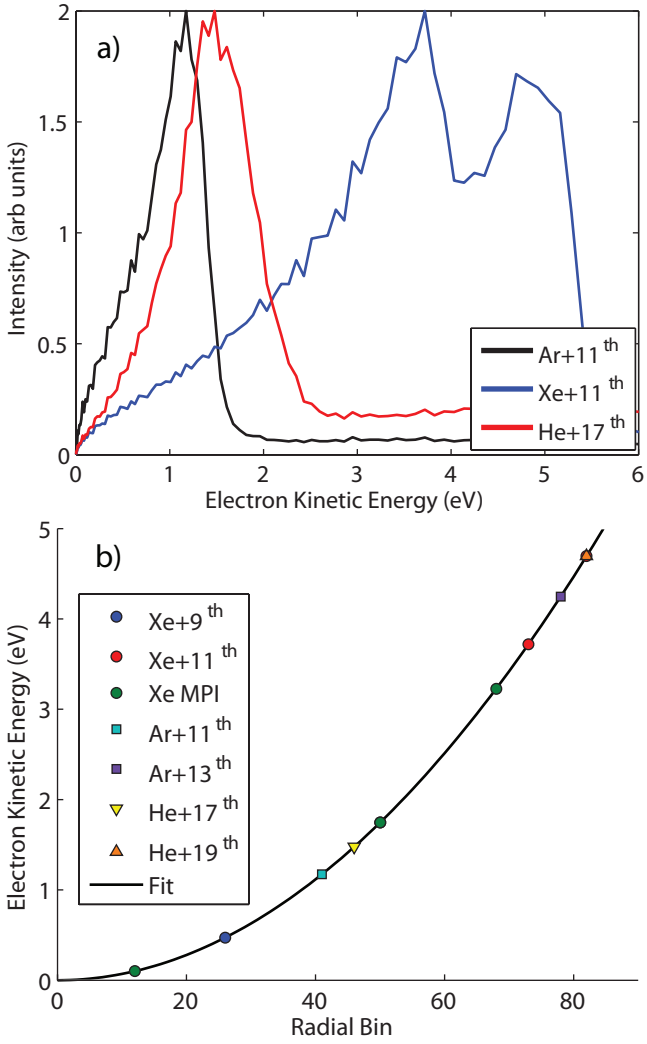

Figure 2.7: The radial photoelectron spectra of the images in Figure 2.6 are plotted in (a). The x-axis is calibrated in energy by fitting the curve given in (b). The relationship between radius and energy is quadratic.

atom and the harmonic order is known one can estimate the energy of the harmonic as

$$E_{HH} = Z(\frac{hc}{\lambda}) \tag{2.9}$$

where Z is the harmonic order, λ is the wavelength in nm that the fundamental laser frequency is centered at, h is Plank's constant, and c is the speed of light. The approximation in this step is that the harmonic photon energy is simply the product of the harmonic order and the energy of the driver pulse. This is an acceptable approximation in all the experiments presented here; at high driver powers the harmonic spectrum can actually be blue shifted to higher energies.[57] Blue shifting of the harmonic pulse typically is observed at average driving laser powers greater than 1.0 W in this setup. To avoid ambiguities, the energy of the harmonic is set as an adjustable parameter in the calibration. The measured spectrum and the driving laser central frequency should be consistent if the fit is of good quality. In the experiments presented here, the energy of the harmonic is well described by the simple product of harmonic order and energy.

The radial bins are equated to the expected kinetic energy of the feature by the use of the quadratic relation between velocity and kinetic energy.

$$E_K = ar^2. \tag{2.10}$$

The calibration constant, a, is determined from the solution to this equation. To more carefully calibrate the spectrometer, a series of spectra are collected and the sum of the squares of the errors for all the expected and measured kinetic energies are minimized. This ensures that the calibration coefficient describes all kinetic energies well and is less susceptible to errors. The harmonic photon energy is allowed to change as the solution is minimized and this value is present in the determination of the expected electron kinetic energy. The results of the calibration yield both the actual energy of the harmonic photons and the proportionality coefficient in Equation 2.10. An example of fitting the radial distribution is shown in Figure 2.7(b). Many more data points are included in this determination than are shown in Figures 2.7(a) and 2.6. The calibration includes several harmonic orders and gases to guarantee the energy axis is accurate. The proportionality coefficient here is determined to be $a = 0.0006981$ eV/r^2. Typical values for this constant are on the order of 1×10^{-4}–1×10^{-3} eV/r^2.

The raw images shown in Figure 2.6 are the 2-dimensional projection, $P(R', \theta')$, of the 3-dimensional distribution, $F(R, \theta)$, onto the imaging MCP. When the laser polarization is parallel to the detector face the cylindrical symmetry can be used to write the projection as the Abel projection as

$$P(R', \theta') = 2\int_{|x|}^{\infty} \frac{rF(R,\theta)}{\sqrt{r^2 - x^2}} dr. \tag{2.11}$$

where $x = R' sin(\theta')$ and $r = R\ sin(\theta)$. The projection is inverted to retrieve $F(R, \theta)$. Numerous techniques exist to carryout this procedure.[58–64] A discontinuity in the evaluation of the inverse able transform amplifies noise near the center of the image. The technique used in all the work presented here is the pBasex inversion, which uses a basis set of known projections in polar coordinates to evaluate the inverse transform.[62] This results in noise amplification near the center of the image and the electron anisotropies are determined in-situ. This is in contrast to other methods where the noise is concentrated at small angles relative to the laser polarization and the polar plots need to be fit individually to the Legendre expansion given in Equation 1.7.

The determination of the radial coordinate to electron/ion kinetic energy follows the exact procedure described for the radial distributions and yields similar results. One difference is that the binning of the radial distribution is uniform and takes integer values, while the inversion interpolates the Cartesian image onto a polar grid as a first step. This interpolation allows for smaller bin sizes at low radial coordinates where higher resolution is typically needed. This results in a small difference in the calibration coefficient, a, as given in Equation 2.10, but for the same photon energy to be retrieved. Examples of inverted images is given in Figure 2.8 and the photoelectron spectrum and calibration is shown in Figure 2.9

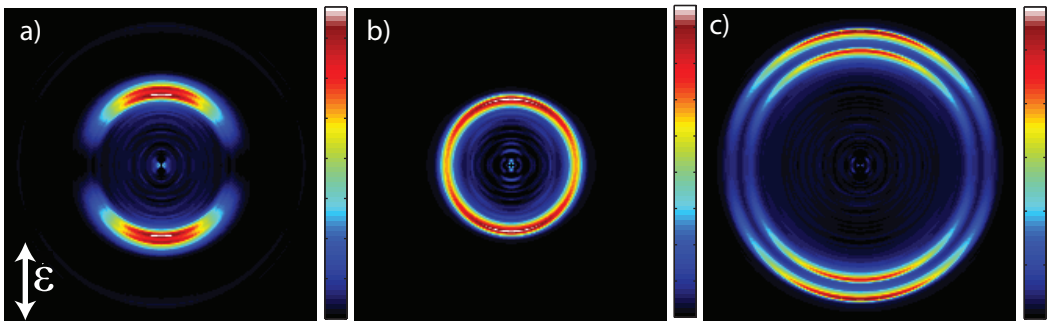

Figure 2.8: Inverted single photon ionizations of He with the 17^{th} harmonic (a), Ar with the 11^{th} (b), and Xe with the 11^{th} harmonic (c).

Once the images are inverted and the kinetic energy axis calibrated, the anisotropy of each photoelectron spectrum can be considered. It is important that the energies of the photoelectrons be known since the anisotropy parameters are strongly energy dependent. The energy dependence is manifested in the the Coulomb phase shift and radial dipole matrix elements for each outgoing partial wave. The pBasex inversion yields anisotropy parameters as a function of energy. By selecting a region near the maximum of the photoelectron peak, the photoelectron intensity weighted average of the energy dependent anisotropy parameters result in the quantitative anisotropy parameter. Some of these values are given in Table 2.1 for ionization of different atoms with different harmonics.

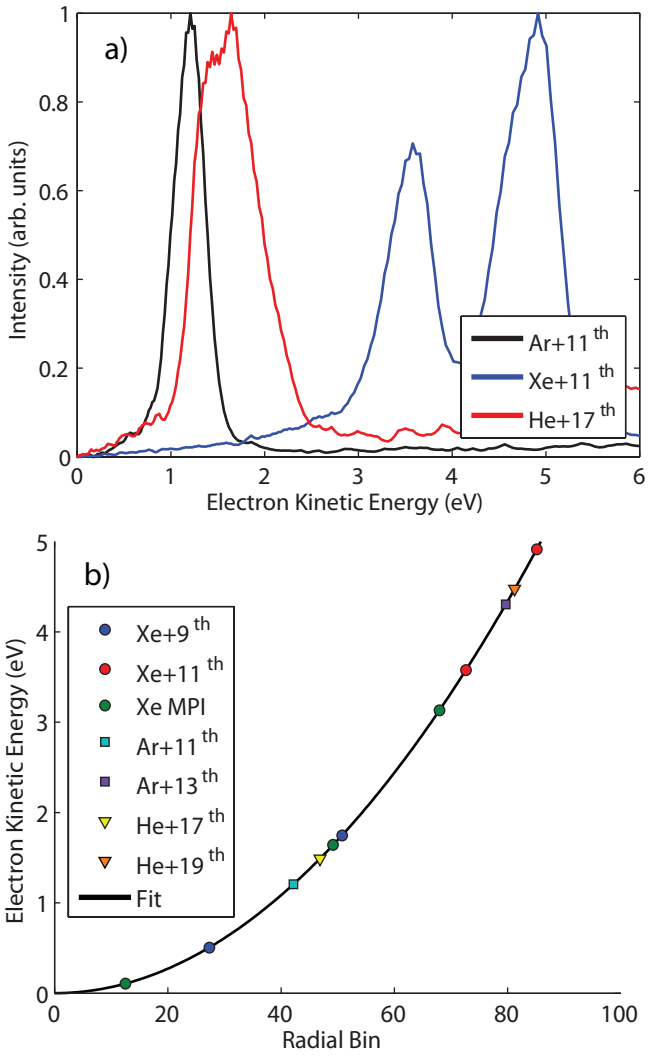

Figure 2.9: The inverted photoelectron spectra of the images in Figure 2.8 are plotted in (a). The x-axis is calibrated in energy by fitting the curve given in (b). The relationship between inverted radial bin and energy is, once again, quadratic.

The measured values of the single photon ionization anisotropy parameters agree very well with literature values.[65] Most notable is the ionization of helium with the 17^{th} harmonic. Since the only electrons in helium are s-electrons the only outgoing partial wave allowed is a P-wave. Since only one electron partial wave is ejected, no interferences exist in the final continuum, and Equation 1.5 reduces to the sole value of $\beta_2 = 2$. The measured value given in Table 2.1 is 1.99 ± 0.05. Deviations away from ideal s-orbital ionization are generally a result of spin-orbit interactions in the ionization step that allow spin-flip contributions to the total PAD which have anisotropies

	Atom				
	Helium	Neon	Argon	Xenon	
Harmonic Order	$^2S_{1/2}$	$^2P_{3/2}$	$^2P_{3/2}$	$^2P_{1/2}$	$^2P_{3/2}$
11^{th}	-	-	0.27 ± 0.05	1.05 ± 0.10	1.45 ± 0.01
13^{th}	-	-	0.85 ± 0.06	1.59 ± 0.07	1.72 ± 0.04
15^{th}	-	-0.16 ± 0.03	1.27 ± 0.01	-	-
17^{th}	1.99 ± 0.05	0.24 ± 0.01	-	-	-

Table 2.1: Measured single photon ionization anisotropy parameters of rare gas atoms with various harmonic orders. All results agree extremely well with literature values indicating the VMI spectrometer measures quantitatively accurate PADs.

of $\beta_2 = -1$.[19,66] The frame work of angular momentum transfer theory treats these parity unfavored contributions to the measured anisotropy as an incoherent weighted sum over the participating channels. The anisotropies for each channel are weighted with the cross section connecting the probed state to each pathway. This allows for quantifying the extent of configuration mixing in the initial or final states and will be used to understand observations discussed in later chapters.

2.4.3 Resonant Two-Photon Ionization

The instrumental response of the system is determined from resonant two photon ionization of atomic helium as it best represents the true width of the pump and probe pulse cross-correlation. This technique accurately characterizes the 15^{th} harmonic instrumental response and allows for other harmonics to be overlapped in time with an approximation to the instrumental response. There is currently no better strategy to accurately measure the instrumental response for higher order harmonics that do not involve strong probe fields such as in above threshold ionization (ATI) measurements.[28,29] ATI measurements systematically under-evaluate the true harmonic-optical pulse cross-correlation as the strong field process occurs only near the maximum of the optical pulse envelope.

In the resonant two photon ionization the 15^{th} harmonic excites the $1s3p$ or $1s4p$ resonance in atomic helium. These states have lifetimes on the order of nanoseconds and are instantaneously populated by the harmonic pulse. As the delay between the pump and probe pulse is scanned from negative times to positive times the convolution of the two pulses with a step function is measured in time. Negative times correspond to delays where the probe pulse arrives at the samples before the pump, while positive times correspond to delays where the pump arrives before the probe. Plotting the

measured photoelectron spectrum at each time delay gives a two-dimensional map of the time evolving signals. A representative time-resolved photoelectron spectrum of atomic helium probed with a delayed 805 nm probe pulse is shown in Figure 2.10.

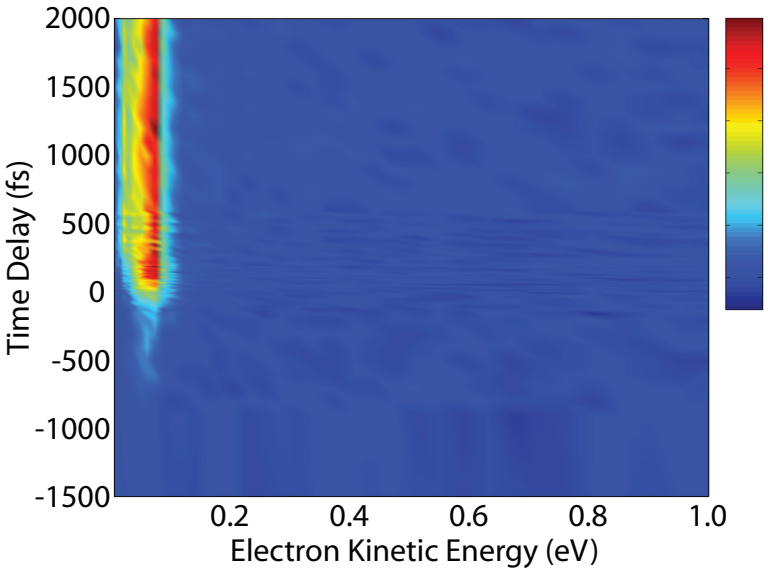

Figure 2.10: The time-resolved photoelectron spectrum resulting from resonant two photon ionization of atomic helium is plotted on an arbitrary color map.

This spectrum provides two complementary pieces of information: electron kinetic energy and temporal evolution. If a slice along the time axis is taken, the photoelectron spectrum at that time delay is recovered. In the resonant two-photon ionization of helium with 805 nm light the electron kinetic energy is ~ 50 meV. If on the other hand, a slice along the energy axis is taken the time evolution of the system is recovered. Numerous slices can be taken over many different ranges to track the rise and decay of multiple channels simultaneously. The electrons from helium are integrated over a 5-bin energy region and plotted over time in Figure 2.11. Here two regions are highlighted in Figure 2.11: (a) considers all the time delays sampled from negative times to very large positive times, (b) focuses on early times where the instrumental response is apparent. Since the lifetime of the excited state is on the order of nanoseconds, the long time delays sampled here do not show a significant decay. As a result the decay can be neglected completely in the fitting of the transient signal. This reduces the complexity of fit significantly and makes the determination of the cross correlation a matter of fitting the data to the function

$$S(t) = A\left[1 + erf\left[\frac{(t - t_0)}{\sqrt{2}\sigma_{cc}}\right]\right] + d. \tag{2.12}$$

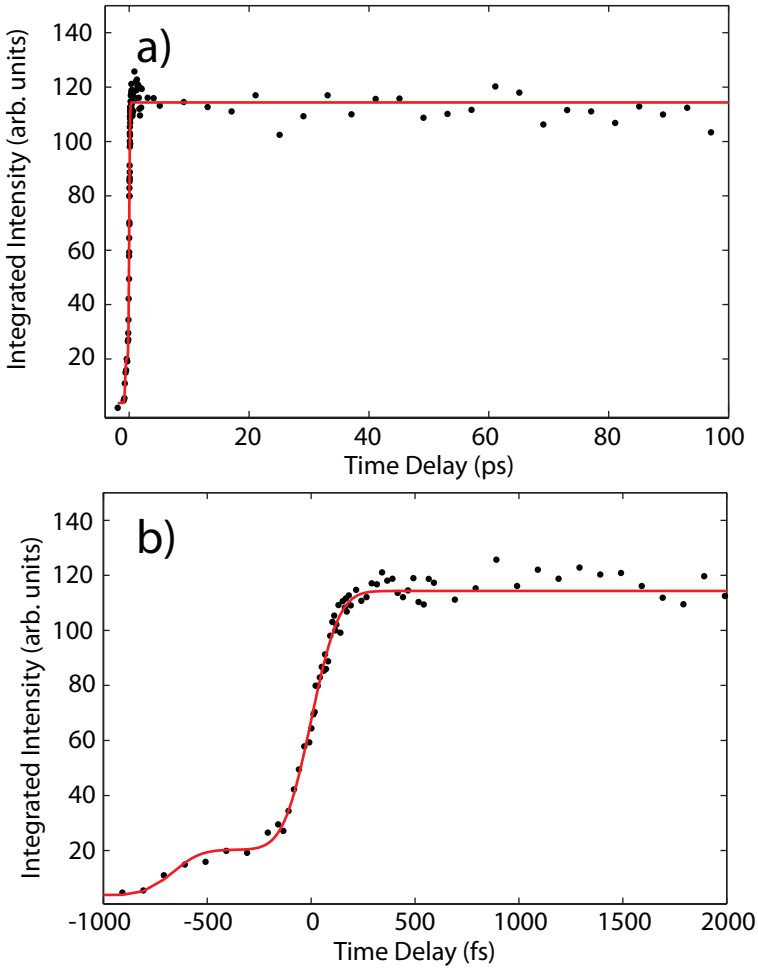

Figure 2.11: Transients for helium pump probe with corresponding fits in the absence of pulse shaping

Here, $S(t)$ is the transient signal, A is a free fit amplitude, t_0 is the offset of the estimated $t = 0$ relative to the true temporal overlap, σ_{cc} is the instrumental cross correlation, and d represents an offset. This can be expanded to include pre- or post-pulses that are sometimes measured in the experiment. This is observed in the early dynamics shown in Figure 2.11(b). These apparent problems are easily characterized and accounted for even in more complex systems provided a high-quality instrumental response is obtained.

The typical instrumental response is found to be in the range of 60-120 fs when helium is probed in this example. The measured response is dependent on the chirp of the probe pulse as the high-harmonic temporal widths are typically much shorter and the spectral bandwidths much larger. Effects from high sample density shaping

the spectral width of the exciting high-harmonic pulse have been explored and found to influence the transient signals significantly.[67] This affects the determination of the true $t = 0$ and cross correlation. This is deliberately used to find the approximate temporal overlap when the system is initially aligned since the signal of the pulse shaping near $t = 0$ is amplified. When the instrumental response is determined, as shown in Figure 2.11, the effusive beam is strongly attenuated by a needle value while the distance between the nozzle and skimmer is increased.

2.5 Final Remarks

The instrument described above is capable of probing dynamics of autoionization and dissociation. In the work presented in the following chapters only atomic and diatomic species are discussed in the context of electron VMI. On going work in the lab is focusing on introducing large ionic salts called room temperature ionic liquids (RTILs) into the VMI spectrometer and probing the ion kinetic energy distributions to uncover the photo-physics of these species.

Chapter 3

Photoelectron Angular Distributions from Autoionizing $4s^1 4p^6 6p^1$ States in Atomic Krypton Probed with Femtosecond Time Resolution

Photoelectron angular distributions (PADs) are obtained for a pair of $4s^1 4p^6 6p^1$ ($j = 1/2$ and $j = 3/2$) autoionizing states in atomic krypton. A high-order harmonic pulse is used to excite the pair of states and a time-delayed 801 nm ionization pulse probes the PADs to the final $4s^1 4p^6$ continuum with femtosecond time-resolution. The ejected electrons are detected with velocity map imaging to retrieve the time-resolved photoelectron spectrum and PADs. The PAD for the $j = 1/2$ triplet state is inherently separable by virtue of its longer autoionization lifetime. Measuring the total signal over time allows for the PADs to be extracted for both the the $j = 3/2$ singlet state and the $j = 1/2$ triplet state. Anisotropy parameters for the $j = 1/2$ triplet state are measured to be $\beta_2 = 0.55 \pm 0.17$ and $\beta_4 = -0.01 \pm 0.10$ while the $j = 3/2$ singlet state yields $\beta_2 = 2.19 \pm 0.18$ and $\beta_4 = 1.84 \pm 0.14$. For the $j = 3/2$ state, the ratio of radial transition dipole matrix elements, X, of outgoing S to D partial waves and total phase shift difference between these waves, Δ, are determined to be $X = 0.56 \pm 0.08$ and $\Delta = 2.19 \pm 0.11$ radians. The continuum quantum defect difference between the S and D electron partial waves is determined to be -0.15 ± 0.03 for the $j = 3/2$ state. Based on previous analyses, the $j = 1/2$ state is expected to have anisotropy parameters independent of electron kinetic energy and equal to $\beta_2 = 5/7$ and $\beta_4 = -12/7$. Deviations from the predicted values are thought to be a result of state mixing by spin-orbit and Fano configuration interactions in the

intermediate and final states; theoretical calculations are required to quantify these effects.

3.1 Introduction

Photoelectron angular distributions (PADs) measured from electronically excited atomic and molecular states contain information about the character of the electronic state from which the electron originates, as well as interactions that describe scattering of the electron from the residual ionic core. The nature of the excited state is uniquely imprinted on the continuum electron partial waves as interference patterns measured in the PAD. The building blocks of the PAD are radial transition dipole matrix elements and phase shift difference between the partial waves. A detailed measurement of the PAD provides insight into dynamics of the excited electronic state, which include perturbations and admixtures to the excited state as well as influences of the residual ionic core on the outgoing electron. The effects of neighboring interacting resonances and spin-orbit interactions on excited state PADs probed to a featureless continuum have been previously investigated as well as influences on PADs from other autoionizing states in the final continuum.[7,11,18,20,22–24,26,68,69] As a probe of chemical dynamics, PADs are promising as a sensitive tool to track changes in electronic surfaces as a chemical reaction is evolving. This is especially important in understanding non-adiabatic dynamics in polyatomic molecules.[34,70–72]

A particularly interesting type of excited state occurs when a discrete state is embedded within a continuum of states, for example, in electronic excitation with extreme ultraviolet (EUV) radiation of an atomic species above the ionization threshold. The excited state relaxes via autoionization and interferes with the direct ionization channel, resulting in characteristic spectral line shapes, as addressed in the original work of Fano.[14,16,73] The result of the configuration interaction is to modify the discrete wavefunction by admixing continuum character into it. In probing autoionizing states, information about the coupling matrix elements between the resonance and continuum as well as insight into the transition dipole matrix elements to each pathway are inferred. Fano interferences are not limited to photoabsorption or photoionization experiments on isolated atomic and molecular systems, but are also observed and manipulated in a variety of solid state samples whenever multiple channels evolve to a common final state.[74–80] It is thus valuable to investigate the influence of autoionization on isolated atomic systems using PADs to extract insight into the behavior of the transiently excited state. This can be extended to molecular systems where the Born-Oppenheimer approximation breaks down, such that autoionization is competitive with neutral dissociation.[35] This will be especially important in few femtosecond to attosecond time regime experiments where competing and interacting channels become increasingly likely. Probing the femtosecond excited state dynamics and PADs of isolated atomic species provides a basis for future experiments on highly

excited atoms and molecules.

If the autoionizing state formed after absorption of an EUV photon is probed on a time scale comparable to the autoionization lifetime, the time-evolving system can be directly investigated. The angle-integrated time-resolved photoelectron intensities provide excited state lifetimes and energetic information; in addition, observation of the PADs from the excited states gives insight into the nature of the autoionizing resonance and to the ionization dynamics from these states. The amplitude of partial waves and relative phases arising from each state are sensitive probes of the electronic character of the excited state and the scattering of the outgoing electrons with the residual ion core. By simultaneously measuring the photoelectron energy and angular distribution, a more complete understanding of the excited state relaxation and photoionization dynamics are determined. Femtosecond time-resolution provides the possibility to separate contributions from overlapping states with different lifetimes to retrieve the individual excited state PADs and lifetimes. The pump-probe experiments investigated here prepare and subsequently ionize aligned targets. This allows for the determination of the ratio of radial transition dipole matrix elements and phase shifts difference between the outgoing partial waves of the electrons that are ejected into the continuum when the excited state electron density is aligned parallel to the probe laser polarization. In excitations where the electron density is perpendicular to the laser probe polarization, the equations that describe the anisotropies reduce to constant values; deviations from the expected values illustrate effects of configuration mixing and spin-orbit interactions.[7,11,18,20,24,27–29,68,69,81]

Two $4s^14p^66p^1$ Rydberg states in atomic Krypton are excited in this work using a high-order harmonic of an 801 nm laser as a pump pulse that prepares the autoionizing states. These are subsequently probed by a time-delayed 801 nm pulse to ionize the system to the $4s^14p^6$ ($^2S_{1/2}$) continuum as depicted in Figure 3.1. Both pulses are polarized in the same direction. The $4s^14p^66p^1$ state is only slightly split in energy (14 meV). The pair of states is described in a jj-coupling scheme where the excited electron angular momentum, j_e, is coupled to the ionic core angular momentum, j_c, to yield a total angular momentum, J, written as $(j_c, j_e)_J$. The $4s^14p^66p^1$ pair of states are given by $(1/2, 1/2)_1$ and $(1/2, 3/2)_1$, which are henceforth referred to as $j = 1/2$ and $j = 3/2$ states for brevity. It should also be noted that these states correlate to LS-states of different spin-multiplicities; specifically, the $j = 1/2$ is of triplet character and the $j = 3/2$ state is a singlet. Neither state is pure singlet or triplet due to configuration mixing.[12–14,16] The excited states are described in a jj-coupling scheme while LS-coupling serves as an approximately good set of quantum numbers for the decomposition of anisotropy parameters for the $j = 3/2$ singlet state into cross section ratios and phase shifts. The $j = 1/2$ state cannot be decomposed into these parameters because the equations used to describe the PADs reduce to constants when the pump and probe laser polarizations are parallel.[22,23] Each autoionizing state has associated with it a characteristic Fano profile index, q, spectral width, and resonance energy, for which there is reported information from

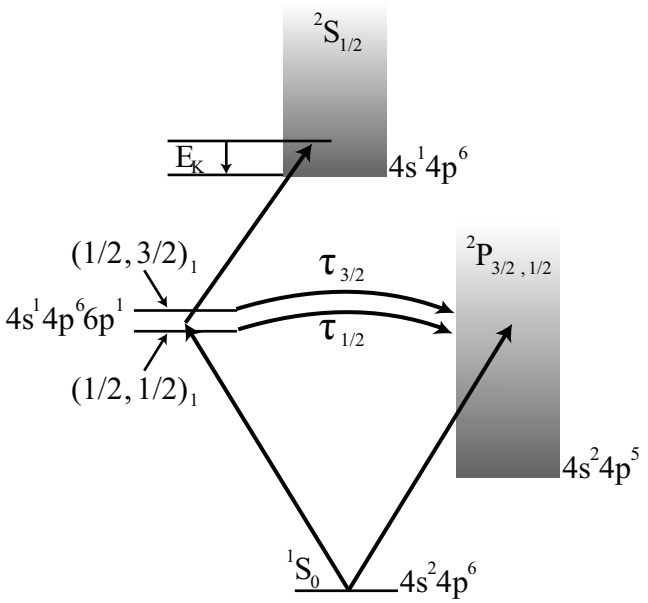

Figure 3.1: An energy level diagram depicting the excitation of ground state Krypton in the $4s^24p^6$ ($^1S_0$) configuration to a pair of $4s^14p^66p^1$ states in krypton described in a jj-coupling scheme as $(1/2,1/2)_1$ and $(1/2,3/2)_1$. The excited states autoionize to the direct $4s^24p^5$ (^2P_J) ionization continuum with a state-dependent lifetime given by τ_j. The interference between direct ionization and autoionization channels is manifested as a Fano line shape, which is observed in static experiments. A time-delayed 801 nm probe pulse ionizes the excited states to the final $4s^14p^6$ ($^2S_{1/2}$) continuum, releasing an electron of kinetic energy, E_K.

higher resolution spectral techniques.[12–14,16,31,32] The two states are characterized as window resonances with small q-parameters of opposite sign. The PADs from single photon excitation and subsequent autoionization of the singlet $4s^14p^65p^1$ state at lower energy have been studied both experimentally and theoretically.[82,83] In, the current work, with the benefit of the time-resolution and inherent alignment via excitation with linearly polarized light in the pump-probe experiment, the ratio of radial dipole matrix elements of S and D waves as well as the phase shift difference between these waves are obtained for ionization from the $j = 3/2$ state. The nascent PADs from each state are separated using the femtosecond time-resolution to extract the effective contribution of each state in the total photoelectron signal (the sum of the two states at early times and predominantly the $j = 1/2$ state at longer delays). The results reveal substantially different PADs originating from each state, which reflect the different electronic characters and alignments of the $j = 1/2$ and $3/2$ states. Configuration mixing and spin-orbit interactions, as well as scattering within the multielectron atom, no doubt influence the measured PADs from each state; this

is evident in the measurement by a significant deviation in the measured β_4 anisotropy parameter for the $j = 1/2$ state compared to the expected value.

3.2 Experimental Details

A similar experimental apparatus to the one used here is described elsewhere.[27–29,67,84] Briefly, an amplified Titanium:Sapphire laser system producing 50 fs pulses with 2.5 mJ/pulse at 1 kHz is split into a pump and a probe path. Approximately 650 mW average power is focused into a pulsed jet of argon where high-order harmonics are generated. Individual harmonics are selected and separated from the residual fundamental by a home built EUV monochrometer consisting of a plane grating, plane mirror, and a torroidal mirror. The 17^{th} harmonic, with energy centered at 26.32 eV and full width at half maximum (FWHM) of ∼0.3 eV, is selected to resonantly excite the $j = 1/2$ and $3/2$ states as well as the $4s^2 4p^5$ direct ionization continuum (Figure3.1). Of the remaining fundamental, only 450 mW of the 801 nm light is delayed in time and overlapped at a small angle with the harmonic pulse in the interaction region where the excited Kr atoms are ionized to the final $4s^1 4p^6$ continuum. Ejected photoelectrons are projected onto an imaging microchannel plate with an electrostatic lens in a conventional particle counting velocity map imaging (VMI) setup from which energy- and angle-resolved information is measured simultaneously.[54] The intensity of the 801 nm probe pulse is kept low to avoid multiphoton ionization to any extent and to minimize strong-field effects[85] that would complicate the analysis. This assumption is tested and confirmed by a separate power dependent experiment in which the 801 nm probe laser power is varied; the results showed no shift of the electron kinetic energy with respect to probe intensity. The pressure in the interaction region is kept very low to minimize spectral pulse shaping effects that would affect temporal measurements in a non-trivial way.[67] All laser polarizations are carefully optimized parallel to the detector face such that cylindrical symmetry is preserved in the VMI spectrometer.

Data is presented from two separate experimental efforts: one focuses on the acquisition of the time-resolved photoelectron spectrum taken with 25 fs step sizes in the range of -542 to +583 fs (46 time delays); the second consists of larger, 50 fs, steps sampling the range of -242 to +258 fs (11 time delays) in an effort to acquire the best possible angular distributions. The former experimental data are collected continuously for approximately four days while the latter data are obtained over two days of acquisition. Negative times correspond to delays where the 801 nm probe pulse arrives at the sample before the 26.32 eV pump pulse, while positive times indicate the pump pulse arrives before the probe. Since the experiment is performed over multiple days, hundreds of iterations at a single delay are acquired. Pump-probe (harmonic and 801 nm probe) and background (harmonic only) images are alternately collected every five seconds and co-added to form final images. The

resulting summed images are then symmetrized and rebinned before application of the pBasex inversion technique,[62] from which quantitatively accurate photoelectron energies and anisotropies are retrieved.[27–29] Photoelectron spectra are calibrated with known energies of rare gases ionized by a single photon whereby the photon energy is determined from the calibration; similarly, the PADs collected for these reference gases agree favorably with literature values. Blue-shifting of the high-harmonic spectrum is typically observed to have an onset near an average driving laser power of >1 W in this system. At the lower driving laser powers used in this work, this effect is not observed. All quoted uncertainties correspond to one standard deviation.

3.3 Results and Discussion

The measured photoelectron images are regarded as having a total signal that can be decomposed into the partial contributions from each autoionizing state. The contribution of each transient photoelectron signal from both states allows for the deconvolution of the total PAD into the time-independent PADs for the individual $j = 1/2$ and $3/2$ states. In the analysis that follows, the coherent excitation and possible interference of the two levels and this effect on the PADs is neglected. The validity of this assumption is assessed and found to not influence the present results, as will be discussed in detail later. With the current time-resolution, a coherence at early time delays would not be clearly observable. The phase of the coherence is not presently known; however, the amplitude of the signal is related to the dipole matrix element connecting the excited state in a spin-flip ionization to the final continuum, which is expected to be negligible.

Figure 3.2(a) shows representative raw photoelectron images collected at the time delays of -8 fs (within pulse overlap) and +242 fs, set side-by-side for ease of comparison. It is seen that the radius of the ring at early times is slightly larger than is observed at later time delays, indicating that faster electrons are ejected at shorter time delays. With the decrease in radius over time comes a decrease in the signal-to-noise ratio due to fewer excited states persisting at later times as a result of autoionization. The inverted images are shown in Figure 3.2(b) where the same decrease in radius is observed along with more noticeable changes in the angular distribution between the two time-delays. Based on previous spectral measurements,[12,31,32,86] the radius at long time delay corresponds to electrons primarily originating from the $j = 1/2$ state, which has a peak at 0.32 eV kinetic energy, whereas the radius measured at early time delay is attributed to electrons ejected from a mixture of the $j = 1/2$ and $3/2$ states, which has a 0.35 eV peak kinetic energy.[12,31,32,86] A slight discrepancy in the energy splitting compared to the expected 14 meV splitting is attributed to the bin sizes in the images. The present bin spacing is approximately 0.007 eV, thus, if the maximum of the peak is one bin off, the resulting $j = 1/2$ state is measured to have a peak energy of 0.33 eV, in closer agreement with expectations for the splitting.[12,31,32,86]

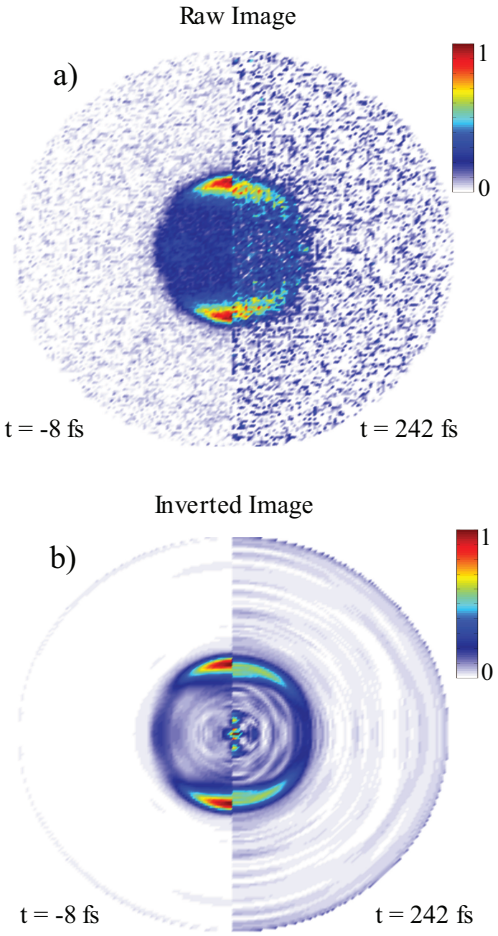

Figure 3.2: Raw photoelectron velocity map images at -8 fs and +242 fs are shown side-by-side in (a) to demonstrate the change in radial and angular features observed over time. The inverted images at the same time delays are shown in (b). The changes are understood by noting that the images are a result of two simultaneously populated spectrally overlapped states that decay with characteristic lifetimes. Early time delays are dominated by contributions from the sum of $j = 3/2$ and $j = 1/2$ states in Kr while later times are composed mostly of electrons originating from the $j = 1/2$ state. Features near the center of the image (ie: near zero kinetic energy) are an artifact of the inversion process.

To more quantitatively interpret the results, a time-resolved photoelectron spectrum is created by angular integration of the inverted images at each time delay. This is plotted in Figure 3.3(a) as a contour map in the range of 0 eV to 0.7 eV and -250 fs to +150 fs. It is observed that the kinetic energy distribution peaks at 0.35 eV at early times and at 0.32 eV at later time delays, each with a FWHM of $\sim$ 0.1 eV. Since the ionization process is a two photon interaction with linearly polarized light,

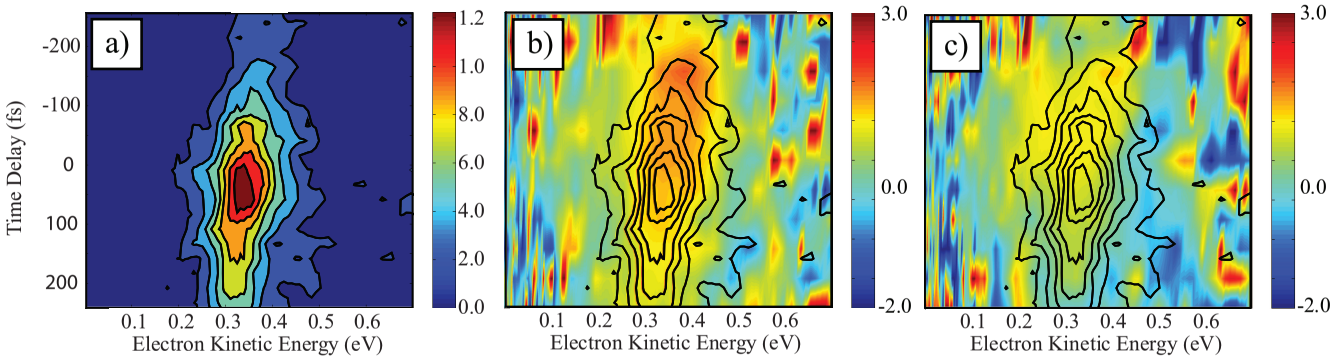

Figure 3.3: The time-resolved photoelectron spectrum (a) shows a change in electron kinetic energy over time indicated with a linear color map of arbitrary intensity. At early time delays the kinetic energy is measured to be 0.35 eV while at long time delays the energy is observed to be 0.32 eV, corresponding to electrons ejected from the sum of $j = 3/2$ and $j = 1/2$ states, and mostly $j = 1/2$ states, respectively. This small shift in energy is not resolved in the frequency domain with the femtosecond pulsed laser, but with the time-resolution afforded by the short pulses the energetic differences are effectively separated due to the unique autoionization lifetime of each state. Figures (b) and (c) correspondingly plot the β_2 and β_4 anisotropy parameters with the photoelectron contour lines in (a) overlaid to illustrate where meaningful angular distributions are retrieved. The color scale is set to represent anisotropies between -2 and 3 accurately. It is observed that the PADs evolve in time as the composition of the photoelectron signal changes from the sum of $j = 3/2$ and $j = 1/2$ states to dominantly $j = 1/2$ contributions.

the angular distribution is given by[8,9]

$$I(\theta) = \frac{\sigma}{4\pi}\left[1 + \beta_2 P_2(cos\theta) + \beta_4 P_4(cos\theta)\right] \tag{3.1}$$

where σ is the total cross section for photoionization and, β_2 and β_4 are the anisotropy parameters. Correspondingly, P_2 and P_4 are the second and fourth order Legendre polynomials. Figures 3.3(b) and 3.3(c) show the β_2 and β_4 anisotropy parameters, each plotted versus time and energy, with the transient photoelectron contours overlaid. Physically meaningful anisotropy parameters are measured only where the photoelectron intensity is appreciable. Artifacts in the inversion step are observed to occur as large peaks or dips in the extracted anisotropy parameter in regions outside of the photoelectron contour lines. The color scale is set such that anisotropies less than 3 and greater then -2 are accurately represented on a meaningful color scale.

3.3.1 Isolation of j-State Anisotropy Parameters

The evolution of the measured anisotropy parameters observed in Figures 3.3(b) and 3.3(c) is a result of the changing contributions of the individual PADs of the two j-states incoherently added together to constitute the measured total PAD. A composition term for the j-state contribution to the total signal at a given time delay is expressed as

$$\xi_j(t) = \frac{I_j(t)}{\sum_i^f I_j(t)} \tag{3.2}$$

such that for the two contributions to the total signal there is a partial intensity of the j^{th}-state component, $I_j(t)$, which changes over time. The time-resolved photoelectron spectrum is used to extract the time-dependent contribution of each state to the total signal. Three representative photoelectron spectra at three different time delays are shown in Figure 3.4.

To retrieve the compositions of the total PAD attributed to the specific j-states, slices over a small energy range are taken from the time-resolved photoelectron spectrum and integrated over energy. Electrons predominantly from the $j = 3/2$ state are integrated in the range of 0.38 to 0.42 eV and labeled as 'fast electrons', while electrons from the $j = 1/2$ are integrated in the region of 0.25 to 0.29 eV and called 'slow electrons'. This is schematically shown in Figure 3.4, which illustrates three photoelectron spectra collected at three different time delays and the two regions of integration. These ranges were selected such that each region has minimal overlap with the neighboring photoelectron line while maintaining good signal-to-noise. The edges of the slices are identically the same energy away from the center of the photoelectron line and consist of an equal number of radial bins. The integrated regions are representative of the time-resolved composition of the two individual excited states. The width and position of the two regions were varied and found to have no statistically significant influence on the results. Specifically, the region was shifted by two

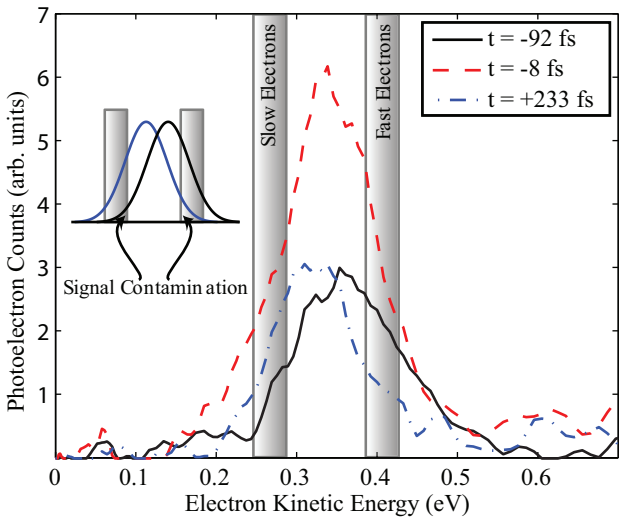

Figure 3.4: The photoelectron spectra from three representative time delays are given along with the areas of integration for constructing the transient photoelectron traces in Figure 3.5(a). The solid line is taken at -92 fs, the dashed trace collected at -8 fs and the dashed-dotted curve is at a delay of +233 fs. The two resonances overlap within the instrumental resolution of $\sim$ 0.1 eV depicted in the inset. The maximum contamination of one resonance on the neighboring transient signal is estimated to be 30 percent as shown in the inset.

bins to higher and two bins to lower energies for the $j = 3/2$ and $1/2$ slices, respectively, while the width was varied from 1-5 bins about the center bin. The analysis indicates that the selected regions are dominated by the temporal evolution of each individual state.

Since the $j = 1/2$ and $3/2$ states are closely spaced (0.014 eV), the extent to which each transient signal is contaminated by the neighboring signal must be assessed. The spectral line widths have been measured to be 0.007 eV for the $j = 1/2$ states and 0.013 eV for the $j = 3/2$ state.[12] The spectral resolution in the present experiment is approximately 0.1 eV, which is large compared to the individual line widths. Assuming the electron signal from each state is Gaussian in energy and given the known resonance energies of the two states,[12,31,32,86] the maximum contamination from the nearby state is estimated to be $\sim$30 percent. This is shown schematically in the inset in Figure 3.4 for the case where the two states would be present with equal intensity. The systematic contamination of the individual signals on the measured composition and PADs will be addressed further below. Excitation cross sections for the two states are known from static experiments and have comparable values; the $j = 3/2$ state has approximately 70 percent of the cross section relative to the $j = 1/2$ state.[12] However this information is not needed explicitly, as the relative cross sec-

tions are inherently accounted for in the fitting of the time-resolved photoelectron spectrum. This includes weighting factors that describe the different degeneracies of one j-state compared to the other (e.g. spin multiplicity) as well as the Fano configuration interactions that influence the absorption cross sections.

The energy integrated slices are plotted versus time in Figure 3.5(a). Each signal is fitted to a convolution of a Gaussian instrumental response function with a single exponential decay representing autoionization. In the fitting process, each data point is weighted with its associated error. The labeled fast and slow transient photoelectron curves are fit simultaneously, sharing common coefficients, such as the instrumental response, wherever appropriate in the global fitting routine. An additional fit was carried out that did not weight the data and this fit was found to yield statistically indistinguishable fit parameters. The autoionization timescales of the two states are the only relaxation channels considered in the fit. Typical fluorescence lifetimes are several orders of magnitude larger than the time scales probed in this work and are neglected. Coherent excitation and beating of the two j-states is also neglected as will be later justified.

The Gaussian instrumental response, σ_{cc}, is determined from the fitting to be 77 ± 2 fs (181 fs at FWHM), in agreement with the typical instrumental response from other experiments. The autoionization lifetime of the fast electrons, which represents the dynamics of the $j = 3/2$, is shorter than can be presently fit with confidence, thus in the fit this lifetime is assumed to be grouped together with the fitted instrument response time. The literature value places the lifetime of the $j = 3/2$ state at 50 ± 2 fs[12] which is faster than the experimental time-resolution. Theoretical calculations of the lifetime range from 24 to 70 fs.[83,87] The $j = 1/2$ state is resolved in time and found to have a best fit lifetime of $\tau_{1/2} = 140\pm13$ fs by fitting the slow electron signal. Static measurements of the $j = 1/2$ spectral width suggest an autoionization lifetime of 89 ± 6 fs.[12] The disparity between the 140 fs lifetime and that from spectral line width measurements may be due to the fact that the spectral fitting[12] is performed with a multi-parameter function. To fit such spectra, assumptions need to be made about the extent of interaction between resonances, coupled with knowledge of how many resonances contribute to the total signal, which is not always certain. The small splitting and non-negligible spectral overlap of the two j-split states, as well as another, presumably doubly excited, resonance (labeled 9 in Ref. 12) complicates the accurate fitting of these particular spectral lines. The doubly excited state is also presumably excited with the high-harmonic pump pulse, but this state is not probed in this experiment because the nearest continuum to which it can be ionized is 0.19 eV higher in energy than is accessible with the 801 nm probe pulse. Such a photoelectron signal would be well resolved from the single excitation states in the pump-probe photoelectron spectrum and would not influence the observed temporal evolution.

The total signal composition at each time delay is determined from Equation 3.2 using the transient signals shown in Figure 3.5(a). The time-dependent composition

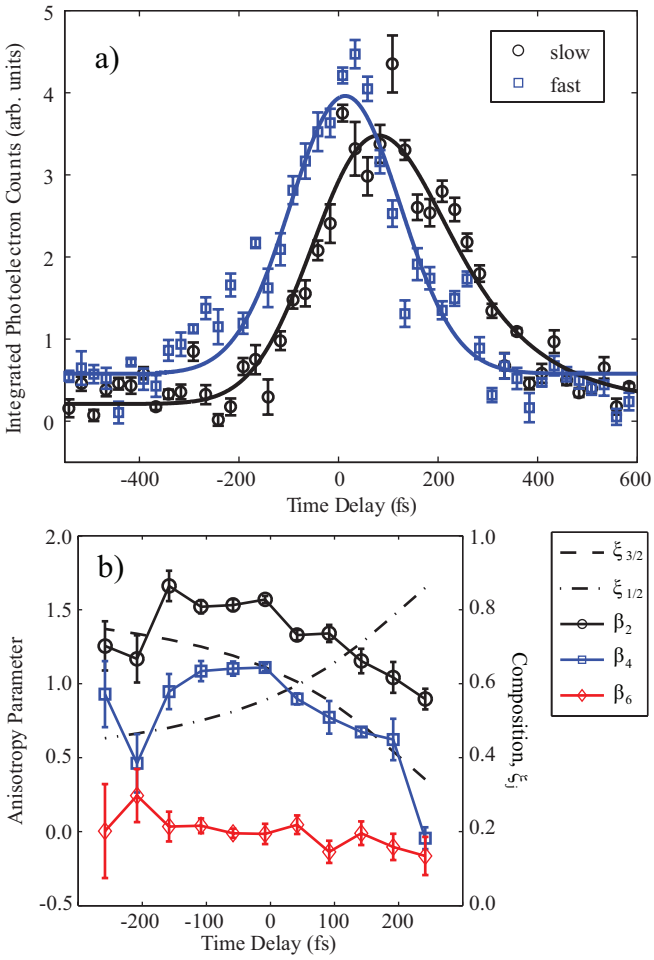

Figure 3.5: The integrated photoelectron signal from electrons in the 'fast' and 'slow' regions of integration are plotted versus time in (a) as described in the text. The regions of integration are defined in the text. Both curves are simultaneously fit to the convolution of a single exponential with the instrumental response time, to retrieve an autoionization lifetime of 140 ± 13 fs for the $j = 1/2$ state. The lifetime of the $j = 3/2$ state is not characterized with the current time-resolution. The anisotropy parameters expanded up to P_6 are shown in (b) along with the signal composition of the $j = 1/2$ and $3/2$ states as described in the text as dash-dotted and dashed lines, respectively. It is observed that as the composition becomes dominated by the $j = 1/2$ state PAD, the angular distribution becomes more isotropic.

curves are plotted in Figure 3.5(b) as dashed and dash-dotted curves for the $j = 3/2$ and $1/2$ states, respectively, obtained from the resulting fits after removal of a small vertical offset associated with each fit. A system of linear equations is written that relates the measured total anisotropy parameter, $\beta_{n,T}$, to the partial anisotropies, $\beta_{n,j}$,

or in other words, the anisotropy for each individual j-component in the mixture. The system of equations is written as

$$\begin{bmatrix} \xi_{1/2}(t_1) & \xi_{3/2}(t_1) \\ \xi_{1/2}(t_2) & \xi_{3/2}(t_2) \end{bmatrix} \begin{bmatrix} \beta_{n,1/2} \\ \beta_{n,3/2} \end{bmatrix} = \begin{bmatrix} \beta_{T,1/2}(t_1) \\ \beta_{T,3/2}(t_2) \end{bmatrix} \tag{3.3}$$

that is solved for every combination of time delays sampled in the experiment. Figure 3.5(b) shows the measured anisotropy parameters taken over a 5-bin width that is constrained to follow the maximum of the photoelectron signal with respect to energy versus time. The anisotropy parameters are then calculated by taking the weighted sum of the anisotropy parameters versus the photoelectron intensity at each time delay. For consistency, β_6 was included in all the inversions and plotted as diamonds in Fig. 3.5(b). Since the signal is a result of a two photon process, the inclusion of 6^{th} order and higher Legendre polynomials and expansion coefficients should not influence the results and must have an anisotropy coefficient of zero.

Total PADs can be extracted from the combination of 11 different time delays, which leads to 55 different solutions of the j-state resolved anisotropy parameters. This is carried out for both β_2 and β_4 anisotropy parameters. In the absence of noise, all solutions should be identical since each individual anisotropy parameter is expected to be time-independent.[27–29] Errors from the measured total anisotropy parameters are propagated through the solutions for Equation 3.3 resulting in individual anisotropy parameters that are independent of the time delays used in the solution within experimental uncertainty. A single constraint is applied to the solutions by requiring that the β_6 anisotropy parameter is equal to zero within the measured uncertainty for the two j-state anisotropies. This eliminates a few solutions based on β_6 from consideration since those anisotropy parameters are not physically meaningful for resonant two photon ionizations. Since the solutions to Equation 3.3 are consistent within their uncertainties, the particular solution with the smallest error should best represent the anisotropy parameter for the individual $j = 1/2$ and $3/2$ states. Anisotropy parameters for the $j = 1/2$ are then found to be $\beta_2 = 0.55 \pm 0.17$ and $\beta_4 = -0.01 \pm 0.10$, and the $j = 3/2$ state yields $\beta_2 = 2.19 \pm 0.18$ and $\beta_4 = 1.84 \pm 0.14$. The time delays used to quote these results are -58 fs and +142 fs. Error bars are determined by propagation of the measured total anisotropy parameter uncertainties through the solution of Equation 3.3.

It is assumed in the analysis that the two overlapping states create a total angular distribution that is a sum of the two individual angular distributions, and as such they can be deconvolved with only the assumption that the anisotropy parameters themselves are not time-evolving. The time-independence of the anisotropy parameters has previously been observed in work exploring the PADs of two-color two-photon excitation and ionization of helium[27] as well as in above threshold ionization (ATI) measurements on argon[28] and helium.[29] The broad bandwidth of the high-harmonic pump pulse provides adequate spectral bandwidth to prepare a coherent superposi-

tion of the j-split states.[88–90] If the superposition is probed to the same final state, the signal will contain a cross term that interferes the two excited states in the final continuum. This interference would influence the observed PADs such that the present analysis cannot be performed. However, since the ejected electrons from the $j = 1/2$ and $3/2$ states are expected to be of opposite spin, the electrons in the final continuum are not identical and will not interfere.[7,90] This allows for the separation of the PADs by the method described above without concern for wavepacket interferences. Additionally, the beat period for the superposition state is much longer than the autoionization lifetimes, which prevents its measurement. Spin-orbit interactions in the probe step may cause a breakdown of the $\Delta S = 0$ dipole selection rule, which might then allow interferences, but this is assumed to be negligible as a first approximation since the dipole matrix element connecting the excited state to a continuum with a spin-flip electron is expected to be small. The observed time-independence of the solution to Equation eq:lineq suggests that the decomposition of the total anisotropy into individual j-state components is reasonable and the influence of a wavepacket on the PADs is not readily observable. Angular distributions from coherent pumping of hyperfine levels has been reported,[11,22,23] but this effect is neglected in the current analysis as these interactions are assumed to be small and the time scales presumed to be long compared to autoionization. The opportunity to study the time-evolution of the Fano line shape has been proposed in several theoretical works,[91–95] which may exhibit interesting dynamics and PADs if probed in the time-domain. It is not obvious in this experiment what effect the line shape evolution plays on the development, as the current time resolution is only sufficient to clock the longer lived $j = 1/2$ state and the measurement is insensitive to the nearby double excitation state.

The influence of possible systematic errors being introduced in the determination of the composition curves in Figure 3.5(b) is explored by scaling the $j = 3/2$ transient amplitude by 70 percent relative to the retrieved fit amplitude. The scaling factor of 70 percent was chosen since the maximum contamination from neighboring photoelectron signals was estimated to be 30 percent based on the known resonance energies[12,31,32,86] and observed spectral widths. Scaling the transient amplitude of the $j = 3/2$ state slightly shifts the composition curve given in Figure 3.5(b), but it retrieves similar anisotropy parameters consistent with the quoted experimental results, within uncertainty. This implies that slight ambiguities in the composition of the transient photoelectron signal from the overlapping photoelectron signals weakly influence the extracted PADs within the present signal-to-noise. Future experiments with improved statistics will certainly observe such weaker influences. The observed results, however, have sufficiently small uncertainties to extract meaningful insight into the dynamics of the system.

3.3.2 Interpretation of the Photoelectron Anisotropies

It is not surprising that the photoelectron angular distributions measured for the ionization of the $j = 3/2$ and $1/2$ states yield anisotropies that differ significantly from one another. This is due to a combination of the different orbital alignment and electronic character that is probed by the ionization pulse,[22–24,26] and it is generally observed in the excitation and subsequent ionization of triplet atomic states when compared to analogous singlets, where the β_4 parameter changes from negative values to positive values as the orbital alignments relative to the probe polarization are changed. Results probing excited states of various atomic species below the ionization threshold report similar large differences in the PADs for singlet and triplet states.[18,20,22–24,26] These results, for example in atomic barium, share many similarities to the present work on Kr, as will be individually addressed for the $j = 3/2$ and $1/2$ states. Generally, the photoelectron anisotropies are described by a set of equations that assumes each excited state is a pure singlet or triplet state.[22,23] In the case of the singlet excitation ($j = 3/2$), the alignment of electron density is parallel to the pump and probe polarization, which allows for the ratio of radial dipole matrix elements and phase shift difference from the excited state to the final continuum partial waves to be extracted, as discussed in the section below. On the other hand, the excited triplet ($j = 1/2$ state) electron density is aligned perpendicular to the laser polarization, which results in anisotropy parameters that, in the present experiment, are independent of the microscopic ionization parameters that typically make up the PAD.[22,23] In the limit that the triplet $j = 1/2$ state is aligned perpendicular to the laser polarization and the angle between the pump and probe polarization is zero, the anisotropies are expected to reduce to $\beta_2 = 5/7$ and $\beta_4 = -12/7$.[22,23] Deviations from these values illustrate the influence of admixed electronic character into the excited and continuum states, as will be discussed further below in the section on the $j = 1/2$ state. Similar observations were made in experiments on barium and attributed to a departure from a single configuration excited state.[22,23]

Partial Wave Analysis of the $j = 3/2$ Anisotropy Parameters

Dipole selection rules uphold that $\Delta J = +1$ for transitions from the $^1S_0$ ground state. Also, $\Delta M_J = 0$ for linearly polarized light such that the only state populated must be a $6P_z$ state aligned parallel to the detector face (ie: $M_J = 0$) with an orbital electron distribution parallel to the pump and probe polarization. The probe photon ionizes the aligned singlet $j = 3/2$ state resulting in anisotropy parameters that can be written in terms of the ratio of radial dipole matrix elements, X, and the total phase shift difference, Δ, according to the equations:[27]

$$\beta_2 = \frac{\frac{2}{7} - X\cos\Delta}{\frac{X^2}{4} + \frac{1}{5}} \tag{3.4}$$

$$\beta_4 = \frac{72}{35}\left(X^2 + \frac{4}{5}\right)^{-1} \tag{3.5}$$

This permits the measurement of the PADs for the $j = 3/2$ state to provide the ratio of radial transition dipole matrix elements and the relative phase information. Since the aligned state is of P character, the outgoing dipole allowed partial waves are S and D waves with transition radial dipole matrix elements D_0 and D_2, respectively, connecting the excited state to the $4s^1 4p^6$ continuum.

The compositional analysis of the outgoing partial waves is performed by making use of Equations 3.4 and 3.5 with the individual state-resolved anisotropies assuming that LS-coupling selection rules reasonably represent the ionization step.[19,27–29,66] This characterizes the ratio of radial transition dipole matrix elements and phase shift difference between partial waves for ionization from the $j = 3/2$ autoionizing resonance. For the $j = 3/2$ state, this gives $X = 0.56 \pm 0.08$ and $\Delta = 2.19 \pm 0.11$ radians. The total phase shift difference is written as

$$\Delta = [\delta_{c,0} - \delta_{c,2}] + [\delta_{s,0} - \delta_{s,2}] \tag{3.6}$$

where $\delta_{c,l}$ is the Coulomb phase shift for the final electron angular momentum, l, given by[9]

$$\delta_{c,l} = Arg\left[\Gamma(l + 1 - i\epsilon^{-1/2})\right] \tag{3.7}$$

and $\delta_{s,l}$ is the scattering phase shift which is related to the quantum defect by[96]

$$\delta_{s,l} = \pi\mu_l \tag{3.8}$$

where ϵ is the electron kinetic energy in units of Rydbergs and μ_l is the angular momentum dependent quantum defect, which is a measure of electron screening in many electron systems. The Coulomb phase shift is analytically calculated for S and D waves with an electron kinetic energy defined by the measured electron kinetic energies of the $j = 3/2$ state, in this case the electron kinetic energies of range from 0.32 eV to 0.35 eV. The continuum quantum defect difference between the S and D partial waves is thus found to be -0.15 ± 0.03.

Addressing the extracted value of X first, it is observed that the D partial wave is preferred nearly 2:1 over the S wave when electrons are ejected from the $j = 3/2$ state. There is no general expectation for what the ionization of an aligned P state will yield in term of X; the prediction of X requires explicit calculation of the transition radial dipole matrix elements for the specific system and excited state considered. The excited state is mapped onto a continuum where additional state mixing may occur. Since no information is available that predicts the values of X for the $j = 3/2$ state, it can only be speculated as to what effects would influence the measured value. Two mechanisms are expected to influence X: spin-orbit interactions that the cause a deviation from LS-dipole selection rules and configuration mixing processes in both the excited and continuum states. Since X is built from transition dipole matrix

elements connecting the excited state to electron partial waves in the final continuum the value of β_4 is thought to be a sensitive probe of the excited state character without influences from the ion core scattering process. This is in contrast to β_2 where both X and Δ contribute to the measured value and thus the scattering due to other electrons in the atom plays a role through the phase shift difference.

Spin-orbit interactions result in a breakdown of the LS-coupling selection rules such that forbidden transitions to the final continuum become allowed, such as spin-flip transitions. These LS-forbidden excitations influence the values of β_n in a non-trivial way by addition of electron anisotropy contributions perpendicular to the probe polarization. This has a noticeable effect on single photon ionization of s-electrons from rare gas atoms where large deviations from $\beta = 2$ are observed.[19,25,66] These effects can be manifested through the simple breakdown of the LS-coupling selection rules or through excitation of an autoionizing resonance with triplet character associated with it. In these measurements LS-selection rules are assumed to be valid in the ionization step; ie: a given configuration will conserve spin when ionized. Admixtures of triplet character to the singlet (and vice-versa) through the spin-orbit interaction may introduce spin-flip contributions to the PADs that would otherwise be absent.[19,66] The singlet-triplet mixing of autoionizing krypton resonances has been addressed in the excitation and subsequent autoionization of $4s^1 4p^6 5p^1$ states. The spin-orbit interaction in the 5p state is found to only slightly influence the excited state by mixing a small amount of triplet character into the resonance.[12,13] This mixing of configurations becomes more important at higher n-Rydberg levels where the energy differences become vanishingly small. In the case of the $j = 3/2$ states probed in this work, the small energetic splitting of the two j-states implies singlet-triplet mixing may be an important contributing factor to the measured PAD.[19,66] The energetic region of the final continuum to which the excited states are probed is observed to be largely structureless.[82,97,98] This means that excitation by the probe pulse of an autoionizing state that has significant triplet character embedded in the $4s^1 4p^6$ continuum is not likely.

The final ion state has significant contributions from $4s^2 4p^4(^1D)4d^1$ configurations.[86] This implies that the independent electron picture of photoionization should break down and that double excitation character is mixed into the single excitation 6p states. Nearby doubly excited states[12,31,32] may also perturb the $j = 3/2$ and $1/2$ states. Related results probing perturbations on single excitation states by neighboring double excitations have been studied in experiments and calculations on atomic barium.[7,10,18,20] The results on barium demonstrate that admixtures of perturbing states drastically change the measured PADs when the configurations are mixed. The Fano configuration interaction that is responsible for the autoionizing resonance in the Kr states here greatly affects the excited state character by admixing continuum and nearby states over a relatively broad energetic region. Single photon excitation/ionization experiments on the $4s^1 4p^6 5p^1$ state of Kr indicate that the observed PADs from the 5p state are more influenced by admixtures of double

excitation character to the pure 5p resonance state than singlet-triplet mixing from spin-orbit interactions.[13] It is thus likely that the anisotropies measured in this experiment are similarly affected by nearby double excitation states.[12] The configuration mixing present in the autoionizing Kr resonances allows for additional mixing of the two j-split states as well as, to different extents, mixing with neighboring double excitation states.[12] This also implies that single electron approximations generally used to describe photoionization are expected to incorrectly predict the PADs.[28]

It can only be speculated from this individual experiment and the expected configuration mixing processes what factors will contribute to the measured values of X, providing a guide for future theoretical work. Probing higher n-Rydberg states should provide additional insight into the composition of various states, and theoretical modeling of the excited state and ionization steps will certainly aid in unambiguously identifying and quantifying the influences on the PADs in these autoionizing states.

The continuum quantum defect difference for the individual $j = 3/2$ state alone does not provide significant insight into electron-electron interactions that take place upon ionization. There is no known theory for which the present results can be compared. As a first approximation, if an average value of the quantum defect difference of the $4s^1 4p^6 \mathrm{n}s^1$ and $4s^1 4p^6 \mathrm{n}d^1$ states below the ionization threshold is considered, an estimated value for the continuum quantum defect difference is found to be -0.03 ± 0.19 using the resonance energies in Srivastava et al.[98] and -0.16 ± 0.07 using the values of Yuan et al.[82] Both values are in good agreement with the continuum quantum defect value measured here of -0.15 ± 0.03. This assumes that the quantum defect difference is energy independent across the series and that perturbations of the energetic locations of the resonances are small. The first assumption is typically valid especially for higher n-Rydberg states; the second assumption may not hold, but serves to approximate the value for at least a qualitative comparison. For significantly more insight into the quantum defect difference it will be important to measure higher-lying Rydberg states and compare the results to calculations as a test of photoionization models.

Anisotropy of the $j = 1/2$ State

The $j = 1/2$ state correlates to a $^3P_1$ term in LS-coupling, meaning the spin of the 4s electron that is excited must flip from the ground state $^1S_0$ configuration. This affects the alignment such that the electron density is no longer parallel to the light polarization, as was the case in the $j = 3/2$ state, but is perpendicular to the light polarizations.[22–24,26] Due to the different alignment and electronic configuration, a different set of equations than those given in Equations 3.4 and 3.5 must be used to decompose the anisotropies into X and Δ.[22,23] These previously derived equations reduce to constants when the angle between the pump and probe polarizations is set to zero, as is necessarily the case for VMI experiments. This framework assumes that a

pure triplet excited state is excited, aligned, and probed, resulting in anisotropies that reduce to exactly $\beta_2 = 5/7$ and $\beta_4 = -12/7$, which are independent of electron kinetic energy and the identity of the atomic species.[22,23] All terms that are system-specific, such as X and Δ, cancel out when the pump and probe pulses are linearly polarized and parallel to one another. Since these expectations are based on a pure configuration excited state, deviations from these values should represent the combined effects of configuration mixing and spin-orbit interactions in the excited and final states. The anisotropy parameters for the $j = 1/2$ are found to be $\beta_2 = 0.55 \pm 0.17$ and $\beta_4 = -0.01 \pm 0.10$ which depart from the expected values especially in β_4.

A similar departure from the predicted anisotropies is observed in atomic barium where singlet and triplet $6s^1 6p^1$ configurations are populated below the ionization threshold and subsequently probed.[22,23] In barium, the measured values are found to be $\beta_2 = 0.61 \pm 0.05$ and $\beta_4 = -0.81 \pm 0.06$, which also clearly depart from the expected values.[22,23] Interestingly enough, the barium results also show a larger deviation of β_4 from the prediction than is observed for β_2, as is the case for krypton here. In general, the β_4 parameter is extremely sensitive to the alignment of the excited state relative to the probe polarization and any admixed electronic character to the excited or final states will greatly vary the composition of outgoing electron partial waves.[19,66] A combination of configuration mixing and spin-orbit effects may be significantly at play. Detailed theoretical attention is needed to quantify the origin of these departures on the measured anisotropy parameters, but the factors presumed to influence the values can be discussed on a more qualitative basis.

The measured β_4 parameter for the $j = 1/2$ state is essentially zero, which might lead one to believe that the state is not aligned, but rather the state is anisotropic such that parameters only up to β_2 need to be considered in the expansion given in Equation 3.1. The pure $j = 1/2$ state is expected to be completely aligned perpendicular to the probe laser polarization due to dipole selection rules. A similar alignment has been observed in other triplet excitations and subsequent ionizations.[22–24,26] One should not be confused by the nomenclature used in this report which describes the valence electron as $j = 1/2$; the total angular momentum is $J = 1$ for the excited electron and ion core, which is, in principal completely aligned. Admixtures to this state might lessen the degree of alignment, which would be manifested most dramatically in β_4, but will not necessarily eliminate the initial alignment altogether. The degree of initial alignment is not directly measured in this work, but analogous results in atomic Yb illustrate the influence of alignment on the β_4 parameter where enhanced alignment yields more anisotropic distributions.[24] The alignment of the admixed excited state induced by the pump pulse will certainly influence β_4 but these admixtures will also contribute to the measured anisotropy in the probe step.

The result of the admixed character to the pure triplet state, when probed with the ionization pulse, is to add anisotropies with different weighting factors (cross sections) to the anisotropy of the pure $j = 1/2$ state. This is given as a weighted, incoherent sum over all the individual anisotropies that construct the measured anisotropy for

the $j = 1/2$ state.[19,66] Quantitatively determining the contributions to the measured anisotropy is not possible in this experiment because the total number of contributions, the weighting of each contribution, and the values of the anisotropies for each channel are not known. Contributions are expected to occur from intermediate and final state configuration mixing as well as from spin-orbit effects. The $j = 1/2$ state might be expected to have more double excitation character compared to the $j = 3/2$ state, since it is energetically closer (by the 14 meV spitting) to a lower energy double excitation state;[12,31,32] without explicit calculations this can only be speculated on. A comprehensive theory that accounts for the excited state wavefunction and the ionization to an admixed continuum is required to ascertain the role of the configuration mixing and spin-orbit effects on the PADs for the autoionizing resonances in krypton.

The measured anisotropies from the j-spit levels are significantly different. The different alignment and electronic structure give two different sets of equations that describe the anisotropies in terms of microscopic photoionizaton parameters.[22,23] It is presumed that the $j = 3/2$ state PAD results from admixtures of double excitation states and triplet character that influence the measured anisotropies. These effects are thought to be present based on previous work and theoretical calculations that describe the excited and continuum states.[13,86] There is no theoretical work for which a comparison of the presently measured PADs can be applied, although experiment determinations of bound state quantum defect difference[82,98] agree favorably with the presently measured continuum quantum defect difference. The measured values of the $j = 1/2$ PADs can be compared to a single configuration (pure triplet) prediction, which allows for a clear illustration of the effect of mixed configurations on the measured anisotropies, although at what step the configuration mixing is most important (pump or probe pulses) is not clear, and precisely what influences are dominant in the measured PADs require theoretical assistance to determine. The deviations from the pure triplet PAD are presumed to be from the configuration interaction and spin-orbit effects that admix neighboring electronic state character into the autoionizing resonance. Both phenomena are known to be present and important in describing these short lived autoionizing resonances. Theoretical attention is desirable to precisely ascertain what contributions make up the measured PADs for both $j = 1/2$ and $3/2$ states.

3.4 Conclusion

The femtosecond evolution of a pair of autoionizing $4s^1 4p^6 6p^1$ ($j = 1/2$ and $3/2$) states are tracked using high-harmonic pump and an 801 nm probe pulse to eject photoelectrons detected in a VMI spectrometer. This allows for the simultaneous acquisition of the energy, angle and decay observables that characterize the excited system. This also permits the retrieval of the PADs from individual states that are spectrally overlapped. Direct measurement of the $j = 1/2$ autoionzation lifetime

($\tau_{1/2} = 140 \pm 13$ fs) is found to differ from the previously measured spectral width observed in high-resolution experiments.[12] The measured anisotropy parameters from the $j = 3/2$ state yield the ratio of radial dipole matrix elements and the phase shift difference between these partial waves. The preferential ejection of D partial waves is observed in approximately a 2:1 ratio relative to the S waves for ionization of the $j = 3/2$ state. Different mixtures of continuum and double excitation character are presumed important to the final outgoing dipole matrix elements, but these are not distinguishable from spin-orbit effects. The measured quantum defect difference of -0.15 ± 0.03 agrees favorably with estimated continuum quantum defect difference from electron impact experiments.[82,98] Direct comparison to a theoretical model is desirable to more quantitatively assess the influences of resonance mixing and spin-orbit effects on the PADs.

The measured PADs from the $j = 1/2$ state significantly depart from expected values of $\beta_2 = 5/7$ and $\beta_4 = -12/7$ predicted by a single configuration model.[22,23] The deviation is thought to be a result of configuration mixing with the nearby $j = 3/2$ singlet state and double excitation states, which appear to influence the measured values of β_4 the most. This can be attributed to admixtures in the excited state wavefunction that may influence the excited state alignment and ionization propensities of electrons into the continuum. Theoretical attention to this problem would assist in the unambiguous determination of the excited state characters and lead to a more complete understanding of the excited state relaxation and photoionization processes. The results presented here should also help test rigorous theoretical predictions of photoionization of autoionizing states, which represent an interesting set of physical problems. Recently acquired results probing higher n-Rydberg states in Kr are currently under consideration in an effort to quantify the effects on the PADs as a function of principal quantum number.

Chapter 4

Ultrafast Relaxation Channels of Superexcited $c\ ^4\Sigma_u^-\ nl\sigma_g\ v = 0, 1$ States of O_2 Probed with Femtosecond Photoelectron Velocity Map Imaging

Neutral superexcited states (SESs) converging to the $O_2^+\ c\ ^4\Sigma_u^-$ ion core are excited and probed with femtosecond time-resolution to track the competitive predissociation and autoionization decay channels. The $c\ ^4\Sigma_u^-\ nl\sigma_g\ v = 0, 1$ SESs are excited with a single high-harmonic photon centered at 23.10 eV. The SESs and neutral atomic products are ionized by a time-delayed 805 nm probe pulse. The ionized electrons from atomic $4d^1\ ^3D_J^\circ$, $4p^1\ ^5P_J^\circ$, and $3d^1\ ^3D_J^\circ$ fragments are detected using velocity map imaging to reproduce the known electron binding energies for the atomic fragments of 0.87 eV, 1.34 eV and 1.52 eV, respectively, relative to the ground O^+ ion state. Using principles based on the ion core dissociation model to make assignments, it is plausible that the $4d^1\ ^3D_J^\circ$ fragment is formed on a timescale of 65 ± 5 fs and is a photoproduct of the $4s\sigma_g\ v = 1$ SES. The $4p^1\ ^5P_J^\circ$ fragment is formed on the timescale of 427 ± 75 fs and is most likely attributed to the neutral predissociation of the $4s\sigma_g\ v = 0$ SES. The temporal development of the $3d^1\ ^3D_J^\circ$ fragment is not unambiguously resolved due to overlap with the simultaneous decay of a $v = 1$ SES decay signal. These results are in good agreement with previous experimental and theoretical efforts that probe the ion core predissociation lifetimes for $v = 0, 1$ SESs via line widths and calculations. An unidentified molecular state is inferred by the observation of a long-lived autoionization depletion signal connected to the $B\ ^2\Sigma_g^-$ ion state. The origin of this signal is not identified; it is persistent up to time delays

of 105.09 ps, limiting the likelihood that the origin of the depletion signal is from a populated SES based on previous high-resolution measurements of the predissociation lifetimes of the molecular ion core. Future work is needed to identify the nature of this excited molecular signal.

4.1 Introduction

Molecular superexcited states (SESs) are neutral excited electronic configurations embedded in the ionization continuum. These states decay predominantly through autoionization and neutral predissociation channels. The neutral dissociation pathway is often thought to be dominated by the bond breaking dynamics of the ion core and is independent of the nature of the excited electron (ie: the excited electron is a spectator).[35–39,41,99–103] On the other hand, autoionization, which is a purely electronic process, couples the SESs to various excited ion cores and a continuum electron that carries away excess kinetic energy. The competition between these two channels determines the dominant decay mechanism and results in important processes that occur in the atmospheric chemistry of Earth and other terrestrial bodies in the solar system.[104]

The experiments presented here study a series of SESs that converge to two different vibrational levels of the O_2^+ $c\,^4\Sigma_u^-$ ion core, the $v = 0$ and $v = 1$ states, in molecular oxygen.[35–39,41,99–103,105] The ground state oxygen configuration of molecular oxygen is given by $2\sigma_u^2 3\sigma_g^2 1\pi_u^4 1\pi_g^2$ ($X^3\Sigma_g^-$), which is excited to the $2\sigma_u^1 3\sigma_g^2 1\pi_u^4 1\pi_g^2$ ($c^4\Sigma_u^-$) $nl\sigma_g^1$ ($^3\Sigma_u^-$) $v = 0, 1$ state by a single photon. The O_2^+ $c\,^4\Sigma_u^-$ ion core is quasibound, with a predissociative lifetime that is dependent on the vibrational level excited. The dissociation dynamics of the ion core are responsible for the neutral predissociation of the SES since the valence electron is expected to act as a spectator to the nuclear dynamics. This results in dissociation products that conserve the principal quantum number, n, from the molecular state to the atomic Rydberg product.[35–39,41,99–103] This is depicted in Figure 4.1 and generally termed as the ion core dissociation model. The dissociation partner of the atomic Rydberg state is typically the ^3P ground state or the first excited ^1D atomic oxygen state; for the energetically high lying SESs probed in this work, the dissociation fragment is the ^1D partner fragment.[103] These fragments are not measured in this experiment, but numerous fragmentation partners are possible for the highly excited neutral atom that is detected in this work based on the Wigner-Witmer correlation rules for homonuclear diatomics.

The O_2^+ $c\,^4\Sigma_u^-$ $nl\sigma_g$ $v = 0, 1$ states are abbreviated as $nl\sigma_g$ $v = 0, 1$ states for remainder of this chapter. It should be noted that the absolute assignment of these states is somewhat inconsistent in the literature. Some reports assign the nd SESs as $nd\sigma_g$ $v = 0, 1$ states, while others assign the same resonances as $nd\pi_g$ $v = 0, 1$.[99,106] The absolute assignment of these states is not the goal of this work; for the analysis presented here, the determined values of nl for each SES, which are well documented

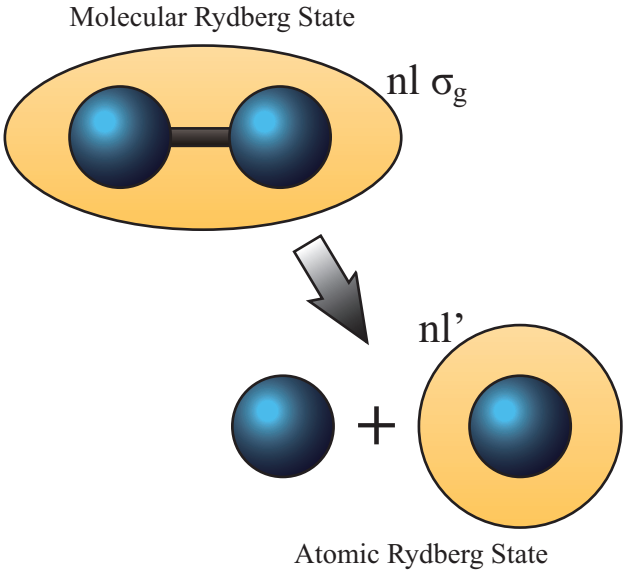

Figure 4.1: The ion core dissociation model is illustrated here. In this model, the superexcited valence electron, described by $nl\sigma_g$, is delocalized over both atomic centers, as indicated by the shaded region surrounding the diatomic molecule. The molecule then breaks apart governed by the predissociation of the molecular ion core and is independent of the character of the electronic state. At a certain nuclear separation, the excited electron is localized on a single atomic fragment where the principal quantum number, n, is conserved from the molecular state to the atomic fragment.

and reasonably consistent in much of the literature, is all that is necessary. The relevant SESs, atomic fragments, and ion states to which the SES can be probed or by autoionization are is illustrated in Figure 4.2.

While the valence electron is not expected to participate in the dissociation, it should influence the autoionization contribution to the total SES lifetime and it is used to act as a reporter of the dynamics of the SES decay when probed. The SES lifetime for a given vibrational level is the inverse of the sum of the inverse lifetimes for each decay channel. Explicitly, it can be written as

$$\frac{1}{\tau_{ses}} = \frac{1}{\tau_{ai}} + \frac{1}{\tau_{pd}} + \frac{1}{\tau_{fl}} \tag{4.1}$$

where τ_{ses} is the lifetime of the vibrational SES, τ_{ai} is the lifetime of the autoionization channel, τ_{pd} is the neutral predissociation lifetime, and τ_{fl} is the fluorescence lifetime. Since the dynamics of the ion core are thought to dominate the predissociation, the nature of the electronic state (ie: $ns\sigma_g$ or $nd\sigma_g$ states) should not effect τ_{ses} unless τ_{ai} is much shorter than the τ_{pd}. The value of τ_{ai} is system dependent and can

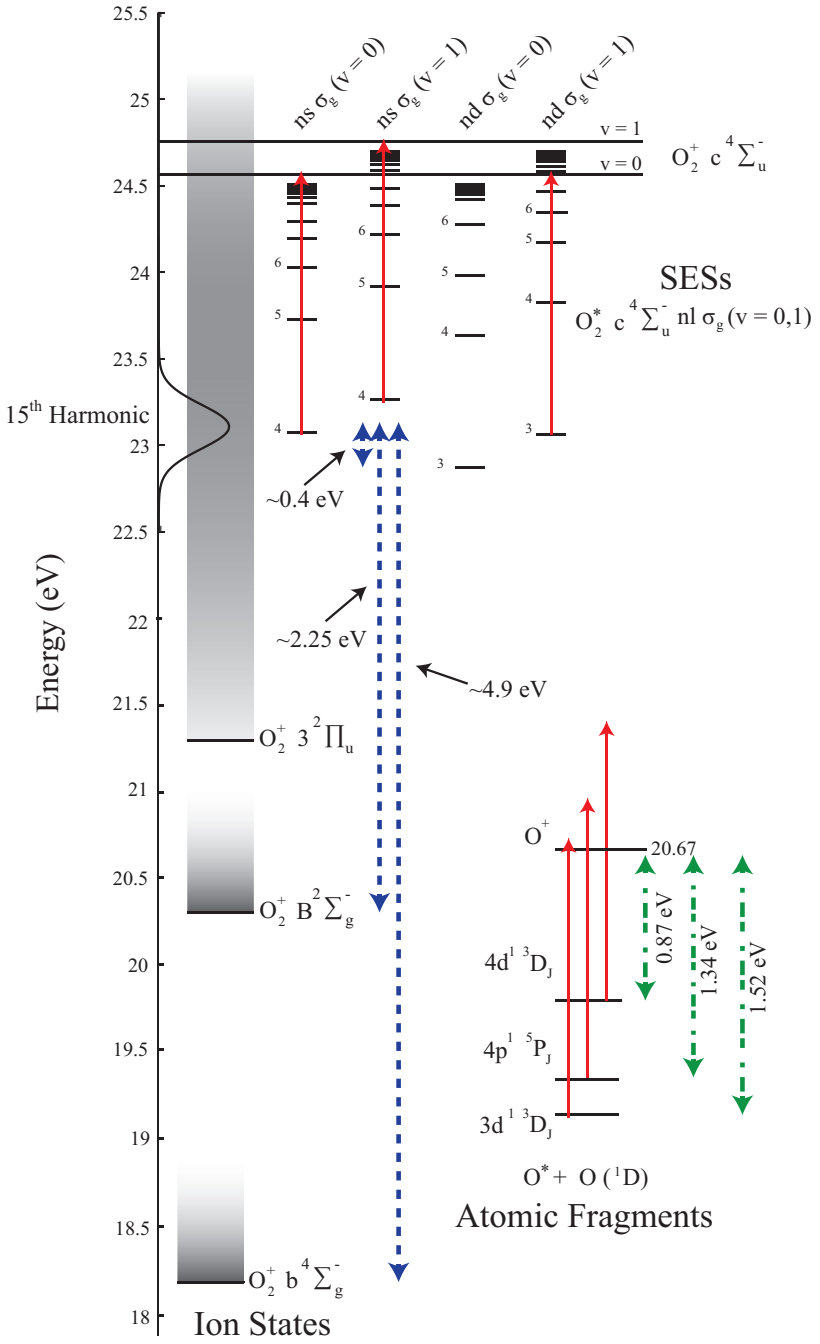

Figure 4.2: The relevant SESs converging to the O_2^+ $c\ ^4\Sigma_u^-$ ion core are depicted along with the atomic and molecular ion states relevant to the signals observed in this work. The high-harmonic spectrum is plotted along the vertical energy axis to illustrate the resonances excited within the pump pulse spectral bandwidth ($\sim$ 0.3 eV). These states can autoionize to various ion states (depicted as dashed lines) or predissociate to neutral fragments (binding energy shown as dashed-dotted lines). The SESs and neutral fragments are probed with a delayed 805 nm ionization pulse to eject an electron which is measured in this experiment.

take on values ranging from nanoseconds to attoseconds depending on the coupling between the discrete and continuum channels. A time resolved experiment affords the opportunity to test the assumptions of the ion core model for low n SESs since the observed lifetime of the SES should be identical to the ion core predissociation lifetime in the limit that the valence electron is non-interacting. The observed rise and decay of signals presented in this work are much faster than the typical fluorescence lifetime, effectively eliminating radiative relaxation as a contributing relaxation channel.

Since the dynamics of the SES are intimately tied to the predissociation of the ion core, it is useful to review some critical aspects of the ion core dynamics. Significant attention has been paid to the spectroscopy, dynamics, and product yields of these states, but widely varying values of the ionic O_2^+ $c\ ^4\Sigma_u^-$ $v = 0$ vibrational ion state lifetime have previously been reported.[35–39,41,99,99–103,107–112] Experiments studying the line widths suggest that the lifetime of the neutral $v = 0$ SES is on the order of 270 fs to 1 ps.[39,41,99] The most recent theoretical calculations indicate that the lifetime of the $v = 0$ ion state should be on the order of 10 ps,[37,38,40,99,101] which is generally at least one order of magnitude larger than experimental results. On the other hand, a general consensus from both experimental and theoretical efforts has determined that the lifetime for the the $v = 1$ level of the $c\ ^4\Sigma_u^-$ ion state is on the order of 60 fs to 70 fs.[36–39,41,99–102] The experiments presented here will address the neutral SESs.

Turning attention back to the SESs that converge to the $c\ ^4\Sigma_u^-$ ion states, there are differences between the dynamics of the SES and that of the ion state. The main difference of the SES decay as compared to the dynamics of the ion core, is that autoionization is an accessible channel to the SES for decay. Given that autoionization lifetimes are often very short, on the order of attoseconds to picoseconds, it is expected that the lifetimes of the SES might differ from the predissociation lifetime of the ion state.

There are difficulties encountered in high-resolution measurements that study SESs in the frequency domain. Specifically, there is difficulty in measuring natural line widths for an optical transition in which rotational and vibrational progressions are overlaid and not spectrally resolved. This can hinder the accurate determination of the natural line width for a given state. High-resolution photoabsorption and photoionization experiments also must address the Fano line shape that is associated with each resonance. This is because the neutral SES couples via autoionization to several direct ionization continua, which interfere and create an asymmetric spectral profile.[14,16,73] This can complicate the interpretation of the SES line widths and therefore the SES lifetimes. Theoretical calculations face similar challenges in that inclusion of all the necessary potential energy surfaces and the couplings between them, which lead to curve crossings, must be incorporated, in a high energy regime where numerous states exist.[113]

Additionally, determining the nascent atomic products of the predissociation can be complicated by atomic fluorescence cascades that may not be observed in the experimental detection window (ie: the frequency range that is measured by the detector).

Previous work studying SESs in molecular N_2 has shown that detecting atomic fluorescence alone may not lead to a correct understanding of the excited state decay channels and nascent product distributions.[84] Related work observing visible/near-infrared atomic fluorescence from the dissociation products of the $nl\sigma_g$ $v = 0, 1$ states in O_2 also shows this effect,[103] compared to experiments where only ultraviolet radiation is collected.[35,36]

Pump-probe experiments in the femtosecond time regime can aid in determining the SES lifetimes and decay dynamics and will identify nascent products from the neutral dissociation channel, which gives a complementary understanding of the relaxation dynamics. The excitation and decay of the SESs can be tracked by probing the excited electron over time using a second probe pulse to ionize the SES to a final continuum. The transient behavior of the SES signal will yield the SES lifetime when fit to an appropriate kinetic model suggested by high-resolution measurements of the ion core dissociation. By fitting the transient signal versus time, the number of adjustable parameters is reduced compared to fitting several resonances simultaneously in the frequency domain.[30] Such a measurement also eliminates problems in detecting the large range of atomic fluorescence (from infrared to ultraviolet) that can be emitted from excited atomic products. This is because, on the femtosecond time scale, the excited atoms do not have time to radiatively decay to a detectable extent. This eliminates difficulties caused by cascading fluorescent processes and can allow for the determination of the nascent products, but it introduces limitations on the atomic fragments that can be probed based on the choice of the ionization laser frequency and spectrometer resolution.

The experiment presented here populates neutral SESs in the energy range of $\sim$ 22.75 to 23.5 eV. Specifically, vibrational levels of the $ns\sigma_g$ and $nd\sigma_g$ state are pumped using the 15^{th} harmonic of a femtosecond laser pulse centered at 805 nm. Within the pump-pulse spectral bandwidth ($\sim$ 0.3 eV) are the $4s\sigma_g$ $v = 0$, $4s\sigma_g$ $v = 1$, $3d\sigma_g$ $v = 0$, and $3d\sigma_g$ $v = 1$ states. The $3d\sigma_g$ $v = 0$ state is not expected to be populated significantly due to the smaller excitation cross section to the $nd\sigma_g$ $v = 0$ states at lower n[99] and the lower spectral intensity of the excitation-pulse at this energy as compared to the other three states (see Figure 4.2). The ionic $c\ ^4\Sigma_u^-$ state can support an extremely short lived $v = 2$ level, but the excitation cross section of this vibrational level based on the FC factors is $\sim$67 times weaker then the $v = 0$ transition and $\sim$30 times weaker than the $v = 1$ transitions.[105] Evidence for the $v = 2$ vibrational levels is not observed in the present work and $v = 2$ is SESs are neglected in the analysis that follows. A time-delayed 805 nm (1.54 eV) probe pulse ionizes the transiently excited SESs and probes the neutral atomic products that are produced to retrieve the SES lifetimes and nascent products. Some of the populated SESs are probed to the O_2^+ $c\ ^4\Sigma_u^-$ core to eject a low kinetic energy electron that is measured with a photoelectron velocity map imaging (VMI) spectrometer. Neutral atomic Rydberg states are simultaneously detected and their electron binding energies recorded.

The results presented here use the ion core dissociation model to tentatively assign neutral fragments to the SES from which they originated. The femtosecond time-resolution is used to further correlate products with vibrational SESs by relating signals with similar lifetimes to one another in a simple kinetic model.

4.2 Experimental Details

The experimental apparatus is analogous to those used in previous work.[27–29,67,84] Only the critical aspects of this system will be described here. A Spectra-Physics Spitfire Pro amplified Ti:Sapphire laser producing 2.5 mJ pulses at 1 kHz with a pulse duration of $\sim$ 50 fs centered at 805 nm is split into a pump and a probe arm. High-order harmonics are generated by focusing 770 mW average power into a 1.5 mm path length gas cell filled with argon with two 200 μm holes drilled on either side. The generated harmonics co-propagate with the residual fundamental laser light into a home-built monochromator designed to select and focus a single harmonic order into the interaction region. The separation is achieved by the use of a plane grating, cylindrical mirror and toroidal mirror followed by a slit. This allows for the 15^{th} harmonic with energy centered at 23.10 eV and spectral width of approximately 0.3 eV to be used as a pump pulse. The spectral width is determined from the single photon ionization of atomic calibration gases such as argon. The pump pulse overlaps a skimmed effusive beam of O_2 at room temperature.

A time-delayed 805 nm (1.54 eV) probe pulse intersects the pump and O_2 beams at a small angle to ionize the excited molecular and atomic species. The average power of the probe pulse was set at 650 mW and is low enough to avoid multiphoton ionization. This minimizes strong field effects[85] that would complicate the analysis. Time delays are taken in the range of -1.91 ps to +105.09 ps. The smallest delays (10 fs) were taken near $t = 0$, with more coarse delays ($\sim$ 500 fs to 1000 fs) sampled at longer delays to establish the asymptotic temporal behavior. Negative times correspond to delays where the 805 nm probe pulse arrives at the sample before the harmonic pump pulse, while positive times are when the probe pulse arrives after the pump pulse.

The ejected photoelectrons are collected using a particle counting velocity map imaging spectrometer, which projects the 3-dimensional electron cloud onto an imaging quality microchannel plate (MCP) detector coupled to a phosphor screen.[54,55] The phosphor screen releases a burst of light when an electron is incident on the MCP and that light is subsequently recorded by a CCD camera running at a 60 Hz frame rate. The center of mass of each event is recorded as an x and a y coordinate for reconstruction of the images off line. Approximately 300 frames of pump-probe and background (harmonic only) data are alternately collected at 5 second intervals for every time delay sampled. The time delays are scanned in a linear manner from positive times to negative times, then once the limit is reached at the negative limit, the delay reverses back to positive times. This can introduce some systematic error due

to experimental drift depending on how many time delays are sampled and how long the experiment needs to acquire data for. To minimize systematic error while maintaining a fast rate of data acquisition by moving the delay stage as little as possible from time step to time step (ie: not taking random time steps where the delay stage would have to move long distances between each delay), the hundreds of iterations at a single time delay are co-added into final images, which are then analyzed after the experiment is completed. These images are then angle integrated to retrieve the radial distribution. In this chapter, the *projected* photoelectron image is analyzed, which provides energetic information on the system as it evolves over time. This is not to be confused with inverted photoelectron images, which are obtained when the inverse Abel transform is performed on the raw data. The kinetic energy is calibrated with known binding energies of rare gas atoms.[56] In all cases, error bars correspond to one standard deviation. The data is collected continuously for approximately 6 days to achieve an acceptable signal-to-noise in the time-resolved photoelectron spectrum.

The inverse Abel transform is not performed on the images due to the large negative (depletion) signals observed at early time delays. The problems associated with inversion of negative signals is not currently addressed in the literature,[58–64] but will be critical to the advancement of time-resolved VMI experiments with large backgrounds and contributions from depletion signals. This is a non-trivial challenge that might best be addressed with an onion-peeling technique[58] that is designed to address the depletion signals that exist at higher kinetic energies. A similar approach might be possible using a basis set expansion with depletion basis functions included. Alternatively, a percentage of the background can be subtracted, rather than complete subtraction, to avoid negative features, which can then be treated with conventional inverse Abel transform techniques. This approach has been performed in above threshold ionization experiments on argon and helium with success.[28,29] In a similar vein of thought, a time-dependent background subtraction scheme can be applied to molecular states to accomplish a similar result with the added flexibility of not 'under-subtracting' the background at longer time delays where little depletion signal is present. For the purposes of this analysis, the radial distributions are sufficient to extract meaningful insight into the decay of the SESs.

4.3 Results and Discussion

4.3.1 Time-Resolved Photoelectron Spectrum

The angle-integrated time-resolved photoelectron spectrum is given in Figures 4.3 and 4.4. Multiple signals are simultaneously observed with positive and negative intensity signatures; positive features are from the probe pulse ionization of SESs and neutral atomic products, while negative features are a result of probing the SES before autoionization couples the SES to a continuum electron and an excited ion

core. The depletion signals correspond energetically to suppression of autoionization by probing the prepared SES before relaxation to the $B\ ^2\Sigma_g^-$ and $b\ ^4\Sigma_g^-$ ion states, with expected vertical binding energies of 20.30 eV and 18.17 eV, respectively.[105] This correspondingly results in electrons with an expected kinetic energy of 2.80 eV and 4.93 eV. The observed photoelectron depletion signals are measured to be in the kinetic energy range between 1.48 eV and 2.95 eV when the $B\ ^2\Sigma_g^-$ ion core is considered. The depletion signal from the $b\ ^4\Sigma_g^-$ ion core is observed to be in the electron kinetic energy range between 3.80 eV and 5.91 eV. Both observations agree well with the expected ionization energies given above.[105]

The next highest ion core is the $^2\Pi_u$ state with a vertical excitation energy of 23.90 eV. This ion state has a very wide spectral distribution, but a significantly weaker excitation cross section compared to the $B\ ^2\Sigma_g^-$ and $b\ ^4\Sigma_g^-$ ion states.[105] This is due to the Franck-Condon (FC) region for excitation lying energetically above the dissociation limit for this state. In fact, the excitation cross section to this ion core is estimated to be at least 10 times smaller than the neighboring $B\ ^2\Sigma_g^-$ and $b\ ^4\Sigma_g^-$ ion states cross sections. Considering the weaker excitation cross section and the difficulty in measuring depletion signals in general, it is not expected that a significant contribution to the time-resolved photoelectron spectrum would be observed from this state.

Thus, the dominant signals at low electron kinetic energies are expected to be largely from atomic and SES states that are ionized with the probe pulse. Since the inverse Abel transform is not performed on the images, there might be some effect of overlapping intensity from higher electron kinetic energy features being projected onto the lower kinetic energy signals. To assess this contribution, a simulated photoelectron image is created with an isotropic electron distribution, which is projected onto a plane representing the imaging MCP detector. The radius of this distribution is set to correspond to the observed photoelectron signal for the $B\ ^2\Sigma_g^-$ ion state. At radii that represent atomic and molecular photoproducts, it is estimated that the largest kinetic energy features observed, namely the signal centered at 0.67 eV electron kinetic energy, would be overlapped with $\sim 17\%$ of the maximum intensity of the $B\ ^2\Sigma_g^-$ direct ionization signal. This is the case when both signals are present with equal intensity, which is not observed in the experiment (see Figures 4.3 and 4.4). In fact, the depletion signal is estimated to be more than a factor of two smaller in intensity, reflecting the difficulty in measuring a small signal on a large background. This means that the estimated $\sim 17\%$ overlap is an upper limit to the effect of overlapping states due to the VMI projection; a more realistic number is expected be smaller than $\sim 10\%$ based on the relative intensities.

Given that the effect of overlapping states at higher kinetic energies is small, if a simulated photoelectron signal is added to the simulated background image, the resulting photoelectron spectra of the lower energy feature is not significantly altered. This means that features in the photoelectron spectrum observed at low kinetic energy can be assigned with confidence. The overlapping signal from the $^2\Pi_u$ state, based on

the lower excitation cross section[105] is not observed with the present signal-to-noise since it is estimated to be a factor of 10 smaller in intensity.[105] This state might have a small effect on the time-resolved signal, as will be addressed later, but should not influence the assignment of the photoelectron spectral features.

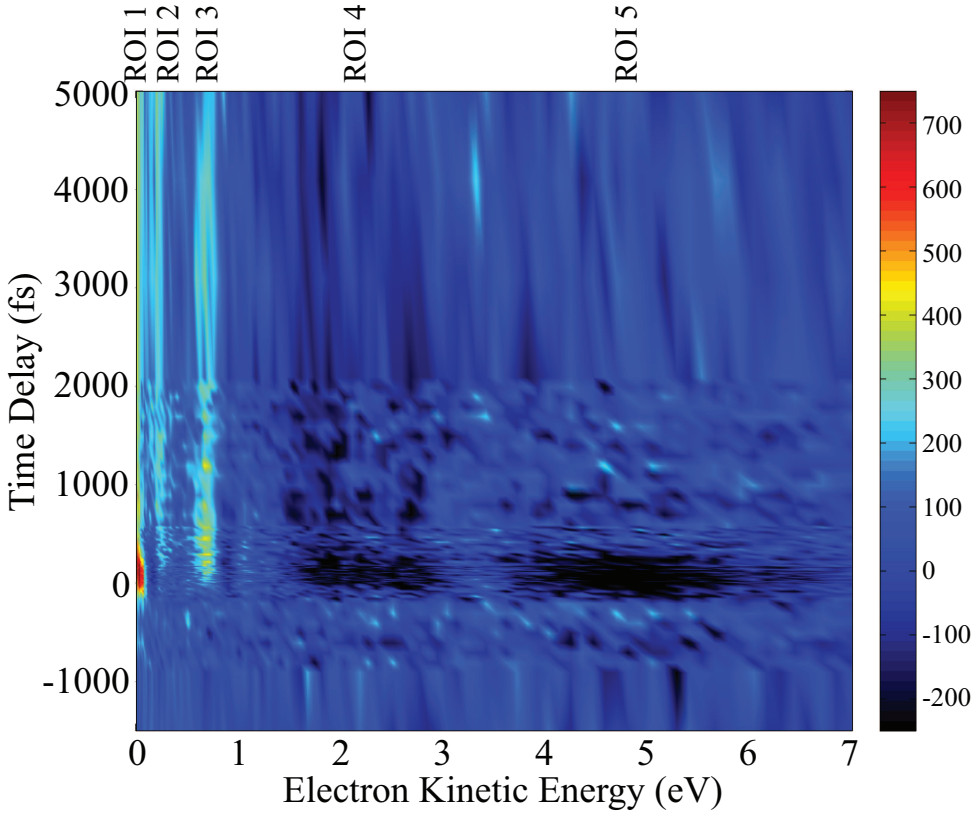

Figure 4.3: The time-resolved photoelectron spectrum is plotted here for all observed photoelectron kinetic energies. The positive signals are SESs and atomic products that are probed with the time delayed 805 nm probe pulse. These are described individually in the text and tabulated in Table 4.1. Negative signals (or depletions) are a result of probing a SES before it can autoionize; this suppresses the decay, and the result is observed as a depletion relative to the signal that would be observed if the probe pulse had not ionized the SES. The low kinetic energy depletion signal is attributed to electrons that would have autoionized to the $B\ ^2\Sigma_g^-$ ion core with electron kinetic energies between 1.48 eV and 2.95 eV. The other depletion signal is from electrons that would have autoionized to the $b\ ^4\Sigma_g^-$ ion core in the electron kinetic energy range between 3.8 eV to 5.91 eV.

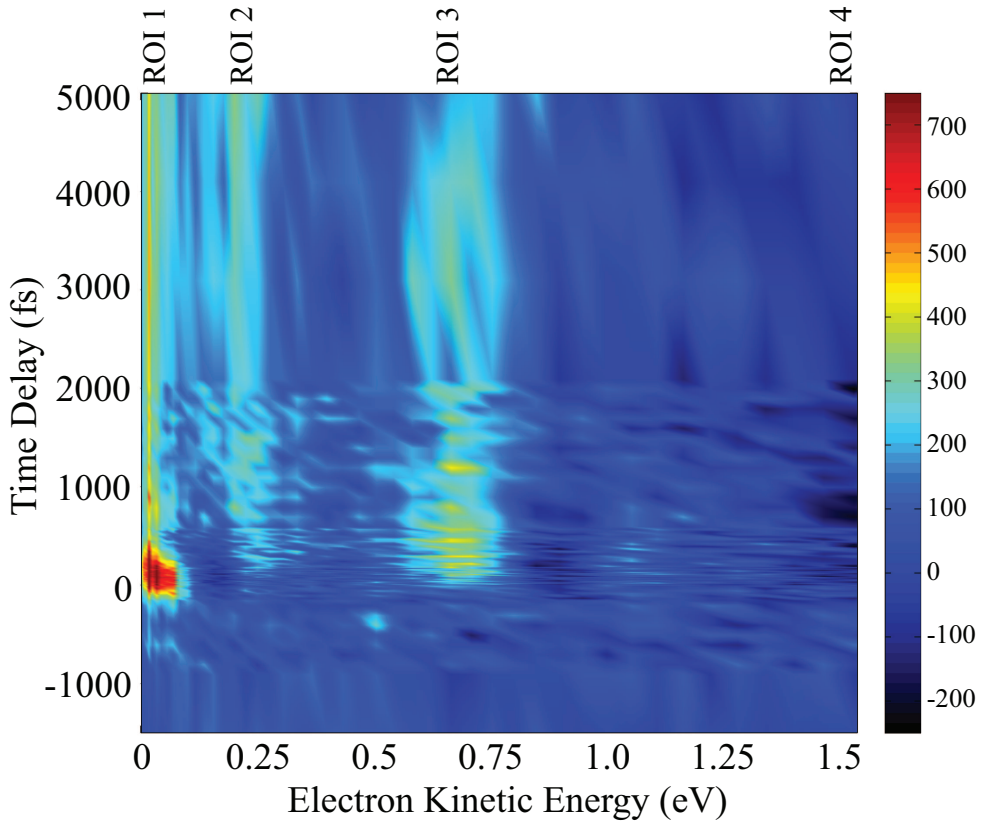

Figure 4.4: A zoomed in region of the time-resolved photoelectron spectrum given in Figure 4.3 is presented here. The energy axis is chosen to reflect the energetically accessible products that are probed with the 805 nm probe pulse. Electrons with kinetic energy up to 1.54 eV are expected. Three atomic products are observed with electron kinetic energies of 0.67 eV, 0.20 eV, and 0.02 eV, which correspond to ${}^3D^\circ_J$, $4p^1\ {}^5P^\circ_J$ and $3d^1\ {}^3D^\circ_J$ neutral atomic fragments, respectively.

4.3.2 Assignment of the Long Time Photoelectron Spectrum

The neutral photoproducts are the result of the predissociation of SESs to give atomic excited states, which are probed with the time delayed 805 nm pulse. Given the energy of the probe pulse, atomic species with binding energies less than 1.54 eV are detectable with a single 805 nm photon. There is no multiphoton ionization of ground state molecular O_2 observed with the 805 nm probe pulse. The long time photoelectron spectrum (PES) is plotted in Figure 4.5 and constructed by temporal integration of the time-resolved photoelectron spectrum from time-delays spanning 441 fs to 105.09 ps. The PES is plotted versus binding energy to aid in the identification of the atomic products. The time range is chosen to eliminate the strong signals observed at early times at low electron kinetic energies that are attributed

to the transiently populated SES. Similar results are observed when the entire time axis is integrated, but the intensity of the lowest kinetic energy feature is artificially high due to the overlapping signals. No attempt has been made to quantify the relative intensities of the signals since the degeneracies of the atomic fragments that are probed are expected to be different and the ionization cross sections of the excited atomic fragments are not known.

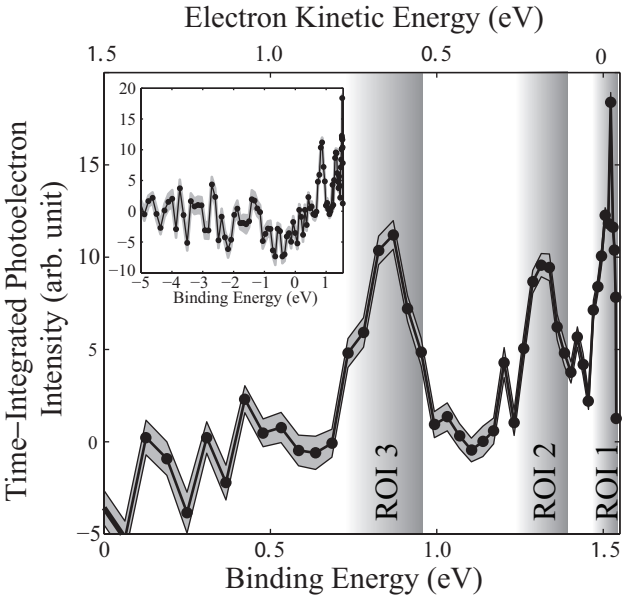

Figure 4.5: The time-integrated photoelectron spectrum is given here with uncertainties represented by the gray shaded region surrounding the solid black trace. Delays from 441 fs to 105.09 ps are integrated to make the spectrum. Photoelectron lines from excited atomic fragments are observed at 0.87 eV, 1.34 eV, and 1.52 eV, which correspond to $4d^1\ ^3D^\circ_J$, $4p^1\ ^5P^\circ_J$ and $3d^1\ ^3D^\circ_J$ states with expected binding energies of 0.86 eV, 1.33 eV and 1.53 eV, respectively. The inset shows 'negative' binding energies (or higher kinetic energies) to illustrate that two-photon transitions from the 805 nm probe pulse are not observed.

Since a typical atomic fluorescence lifetime is on the order of hundreds of picoseconds to nanoseconds, the signals from atomic excited states do not decay significantly on the time-scales measured here. Atomic signals are observed with electron kinetic energies of 0.67 eV, 0.20 eV, and 0.02 eV (binding energies of 0.87 eV, 1.34 eV, and 1.52 eV) which correspond to $O^*\ 2s^22p^3(^4S^\circ)4d^1\ ^3D^\circ_J$, $O^*\ 2s^22p^3(^4S^\circ)4p^1\ ^5P^\circ_J$ and $O^*\ 2s^22p^3(^4S^\circ)3d^1\ ^3D^\circ_J$ fragments, respectively.[56] The fine structure of each atomic excited states is not resolved in this experiment because the splitting is small compared to the resolution of the VMI spectrometer and the probe laser pulse spectral width.[56] In the remainder of this chapter, the atomic ion core configuration will be

neglected when identifying each atomic product in favor of a more concise nomenclature that describes only the outermost valence electron and the term symbol of the state, ie: $nl^1\ ^S L^\circ_J$.

Photoelectron signals from the $4s\sigma_g$ $v = 0$, $4s\sigma_g$ $v = 1$, and $3d\sigma_g$ $v = 1$ SESs that are probed with the delayed 805 nm pulse are expected at kinetic energies of 0.05 eV, 0.05 eV and 0.03 eV, respectively, when the vibrational quantum number is conserved upon ionization to the final $c\ ^4\Sigma^-_u$ ion state (ie: $v = v'$). These signals are not resolved from one another; they also overlap spectrally with the photoelectron signal from the $3d^1\ ^3D^\circ_J$ atomic fragment. Additionally, the $4s\sigma_g$ $v = 1$ can be probed to the $v = 0$ level of the $c\ ^4\Sigma^-_u$ ion core, which would eject photoelectrons with kinetic energies of 0.24 eV. This ionization channel might overlap energetically with the signal from the $4p^1\ ^5P^\circ_J$ atomic fragment with electron kinetic energy of 0.20 eV. These overlapping signals will be explored in greater detail when the time dependence of the signals is discussed below; additional selectivity is obtained by using the observed time dependencies of the atomic and molecular SESs. At long time delays, the decay of the SESs is expected to be fast compared to the radiative lifetimes of the atomic fragments. The high-harmonic pulse is not energetic enough to generate an excited fragment and an atomic ion, so the origin of the excited atomic fragments must be from neutral dissociation of the SESs. This conclusion is also based on static fluorescence measurements where excited atomic fragments are detected as neutral dissociation products of SESs.[35,36,103] Thus, the origin of the atomic fragments observed here is attributed to the neutral predissociation of $4s\sigma_g$ $v = 0$, $4s\sigma_g$ $v = 1$, and $3d\sigma_g$ $v = 1$ SESs.

In the ion core dissociation model the excited electron rapidly adjusts to follow the ion core dissociation; at some point during the fragmentation, the excited electron of the molecule is localized on a single atom where the principal quantum number from the molecular state is preserved in the atomic state produced. Probing the time scale over which the electron localization occurs will be discussed in a future work exploring the photoelectron angular distributions. The time scale over which the electronic excitation is localized on a dissociating atomic fragment has previously been studied in I_2^- [114] by monitoring the angular distributions versus time.

In contrast to this simple picture, previous results studying dispersed fluorescence of the excited atomic fragments in the UV spectral range indicate that the $ns\sigma_g$ SESs will preferentially form ns^1 and $(n-1)d^1$ fragments while $nd\sigma_g$ SESs will form $(n+1)s^1$ and nd^1 atomic oxygen products.[36] In this proposed model, the effective quantum number, $n^* = n - \mu_l$, is conserved rather than the principal quantum number (here μ_l is the angular momentum dependent quantum defect). This is in contrast to the previous work of Ukai[35] that shows a conservation of the principal quantum number upon dissociation. Additionally, a similar dispersed fluorescence experiment[103] measuring visible/near-infrared emission from the neutral atomic fragments detects np^1 fragments that are not observed in the UV fluorescence experiment presumably due to radiative cascades from higher lying states that emit outside the detection

window. Additionally, the visible fluorescence results[103] suggest a reassignment of the principal quantum numbers of the *nd* SESs in contradiction to the assignment of Ukai et al., Hikosaka et al. and Liebel et al.[35,36,99] The discrepancy in the assignment of the *nd* series and the propensity rules that describe the neutral dissociation product distributions limit the definitive correlations of atomic fragments measured here to the particular SESs from which they originate. Using previous reports of the neutral product distribution and the ion core dissociation model, no consistent and unambiguous assignment can be made. Additionally, an assessment has to be made as to the validity of the ion core dissociation model in describing the SESs excited in this experiment since valence electrons might play an important role as well.

Some assumptions made here include adopting the prevalent assignments of the $nl\sigma_g$ SESs from Ukai et al., Hikosaka et al. and Liebel et al.[35,36,99] Since UV dispersed fluorescence measurements do not directly observe np^1 fragments, it is assumed that those results might be influenced by fluorescence cascades.[36] Thus, the fragment propensity rules that have been previously formulated might not describe the predissociation of SESs at these low values of n. In fact, the present observation of $4d^1\ {}^dD_J^\circ$ fragments is at odds with the propensity rules since the SESs excited here should not produce $4d^1$ fragments as a dominant channel. The only fragments one might expect from these rules are $4s^1$ and $3d^1$ SESs, which are clearly not the only fragments observed in the present experiment (see Figure 4.5) or in the the visible/near-infrared dispersed fluorescence.[103] The original interpretation of Ukai[35] has been adopted that assumes the principal quantum number is conserved upon neutral dissociation.

It should be noted that the ionization probe pulse is somewhat low in energy and might not be sensitive to the complete set of neutral dissociation products. Future experiments using a higher energy probe pulse (say 400 nm light rather than 805 nm) is desirable to ensure that the only products formed are the ones detected here. Despite this limitation, there are clearly at least three neutral products that agree well with known binding energies of atomic excited states. Using these assumptions, the fragments can be tentatively correlated to the SESs from which they originated.

Using the simple ion core dissociation model, the $3d^1\ {}^3D_J^\circ$ fragment is tentatively assigned to the predissociation of the $3d\sigma_g\ v = 1$ SES because the principal quantum number is conserved and there exist only one $3l\sigma_g$ SES populated by the harmonic pump pulse (see Figure 4.2). This assignment incidentally follows the propensity rules of Liebel et al.[36] (ie:$3d\sigma_g \rightarrow 3d^1$), but these rules indicate that the $3d^1\ {}^3D_J^\circ$ fragment might also be attributable to dissociation of the excited $4s\sigma_g$ SESs. Future work is needed to confirm the postulated origin of this fragment.

Since two $4s\sigma_g$ states are populated, it is expected from the ion core dissociation model that the atomic fragments would have a $4l^1$ excited electron. Indeed, the remaining identified atomic signals are $4d^1\ {}^3D_J^\circ$ and $4p^1\ {}^5P_J^\circ$ states. Identifying which SES produces the specific product is not possible with this spectral measurement alone; however, using the time-resolution afforded by this experimental configuration permits a correlation of the products to the SESs from which they originate by

correlating lifetimes extracted from the time-dependent signals. These spectral measurements appear to support the ion core dissociation model illustrated in Figure 4.1 as described by Ukai et al.[35] in that the principal quantum number, n, appears to be conserved upon predissociation of the molecular SES to atomic products. This is discussed further below.

4.3.3 Transient Photoelectron Signals

A critical aspect to the ion core dissociation model is that the character of the excited state should not influence the SES lifetime. This means that the decay lifetimes of the $4s\sigma_g$ $v = 1$ and $3d\sigma_g$ $v = 1$ should be identical in the limit that the excited electron is non-interacting, or in other words, that the ion core dynamics are fast compared to autoionization. By probing the temporal development of the atomic products the SES responsible for each $4l^1$ atomic fragment can be assigned based the time scales that the products appear. The transient photoelectron signal is determined by integration of a range of photoelectron energies, or regions of interest (ROIs), and plotting the result versus time delay. The signals are globally fit to a simple kinetic model to describe the time-dependent signals. The results are illustrated in Figure 4.6 where several regions of interest are plotted with the kinetic fits overlaid; the results are also tabulated in Table 4.1.

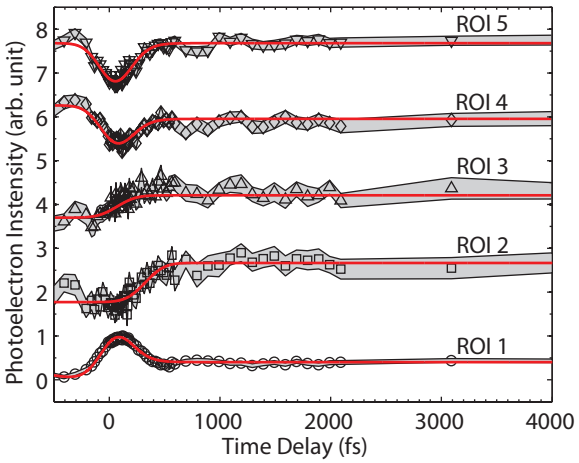

Figure 4.6: The transient photoelectron signal observed from integrating energetic regions of interested described in the text and summarized in Table 4.1. Only the time delays taken in the range of -500 fs to 4000 fs are shown here; time delays up to +105.09 ps were measured with no significant change in the observed transient behavior. The regions of interest, the assignment of each region, the kinetic energy range integrated over to yield the transient signals and, the fit functions used to quantify the dynamics are summarized in Table 4.1.

ROI	Assignment	Kinetic Energy Range (eV)	Fit Function
1	$nl\sigma_g\ v=1$ / $3d^1\ ^3D_J^\circ$	0 - 0.14	Eq 4.2+4.3
2	$4p^1\ ^5P_J^\circ$	0.14 - 0.55	Eq 4.3
3	$4d^1\ ^3D_J^\circ$	0.55 - 0.90	Eq 4.3
4	$B\ ^2\Sigma_g^-$	1.41 - 2.95	Eq 4.2+4.3
5	$b\ ^4\Sigma_g^-$	3.72 - 6.70	Eq 4.2

Table 4.1: Regions of interest (ROIs) are given along with the electron kinetic energy regions that are integrated. The regions are also described in terms of the identity of the products that contribute to the transient signals shown in Figure 4.6. The fit functions used to fit the transient signals are also given.

General Considerations

General aspects of the time resolved signals will be addressed here before the results of the curve fitting are discussed. This includes details pertaining to the instrumental response function and the effect of a vibrational or rotational coherent signal on the observed transients. Additionally, the thought process used in defining the global fitting routine is briefly outlined. Finally, an assessment of overlapping depletion signals on the transient signals is given.

The instrumental cross-correlation, σ_{cc}, is found to be 97 ± 3 fs from a separate pump-probe ionization experiment of $1s^13p^1$ states in atomic helium.[27,67] The excitation is instantaneous and the observed signal is described by a step function convolved with the Gaussian instrumental response, which yields an error function. This signal is fit to the error function with the assumption that the radiative decay lifetime of the resonance in helium is much longer than the measured time delays. This is a valid assumption as the fluorescence decay of helium is many nanoseconds and the delays sampled here only measure up to 105.09 ps.

Coherent pumping of the vibrational SESs is considered before an accurate kinetic model is described. The splitting between the $4s\sigma_g\ v=0$ and $4s\sigma_g\ v=1$ states shown in Figure 4.2 is 0.19 eV. If the states are coherently excited to form a vibrational wavepacket, the expected beat period would be on the order of 22 fs, much faster than the present experiment can resolve in time. However, since the energy gap between the states is large compared to the probe pulse spectral width, the two vibrational levels are not probed to the same final state with the same electron kinetic energy and thus, will not interfere. This means that a coherent signal from the superposition of these two states will not be observed.

Considering now the possible superposition and interference of the $4s\sigma_g\ v=0$ and $3d\sigma_g\ v=1$ SESs, there exists a possibility that both states can be probed to the

same final ion core ($v = 0$), ejecting an electron with the same kinetic energy (within the spectral width of the probe pulse). This coherence will beat with a period of 207 fs. The decay of the coherence is determined by the lifetimes of the individual states coherently populated. Specifically, the wavepacket will decay with a lifetime related to the average of the spectral line widths, and this is estimated to be on the order of 50 fs assuming that the natural line widths of the ion state represent the decay of the SES as a first approximation. In this instance, the decay of the coherence is limited by the predissociation lifetime of the $3d\sigma_g$ $v = 1$ state which is on the order of 70 fs.[36–39,41,99–102] Considering that the decay is considerably faster than the instrumental time resolution, coherent effects will not be clearly resolved in time with this experiment. This also means that the coherence will never experience a complete oscillation and will have a temporal signature composed of the instrumental time resolution convolved with the ~ 50 fs exponential decay.

The amplitude of the coherent signal is composed of the transition dipole matrix elements connecting the ground state to each SES in the superposition, represented as A_v^e. The ionization cross sections connecting each SES to the same final ion state are represented by A_v^i and also contribute to the total coherent signal amplitude. Using previously determined FC factors[105] one can write the coherence amplitude as a product of the four individual matrix elements weighted by the FC factors. Assuming that the electronic parts of the individual amplitudes are the same allows the known FC factors to provide a rough estimate of the coherent signal amplitude. The FC factor to populate the $v = 0$ SES is defined as unity while the FC factor to form the $v = 1$ SES is 0.42.[105] Similarly, in probing an SES with a change in vibrational quantum number, it is assumed to have the same FC weightings. This results in a total amplitude that is written as $A_0^e \times A_1^e \times A_0^i \times A_1^i = 1 \times 0.42 \times 1 \times 0.42 = 0.18$. This means that the coherent part of the total signal with electron kinetic energy centered at $\sim$ 0.05 eV is composed of approximately 9% coherent signal. This estimate neglects the formation of neutral products ($3d^1\ ^3D_J^\circ$) that also contribute to the total signal since their contribution is not precisely known. This means that the $\sim 9\%$ coherence signal is at most an upper limit to the contribution of the total signal. Since the uncertainity in the measurement of the low electron kinetic energy feature is slightly larger than the estimated contribution, the likelihood of observing the coherent part of the total signal is small. For this reason, in an effort to simplify the fitting functions used to describe the photoelectron transient behavior, the coherence terms are negelected. Other features that might also show influences from the coherence, such as the neutral product signals, have much higher uncertainities associated with them, on the order of $10\% - 20\%$. This means that the effects of the small coherence term can be safely negelcted as a first approximation. Future experiments with better signal to noise and time-resolution might be able to observe this wavepacket.

Rotational wavepackets are also neglected since the O_2 sample is used at room temperature and not is cooled extensively by the effusive expansion into the vacuum chamber. This makes it difficult to observe a coherent rotational population in the ex-

cited state. Additionally, the timescales for a rotational revival are much longer[115,116] than the femtosecond dynamics observed in here (ie: in Figure 4.6).

The fitting results of regions of interest are reported below are obtained by a global fitting routine, where fit parameters are shared between related signals, such as the instrumental response and lifetimes, where appropriate. A global fit usually requires some a priori insight into what the signals physically mean. This can incorporate a certain degree of bias towards what the results might be by linking signals that may not naturally be correlated. To address this, rather than fit the data globally from the start, a free fit of the data was first performed. This result showed that all the signals have similar instrumental responses, as one would expect. These coefficients are then shared between all the transient functions and the fit reoptimized. Next, signals with lifetimes that are within the fit uncertainty are linked to one another and the optimization is once again performed. These are the only parameters globally shared in the results below and will be described in detail as each ROI is addressed. A wide range of starting values were chosen to avoid fitting data to a local minimum rather than the global minimum.

Since the projected photoelectron images are used in forming the transient photoelectron signals, the effect of energetically higher lying photoelectron depletion signals on the lower kinetic energy transients must be assessed. To assess this contribution, a simulated photoelectron image is created with an isotropic electron distribution, just as was done when the same effect was addressed in the assignment of the photoelectron spectrum (see Section 4.3.1). As before, the radius of this distribution is defined to be energetically centered at the photoelectron signal for the $B\ ^2\Sigma_g^-$ ion state. When a SES is ionized in the pump-probe measurement, the signal at this energy is depleted as compared to images where the SES is not probed. Additional signals are generated at radii that represent atomic and molecular photoproducts to assess the effect of the overlapping depletion on these transient signals. Once again it is estimated that the $4d^1\ ^3D_J^\circ$ signal (ROI 3) is overlapped with at most $\sim 17\%$ of the maximum intensity of the $B\ ^2\Sigma_g^-$ direct ionization signal. This is the case when both signals are present with equal intensity, which is not observed in the experiment (see Figures 4.3 and 4.4). The depletion signal is estimated to be more than a factor of two smaller in intensity because depletion signals are generally much harder to measure in a pump-probe experiment.

The $\sim 17\%$ overlap thus represents an upper limit to the effect of overlapping states due to the VMI projections from higher electron kinetic energy features, just as was concluded for the effect of overlapping states on the long time photoelectron spectrum. A reasonable estimate based on the relative intensities is expected to be smaller than $\sim 10\%$. Considering the typical uncertainties associated with ROI 2 and ROI 3 are on the order of $10\% - 20\%$, which limit the positive identification, or for that matter the influence, of the depletion features on the observed transients at low electron kinetic energy. As such, the effect of overlapping depletion signals from the $B\ ^2\Sigma_g^-$ ion state is negelected in the fitting of neighboring ROIs.

In a similar vein of thought, the overlapping signal from the $^2\Pi_u$ ion state is neglected in the kinetic fits that are detailed below. This is because the lower excitation cross section to this states is on the order of ten times smaller than neighboring ion states.[105] Due to the difficulty in measuring a depletion signal, this factor of ten severely limits its observation and is expected to only slightly perturb the transient signals. This is quantified in the curve fitting of ROI 2 that is described below. The results of the global fit will be presented below and are discussed in a different numerical order (ie: not linearly from ROI 1 to ROI 5) to present a discussion that groups related dynamics together.

Fit Results and Discussion

The signal in ROI 1 is attributed to the sum of two overlapped transients; specifically, the signal represents the excitation and decay of at least one SES transient and the neutral $3d^1\ ^3D_J^\circ$ product that was assigned by the long time photoelectron spectrum. Exactly what values of n and l contribute to this signal, or for that matter how many SES signals contribute to this ROI, is not known. Due to this ambiguity, the decay lifetimes of the individual states cannot be fit; instead it is assumed that the SES signal is dominated by a single contribution with one lifetime, or alternatively, it can be thought of as a sum of signals from multiple SES with the same decay lifetime. This is a reasonable approximation based on the ion core dissociation model since the two populated $v = 1$ SESs are be expected to have the same decay lifetime in the limit that autoionization is slow compared to neutral predissociation of the ion core. In other words, the excited electron is non-interacting in the ion core dissociation model, so the predissociation relaxation channel will dominate. The SES transient signal, $S_{ses}(t)$, is described by first order kinetics (ie: a single exponential) that is convolved with the instrumental response and given by[117]

$$S_{ses}(t) = A \times Exp\left[\frac{-(t-t_0)}{\tau_{ses}} + \frac{\sigma_{cc}^2}{2\tau_{ses}^2}\right] \times \left\{1 + Erf\left[\frac{1}{\sqrt{2}}\left[\frac{(t-t_0)}{\sigma_{cc}} - \frac{\sigma_{cc}}{\tau_{ses}}\right]\right]\right\} + b \tag{4.2}$$

where A is a free fit amplitude, t_0 is the time at which the decay is initiated, τ_{ses} is the SES decay lifetime, σ_{cc} is the instrumental cross correlation, and b is a vertical offset. The SES transient signal is then superimposed on neutral $3d^1\ ^3D_J^\circ$ product production as assigned with the long time photoelectron spectrum. The temporal development of atomic products is also described by first order kinetics and written as

$$\begin{aligned} S_{nd}(t) = A \times (1 + Erf\left[\frac{1}{\sqrt{2}}\frac{(t-t_0)}{\sigma_{cc}}\right] - Exp\left[\frac{\sigma_{cc}^2 - 2\tau_{ses}(t-t_0)}{2\tau_{ses}^2}\right] \\ \times Erfc\left[\frac{1}{\sqrt{2}}\frac{\tau_{ses}(t-t_0) - \sigma_{cc}^2}{\sigma_{cc}\tau_{ses}}\right]) + b. \end{aligned} \tag{4.3}$$

Since the neutral products are a result of the decay of a SES, the product formation lifetime is identical to the SES decay lifetime. ROI 1 is then fit to the sum of Equations 4.2 and 4.3. Since the decay of the SES in ROI 1 and the atomic fragment product rise are overlapped spectrally and temporally, a definitive value of the product rise lifetime is not extracted, but the expectation of what it might be based on the ion core dissociation model is suggested below.

The fit yields $\tau_{ses} = 65 \pm 5$ fs. This lifetime agrees very well with the predissociation lifetime reported in previous high resolution measurements and theoretical predictions for the $v = 1$ vibrational level of the $c\ ^4\Sigma_u^-$ ion core.[36–39,41,99–102] This suggests that the dominant SES signal observed in ROI 1 is from a $nl\sigma_g$ $v = 1$ SES and that neutral dissociation from these states dominates the total SES lifetime since the observed value agrees so favorably with high-resolution measurements. However, the value of n and l contributing to this signal, or for that matter how many states contribute to this rise and decay, cannot be determined.

Since the $3d^1\ ^3D_J^\circ$ fragment was tentatively assigned as a photoproduct of the $3d\sigma_g$ $v = 1$ SES, in the framework of the ion core dissociation model, the neutral product should have a corresponding product rise lifetime of 65 ± 5 fs. This lifetime is not measured directly in this work; the free fit lifetime of the neutral product rise in this ROI has a large uncertainty reflecting the difficulty in quantitatively extracting individual lifetimes from overlapping signals. For the purposes of these results, the product rise is linked to the the SES decay based on the expectations of the ion core model. This is meant to reflect the *expectations* of the signal lifetime based on the ion core dissociation model and not to be confused with a directly measured lifetime. The results are not altered in a statistically significant way if the product rise lifetime is not linked to the SES decay, indicating that the value of the product rise lifetime is not critically dependent on the lifetime to which it is fit.

The signal represented by ROI 3 is fit to the functional dependence given by Equation 4.3. This region is attributed to, based on the photoelectron spectrum, the temporal development of the $4d^1\ ^3D_J^\circ$ neutral fragment. Here the product rise is best fit to a lifetime of 65 ± 5 fs indicating this product is most likely from the other populated $v = 1$ SES, specifically, the $4s\sigma_g$ $v = 1$ SES. This is because if neutral predissociation dominates the decay of a vibrational SES, the nature of the excited electronic excitation is not important as the ion core predissociaiton dictates the SES lifetime. In this limit, one can begin to correlate the neutral photoproducts observed to the SES from which they form based on the observed lifetimes and quantum number.

Since the lifetime of the $v = 1$ SES signal in ROI 1 and product rise signal in ROI 3 agree so favorably with high-resolution measurements and theoretical predictions of the $v = 1$ ionic state lifetime,[36–39,41,99–102] it appears that the role of the excited electron in the $v = 1$ SESs is, as expected from the ion core dissociation model, a spectator to the bond breaking. The present experimental results cannot comment on the relative intensities of the fragments, but the observed timescale implies that the

rate of autoionization is slower than dissociation since the ion core kinetics appear to dominate the lifetime of the $v = 1$ SES.

Next, ROI 2 represents the production of the $4p^1\ ^5P_J^\circ$ atomic product based on the assignment from the long time photoelectron spectrum. This is assumed to be a dissociation product of the $4s\sigma_g$ $v = 0$ SES by a process of elimination, since the other two observed fragments have already been correlated to the $v = 1$ vibrational SES. Additionally, when this fragment is fit to Equation 4.3 a product rise lifetime is found to be 427 ± 75 fs, which differs significantly from the previous two ROI that are thought to represent the dynamics of a $v = 1$ SES based on the similar timescales. The predicted and measured lifetime of the $v = 0$ ion state is thought to be on the order of 10 to 100 times larger than the $v = 1$ SES,[37–41,99,99,101] so the fact that the presently observed product formation lifetime is as large as 427 ± 75 fs is not surprising and supports the tentative correlation of the $4p^1\ ^5P_J^\circ$ fragment to the $4s\sigma_g$ $v = 0$ SES.

Since ROI 2 overlaps energetically with the unobserved $^2\Pi_u$ depletion signal, the effect of an overlapping depletion from this ion state on the time resolved transient must be assessed. As was discussed in the previous section, the intensity of the higher electron kinetic energy depletion signals and that of the $^2\Pi_u$ depletion signal are not expected to significantly influence the transient signals. To be assured of this, a separate fit was performed where a depletion signal was incorporated into the fit function for ROI 2. Specifically, the sum of Equation 4.3 and 4.2 was fit to ROI 2 where the amplitude of Equation 4.2 was defined to represent a depletion signal (ie: it is negative). The lifetime of the depletion recovery is defined to match the SES decay lifetime of the $v = 1$ SES, since when probing a SES the depletion recovery should mirror the dynamics of the SES decay. The result of this fit yields a product formation lifetime of 352 ± 98, which, within the uncertainty of the fit, is indistinguishable from the lifetime where the depletion was not incorporated. Additionally, the amplitude of the depletion portion of the fit is approximately the same magnitude as the product production amplitude, which is not a physically meaningful outcome. This is because the depletion signals clearly observed at higher electron kinetic energy have amplitudes that are smaller that the fit amplitude of the unobserved $^2\Pi_u$ depletion signal.

Additionally, the expected signal from the $4s\sigma_g$ $v = 1$ SES that is probed to the $v = 0$ ion core of the $c\ ^4\Sigma_u^-$ state might be spectrally overlapped with atomic products ROI 2. This signal would be a positive feature in the time-resolved photoelectron spectrum and would be initiated at t_0. The lifetime of the $v = 1$ SES signal was found to be 65 ± 5 fs, so the expected signal $4s\sigma_g$ $v = 1$ that is probed to the $v = 0$ ion state would be akin to that of the SES signal in ROI 1. No such feature is observed in the time-resolved signal for ROI 2. It is not clear why this signal is absent, though it might be a result of FC factors on the pump and probe steps since the vibrational levels change upon each step of pump-probe process.[105] A similar argument was already made for why a vibrational wavepacket is not observed.

The possibility exists that the $4p^1\ ^5P_J^\circ$ signal is actually the $4s\sigma_g$ $v = 1$ SES that is

probed to the $c\ ^4\Sigma_u^-$ $v = 0$ ion state. This is ruled out on the basis of two arguments. First, the $v = 1$ ion core has a predissociation lifetime estimated to be on the order of 60 fs to 70 fs[36–39,41,99–102] (measured here to be 65 ± 5 fs), and since the signal in ROI 2 is observed to persist at time delays up to 105.09 fs, it seems unlikely that the signal represented by ROI 2 is the the result of a SES. Second, the total signal would appear as a slow product rise representing the $4p^1\ ^5P_J^\circ$ fragment that evolves somewhat slowly in time with a shoulder at early times representing the population and decay of the $4s\sigma_g$ $v = 1$ SES. There is no observed signal at early time delays near t_0. This 'missing' feature should be a topic of investigation of future experimental efforts.

Previous work measuring neutral product fluorescence does not detect $4p^1\ ^5P_J^\circ$ fragments in the UV spectral range,[35] most likely due to fluorescence cascades from this high lying state to lower lying $^5S_J^\circ$ or $^5D_J^\circ$ atomic states in the visible to near-infrared regions of the spectrum. This is exemplified by experiments identifying $3p^1\ ^5P_J^\circ$ atomic states as a reaction product of these SESs that have be reported by observing visible/near-infrared fluorescence.[103] The visible/near-infrared fluorescence results do not directly support the observation of the $4p^1\ ^5P_J^\circ$ atomic fragment made here. They however, do not contradict the present observation since fluorescence from $4p^1\ ^5P_J^\circ$ states to the $3s^1\ ^5S_2^\circ$ state is expected at 386 nm, which is outside their detection window.[56,103]

It should also be noted that the observed neutral products are not necessarily the complete set of products from the dissociation. This is because three limiting factors exist in this experiment. Namely, the probe pulse photon energy (1.54 eV) is low enough that all the formed fragments might not be ionized based on energetic considerations. Also, the resolution of the VMI spectrometer and the spectral width of the probe pulse might not be able to resolve energetically nearby signals. By integrating ROIs, as was performed here, some of these signals might be lumped together. This potential problem might be alleviated by experiments that have better signal-to-noise so that finer slices of the time-resolved photoelectron spectrum can be taken while preserving reasonable uncertainties. This is likely a difficult task considering the present experimental data was collected continuously for approximately 6 days; to improve the signal-to-noise by a factor of two requires at least four times longer integration time.

Previous work probing SESs in N_2 measure similar results in that fluorescence cascades can complicate the understanding of the relaxation channels and nascent product distributions.[84] Since the $4s\sigma_g$ $v = 0$ is expected to be the only other SES populated to an appreciable extent, the production of $4p^1\ ^5P_J^\circ$ atomic fragments is likely best assigned as a dissociation product the $4s\sigma_g$ $v = 0$ SES. It should also be noted that the principal quantum number is conserved in the dissociation as would be expected from the ion core dissociation model.[35]

The signal in ROI 4 represents the depletion of the $B\ ^2\Sigma_g^-$ autoionization signal. It is observed that the depletion does not, in the time scales probed here, recover

completely. Since the depletion signal represents an excited state that is probed and thus not allowed to autoionize, the lack of a complete depletion recovery implies that a long lived state is probed at long time delays. The identity of this state is not revealed by the measurement. It is not clear if the depletion signal is from a very long lived SES or from some intermediate state that has not previously been observed. It is unlikely that the persisting depletion signal is a result of an SES given the predissociation lifetimes of the ion core measured and predicted in previous work, which would limit the maximum decay lifetime of the potential long lived SES to approximately 10 ps.[36–39,41,99–102]

Given that the identity of the long lived depletion is not positively assigned, a similar kinetic model to that used to describe ROI 1 is adopted. Once again, the overlap of the two signals prevent the unambiguous identification of the long lived depletion rise lifetime, if one exists. It is possible that the depletion signal is directly and instantaneously formed by the pump pulse, which lives for at least hundreds of picoseconds. On the other hand it might be populated indirectly by some other unobserved process.

The signal in ROI 4 is found to have a fast exponential recovery lifetime representing the recovery of the $v = 1$ SESs probed here, namely, it is found to be 65 ± 5 fs. The second part of the fit function represents what appears to be a long lived molecular state that is not identified. No effort has been made to extract a lifetime for this state or in measuring the rate at which the signal is formed since nothing is known about this state and because the convolution of the two signals limits the observation of the early time dynamics. To the best of our knowledge, this feature has not previously been observed in static measurements. Future work is needed to address this puzzling feature.

The feature in ROI 5 is assigned to the depletion and recovery of the $b\ ^4\Sigma_g^-$ autoionization signal. This transient signal is fit to Equation 4.2. There is no other observed decay or product production superimposed on this transient that is observable with the given signal-to-noise. The autoionization recovery is fit to a single exponential lifetime of 65 ± 5 fs indicating the the electrons that would have autoionized to this state if the probe pulse had not interacted with the sample are entirely from the $v = 1$ SES.

It is worth noting that the $v = 1$ SESs have autoionization contributions to both the $B\ ^2\Sigma_g^-$ and $b\ ^4\Sigma_g^-$ states whereas the $v = 0$ SES does not appear to contribute any autoionization signal to the $b\ ^4\Sigma_g^-$ electron yield. In other words, the $v = 0$ SES does not appear to decay, to a detectable extent, to the $b\ ^4\Sigma_g^-$ ion core. The reason for this is not clear and requires future theoretical and experimental attention. One possibility that might explain this is that the $v = 0$ state is not probed by the low energy 805 nm probe pulse such that an autoionization depletion signal would never be observed for any of the ion cores energetically accessible. In this case, only the neutral products from the $v = 0$ states would be detected. This does not seem a likely possibility as there is a long lived depletion signal that does not have any obvious

connection to the pair of $v = 1$ SESs, and based on the energetics of ionization from the $v = 0$ state, the transition should be allowed. Another explanation is that the $v = 0$ preferentially autoionizes to energetically lower lying, not currently measured, ion cores. Electrons from autoionization to lower ion cores are ejected with far more kinetic energy than can be projected on to the detector while preserving spectral resolution for the low kinetic energy electrons. In the current work, these depletion signals are not measured. The origin of the difference can only be speculated on without separate experiments to extract the autoionization branching preferences by detecting the autoionization depletion signals in time for all ion cores energetically accessible. Additionally, the suspected presence of a long lived intermediate might be addressed in a more quantitative way.

The results here show that femtosecond time-resolved experiments provide complementary information to high-resolution experiments that study the decay of SESs in the frequency domain. The time-resolution allows for the tentative correlation of SESs to atomic fragments using the ion core dissociation model. This technique avoids fluorescence cascades that might complicate the fragment fluorescence spectrum in a static measurement.[35,36,99,103] The nascent products detected here are $3d^1\ {}^3D^\circ_J$, $4d^1\ {}^3D^\circ_J$, and $4p^1\ {}^5P^\circ_J$ atomic fragments. The lifetimes of product formation for the $4d^1\ {}^3D^\circ_J$, and $4p^1\ {}^5P^\circ_J$ atomic fragments are in good agreement with static measurements probing the predissociation lifetime of the ion core.[36–39,41,99–102] The timescales obtained here can be compared to future theoretical calculations that study low n-SESs to gain insight into the excited electron interactions on the excited state decay dynamics. Future experiments might probe the system with enhanced time resolution and with higher probe pulse energies to determine if the products detected here are the complete set of neutral fragments and to determine the timescales for product production of all fragments unambiguously.

4.4 Conclusions

Superexcited $c\ {}^4\Sigma^-_u\ nl\sigma_g\ v = 0, 1$ resonances in molecular O_2 are excited with a single high-order harmonic pump pulse centered at 23.10 eV. The prepared states are tracked in time with a delayed 805 nm (1.54 eV) probe pulse to ionize SESs and to detect the nascent neutral atomic products ejected from photodissociation. The $4d^1\ {}^3D^\circ_J$ atomic product is found to be formed on a timescale of 65 ± 5 and is most likely a product of the $4s\sigma_g\ v = 1$ SES based on the ion core dissociation model. The $3d^1\ {}^3D^\circ_J$ fragment is observed spectrally, but the formation cannot be tracked versus time due to overlap with the decay of $v = 1$ SES signal. The observed time scales of the signals related to the $v = 1$ SESs are in good agreement with the most recent high-resolution measurements of the predissociation line width of the ion core to which the SESs converge to, suggesting the SES decay is dominated by the bond breaking of the ion core.[35–39,41,99–103,107–112] The $4p^1\ {}^5P^\circ_J$ product is produced on a

time scale of 427 ± 75 fs and is tentatively attributed to the predissociation product of the $4s\sigma_g$ $v = 0$ SES.

A long lived depletion signal in the autoionization yield to the $B\ ^2\Sigma_g^-$ ion core is also observed. The related positive feature is not identified in the present work, though the possibility that it is a very long lived SES is ruled out based on the predissociation lifetimes of the ion core from previous measurement.[36–39,41,99–102] The origin of this feature requires future experiments and theoretical attention. Future work addressing SESs in polyatomic systems might consider additional decay channels through conical intersections. These molecular funnels may compete more efficiently with the autoionization channels since the Born-Oppenheimer approximation does not apply and facile surface crossings are possible.[33]

Bibliography

[1] Lovelock, K. R. J.; Villar-Garcia, I. J.; Maier, F.; Steinruck, H.-P.; Licence, P. *Chem. Rev.* **2010**, *110*, 5158–5190.

[2] Neumark, D. M. *Annu. Rev. Phys. Chem.* **2001**, *52*, 255–277.

[3] Stolow, A.; Bragg, A. E.; Neumark, D. M. *Chem. Rev.* **2004**, *104*, 1719–1758.

[4] Kimura, K.; Katsumata, S.; Achiba, Y.; Yamazaki, T.; Iwata, S. *Hanbook of HeI Photoelectron Spectra of Fundamental Organic Molecules*; Japan Scientific Societies Press: Tokyo, 1981.

[5] Weightman, P. *Rep. Prog. Phys.* **1982**, *45*, 753–814.

[6] Williams, R. H.; Srivastava, G. P.; McGovern, I. T. *Rep. Prog. Phys.* **1980**, *43*, 1357–1414.

[7] Smith, S. J.; Leuchs, G. In *Advances in Atomic and Molecular Physics*; Bates, S. D., Benjamin, B., Eds.; Academic Press, 1988; Vol. Volume 24; pp 157–221.

[8] Cooper, J.; Zare, R. N. *J. Chem. Phys.* **1968**, *48*, 942.

[9] Cooper, J.; Zare, R. N. *Lect. Theor. Phys.* **1968**, *11C*, 317.

[10] Aymar, M.; Robaux, O. *J. Phys. B-At. Mol. Opt. Phys.* **1979**, *12*, 531–546.

[11] Chien, R. L.; Mullins, O. C.; Berry, R. S. *Phys. Rev. A* **1983**, *28*, 2078–2084.

[12] Ederer, D. L. *Phys. Rev. A* **1971**, *4*, 2263.

[13] Ederer, D. L.; Parr, A. C.; West, J. B.; Holland, D.; Dehmer, J. L. *Phys. Rev. A* **1982**, *25*, 2006–2011.

[14] Fano, U. *Phys. Rev.* **1961**, *124*, 1866.

[15] Fano,; Dill, D. *Phys. Rev. A* **1972**, *6*, 185.

[16] Fano, U.; Cooper, J. W. *Phys. Rev.* **1965**, *137*, 1364.

[17] Flemming, M. G.; Wu, J. Z.; Caldwell, C. D.; Krause, M. O. *Phys. Rev. A* **1991**, *44*, 1733–1740.

[18] Leuchs, G.; Smith, S. J. *Phys. Rev. A* **1985**, *31*, 2283–2290.

[19] Manson, S. T.; Starace, A. F. *Rev. Mod. Phys.* **1982**, *54*, 389–405.

[20] Matthias, E.; Zoller, P.; Elliott, D. S.; Piltch, N. D.; Smith, S. J.; Leuchs, G. *Phys. Rev. Lett.* **1983**, *50*, 1914–1917.

[21] Mies, F. H. *Phys. Rev.* **1968**, *175*, 164.

[22] Mullins, O. C.; Chien, R. L.; Hunter, J. E.; Jordan, D. K.; Berry, R. S. *Phys. Rev. A* **1985**, *31*, 3059–3067.

[23] Mullins, O. C.; Chien, R. L.; Hunter, J. E.; Keller, J. S.; Berry, R. S. *Phys. Rev. A* **1985**, *31*, 321–328.

[24] Kerling, C.; Bowering, N.; Heinzmann, U. *J. Phys. B-At. Mol. Opt. Phys.* **1990**, *23*, L629–L635.

[25] Wills, A. A.; Sokell, E.; Gorczyca, T. W.; Feng, X.; Wiedenhoeft, M.; Canton, S. E.; Berrah, N. *J. Phys. B-At. Mol. Opt. Phys.* **2002**, *35*, L367–L374.

[26] Siegel, A.; Ganz, J.; Bussert, W.; Hotop, H. *J. Phys. B-At. Mol. Opt. Phys.* **1983**, *16*, 2945–2959.

[27] Haber, L. H.; Doughty, B.; Leone, S. R. *Phys. Rev. A* **2009**, *79*, 031401.

[28] Haber, L. H.; Doughty, B.; Leone, S. R. *J. Phys. Chem. A* **2009**, *113*, 13152–13158.

[29] Haber, L. H.; Doughty, B.; Leone, S. R. *Molec. Phys.* **2010**, *108*, 1241–1251.

[30] Shore, B. W. *Phys. Rev.* **1968**, *171*, 43.

[31] Codling, K.; Madden, R. P. *Phys. Rev. A* **1971**, *4*, 2261.

[32] Codling, K.; Madden, R. P. *J. Res. Nat. Bur. Stand. Sect. A. Phys. Chem.* **1972**, *A 76*, 1.

[33] Domcke, W.; Yarkony, D. R.; Köppel, H. *Conical Intersections: Electronic Structure, Dynamics & Spectroscopy*; Advanced Series in Physical Chemistry; World Scientific Publishing Co. Pte. Ltd.: Singapore, 2004; Vol. 15.

[34] Horio, T.; Fuji, T.; Suzuki, Y.-I.; Suzuki, T. *J. Am. Chem. Soc.* **2009**, *131*, 10392–10393.

[35] Ukai, M.; Machida, S.; Kameta, K.; Kitajima, M.; Kouchi, N.; Hatano, Y.; Ito, K. *Phys. Rev. Lett.* **1995**, *74*, 239–242.

[36] Liebel, H.; Lauer, S.; Vollweiler, F.; Muller-Albrecht, R.; Ehresmann, A.; Schmoranzer, H.; Mentzel, G.; Schartner, K. H.; Wilhelmi, O. *Phys. Lett. A* **2000**, *267*, 357–369.

[37] Liebel, H.; Ehresmann, A.; Schmoranzer, H.; Demekhin, P. V.; Lagutin, B. M.; Sukhorukov, V. L. *J. Phys. B-At. Mol. Opt. Phys.* **2002**, *35*, 895–905.

[38] Ehresmann, A.; Werner, L.; Klumpp, S.; Schmoranzer, H.; Demekhin, P. V.; Lagutin, B. M.; Sukhorukov, V. L.; Mickat, S.; Kammer, S.; Zimmermann, B.; Schartner, K. H. *J. Phys. B-At. Mol. Opt. Phys.* **2004**, *37*, 4405–4422.

[39] Padmanabhan, A.; et al., *Journal of Physics B: Atomic, Molecular and Optical Physics* **2010**, *43*, 165204.

[40] Tanaka, K.; Yoshimine, M. *J. Chem. Phys.* **1979**, *70*, 1626–1633.

[41] Evans, M.; Stimson, S.; Ng, C. Y.; Hsu, C. W. *J. Chem. Phys.* **1998**, *109*, 1285–1292.

[42] Schoenlein, R. W.; Chattopadhyay, S.; Chong, H. H. W.; Glover, T. E.; Heimann, P. A.; Shank, C. V.; Zholents, A. A.; Zolotorev, M. S. *Science* **2000**, *287*, 2237–2240.

[43] Hoener, M. et al. *Phys. Rev. Lett.* **2010**, *104*, 253002.

[44] Cryan, J. P. et al. *Phys. Rev. Lett.* **2010**, *105*, 083004.

[45] Fang, L. et al. *Phys. Rev. Lett.* **2010**, *105*, 083005.

[46] Uiberacker, M. et al. *Nature* **2007**, *446*, 627–632.

[47] Sansone, G. et al. *Nature* **2010**, *465*, 763.

[48] Drescher, M.; Hentschel, M.; Kienberger, R.; Uiberacker, M.; Yakovlev, V.; Scrinzi, A.; Westerwalbesloh, T.; Kleineberg, U.; Heinzmann, U.; Krausz, F. *Nature* **2002**, *419*, 803–807.

[49] Baltuska, A.; Udem, T.; Uiberacker, M.; Hentschel, M.; Goulielmakis, E.; Gohle, C.; Holzwarth, R.; Yakoviev, V. S.; Scrinzi, A.; Hansch, T. W.; Krausz, F. *Nature* **2003**, *421*, 611–615.

[50] Abel, M. J.; Pfeifer, T.; Nagel, P. M.; Boutu, W.; Bell, M. J.; Steiner, C. P.; Neumark, D. M.; Leone, S. R. *Chem. Phys.* **2009**, *366*, 9–14.

[51] Corkum, P. B. *Phys. Rev. Lett.* **1993**, *71*, 1994.

[52] Brabec, T.; Krausz, F. *Rev. Mod. Phys.* **2000**, *72*, 545.

[53] Kobayashi, T.; Shirakawa, A. *J. Lumin.* **2000**, *87-89*, 119–120.

[54] Eppink, A.; Parker, D. H. *Rev. Sci. Instrum.* **1997**, *68*, 3477–3484.

[55] Li, W.; Chambreau, S. D.; Lahankar, S. A.; Suits, A. G. *Rev. Sci. Instrum.* **2005**, *76*, 7.

[56] Ralchenko, Y.; Kramida, A. E.; Reader, J.; Team, N. A. NIST Atomic Spectra Database (version 3.1.5). 2008.

[57] Loh, Z. H.; Khalil, M.; Correa, R. E.; Leone, S. R. *Rev. Sci. Instrum.* **2008**, *79*, 13.

[58] Vrakking, M. J. J. *Rev. Sci. Instrum.* **2001**, *72*, 4084–4089.

[59] Smeenk, C.; Arissian, L.; Staudte, A.; Villeneuve, D. M.; Corkum, P. B. *J. Phys. B-At. Mol. Opt. Phys.* **2009**, *42*, 5.

[60] Roberts, G. M.; Nixon, J. L.; Lecointre, J.; Wrede, E.; Verlet, J. R. R. *Rev. Sci. Instrum.* **2009**, *80*, 7.

[61] Renth, F.; Riedel, J.; Temps, F. *Rev. Sci. Instrum.* **2006**, *77*, 12.

[62] Garcia, G. A.; Nahon, L.; Powis, I. *Rev. Sci. Instrum.* **2004**, *75*, 4989–4996.

[63] Braun, A.; Drabbels, M. *Rev. Sci. Instrum.* **2005**, *76*, 10.

[64] Dribinski, V.; Ossadtchi, A.; Mandelshtam, V. A.; Reisler, H. *Rev. Sci. Instrum.* **2002**, *73*, 2634–2642.

[65] Taylor, K. T. *J. Phys. B-At. Mol. Opt. Phys.* **1977**, *10*, L699–L704.

[66] Dill, D. *Phys. Rev. A* **1973**, *7*, 1976–1987.

[67] Strasser, D.; Pfeifer, T.; Hom, B. J.; Muller, A. M.; Plenge, J.; Leone, S. R. *Phys. Rev. A* **2006**, *73*, 4.

[68] Kaminski, H.; Kessler, J.; Kollath, K. J. *Phys. Rev. Lett.* **1980**, *45*, 1161–1164.

[69] Schohl, S.; Cherepkov, N. A.; Petrov, I. D.; Sukhorukov, V. L.; Baier, S.; Hotop, H. *J. Phys. B-At. Mol. Opt. Phys.* **1998**, *31*, 3363–3385.

[70] Gessner, O.; Lee, A. M. D.; Shaffer, J. P.; Reisler, H.; Levchenko, S. V.; Krylov, A. I.; Underwood, J. G.; Shi, H.; East, A. L. L.; Wardlaw, D. M.; Chrysostom, E. T.; Hayden, C. C.; Stolow, A. *Science* **2006**, *311*, 219–222.

[71] Reid, K. L. *Annu. Rev. Phys. Chem.* **2003**, *54*, 397–424.

[72] Seideman, T. *Annu. Rev. Phys. Chem.* **2002**, *53*, 41–65.

[73] Rau, A. R. P. *Phys. Scr.* **2004**, *69*, C10–C13.

[74] Collin, S.; Vincent, G.; Haidar, R.; Bardou, N.; Rommeluere, S.; Pelouard, J.-L. *Phys. Rev. Lett.* **2010**, *104*, 027401.

[75] Faist, J.; Capasso, F.; Sirtori, C.; West, K. W.; Pfeiffer, L. N. *Nature* **1997**, *390*, 589–591.

[76] Golde, D.; Wagner, M.; Stehr, D.; Schneider, H.; Helm, M.; Andrews, A. M.; Roch, T.; Strasser, G.; Kira, M.; Koch, S. W. *Phys. Rev. Lett.* **2009**, *102*, 127403.

[77] Kobayashi, K.; Aikawa, H.; Katsumoto, S.; Iye, Y. *Phys. Rev. Lett.* **2002**, *88*, 256806.

[78] Kroner, M.; Govorov, A. O.; Remi, S.; Biedermann, B.; Seidl, S.; Badolato, A.; Petroff, P. M.; Zhang, W.; Barbour, R.; Gerardot, B. D.; Warburton, R. J.; Karrai, K. *Nature* **2008**, *451*, 311–314.

[79] Madhavan, V.; Chen, W.; Jamneala, T.; Crommie, M. F.; Wingreen, N. S. *Science* **1998**, *280*, 567–569.

[80] Mukherjee, S.; Sobhani, H.; Lassiter, J. B.; Bardhan, R.; Nordlander, P.; Halas, N. J. *Nano Letters* **2010**, *10*, 2694–2701.

[81] Wang, Z. M.; Elliott, D. S. *Phys. Rev. A* **2000**, *62*, 053404.

[82] Yuan, Z. S.; Zhu, L. F.; Liu, X. J.; Zhong, Z. P.; Li, W. B.; Cheng, H. D.; Xu, K. Z. *Phys. Rev. A* **2002**, *66*, 8.

[83] Stener, M.; Decleva, P.; Lisini, A. *J. Phys. B-At. Mol. Opt. Phys.* **1995**, *28*, 4973–4999.

[84] Strasser, D.; Haber, L. H.; Doughty, B.; Leone, S. R. *Molec. Phys.* **2008**, *106*, 275–280.

[85] Knight, P. L.; Lauder, M. A.; Dalton, B. J. *Phys. Rep.-Rev. Sec. Phys. Lett.* **1990**, *190*, 1–61.

[86] Saloman, E. B. *J. Phys. Chem. Ref. Data* **2007**, *36*, 215–386.

[87] Gokhberg, K.; Averbukh, V.; Cederbaum, L. S. *J. Chem. Phys.* **2007**, *126*, 6.

[88] Gilb, S.; Nestorov, V.; Leone, S. R.; Keske, J. C.; Nugent-Glandorf, L.; Grant, E. R. *Phys. Rev. A* **2005**, *71*, 8.

[89] Gilb, S.; Torres, E. A.; Leone, S. R. *J. Phys. B-At. Mol. Opt. Phys.* **2006**, *39*, 4231–4238.

[90] Zamith, S.; Bouchene, M. A.; Sokell, E.; Nicole, C.; Blanchet, V.; Girard, B. *Eur. Phys. J. D* **2000**, *12*, 255–261.

[91] Magunov, A. I.; Rotter, I.; Strakhova, S. I. *Phys. Rev. B* **2003**, *68*, 245305.

[92] Mercouris, T.; Komninos, Y.; Nicolaides, C. A. *Phys. Rev. A* **2007**, *75*, 013407.

[93] Wickenhauser, M.; Burgdorfer, J.; Krausz, F.; Drescher, M. *Phys. Rev. Lett.* **2005**, *94*, 023002.

[94] Wickenhauser, M.; Burgdorfer, J.; Krausz, F.; Drescher, M. *J. Mod. Opt.* **2006**, *53*, 247–257.

[95] Zhao, Z. X.; Lin, C. D. *Phys. Rev. A* **2005**, *71*, 060702.

[96] Seaton, M. J. *Rep. Prog. Phys.* **1983**, *46*, 167–257.

[97] Lagutin, B. M.; Sukhorukov, V. L.; Petrov, I. D.; Schmoranzer, H.; Ehresmann, A.; Schartner, K. H. *J. Phys. B-At. Mol. Opt. Phys.* **1994**, *27*, 5221–5239.

[98] Srivastava, S. K.; Trajmar, S. *J. Phys. B-At. Mol. Opt. Phys.* **1978**, *11*, 3433–3438.

[99] Hikosaka, Y.; Lablanquie, P.; Ahmad, M.; Hall, R. I.; Lambourne, J. G.; Penent, F.; Eland, J. H. D. *J. Phys. B-At. Mol. Opt. Phys.* **2003**, *36*, 4311–4326.

[100] Liebel, H.; Muller-Albrecht, R.; Lauer, S.; Vollweiler, F.; Ehresmann, A.; Schmoranzer, H. *J. Phys. B-At. Mol. Opt. Phys.* **2001**, *34*, 2581–2596.

[101] Demekhin, F. V.; Omel'yanenko, D. V.; Lagutin, B. M.; Sukhorukov, V. L.; Werner, L.; Ehresmann, A.; Schartner, K. H.; Schmoranzer, H. *Russ. J. Phys. Chem. B* **2007**, *1*, 213–221.

[102] Demekhin, P. V.; Omel'yanenko, D. V.; Lagutin, B. M.; Sukhorukov, V. L.; Werner, L.; Ehresmann, A.; Schartner, K. H.; Schmoranzer, H. *Opt. Spectrosc.* **2007**, *102*, 318–329.

[103] Karawajczyk, A.; Erman, P.; Rachlew-Kallne, E.; Riu, J. R. I.; Stankiewicz, M.; Franzen, K. Y.; Veseth, L. *Phys. Rev. A* **2000**, *61*, art. no.–032718.

[104] Luna, H.; McGrath, C.; Shah, M. B.; Johnson, R. E.; Liu, M.; Latimer, C. J.; Montenegro, E. C. *Astrophys. J.* **2005**, *628*, 1086–1096.

[105] Baltzer, P.; Wannberg, B.; Karlsson, L.; Gothe, M. C.; Larsson, M. *Phys. Rev. A* **1992**, *45*, 4374–4384.

[106] Hikosaka, Y.; Aoto, T.; Hall, R. I.; Ito, K. *J. Phys. B-At. Mol. Opt. Phys.* **2003**, *36*, 1423–1432.

[107] Lafosse, A.; Brenot, J. C.; Golovin, A. V.; Guyon, P. M.; Hoejrup, K.; Houver, J. C.; Lebech, M.; Dowek, D. *J. Chem. Phys.* **2001**, *114*, 6605–6617.

[108] Lafosse, A.; Brenot, J. C.; Guyon, P. M.; Houver, J. C.; Golovin, A. V.; Lebech, M.; Dowek, D.; Lin, P.; Lucchese, R. R. *J. Chem. Phys.* **2002**, *117*, 8368–8384.

[109] Vandermeulen, P.; Krause, M. O.; Delange, C. A. *Phys. Rev. A* **1991**, *43*, 5997–6009.

[110] Leblanc, F. J. *J. Chem. Phys.* **1963**, *38*, 487.

[111] Richardviard, M.; Dutuit, O.; Aitkaci, M.; Guyon, P. M. *J. Phys. B-At. Mol. Opt. Phys.* **1987**, *20*, 2247–2254.

[112] Frasinski, L. J.; Randall, K. J.; Codling, K. *J. Phys. B-At. Mol. Opt. Phys.* **1985**, *18*, L129–L135.

[113] Beebe, N. H. F.; Thulstrup, E. W.; Andersen, A. *J. Chem. Phys.* **1976**, *64*, 2080–2093.

[114] Mabbs, R.; Pichugin, K.; Sanov, A. *J. Chem. Phys.* **2005**, *123*, 8.

[115] Tsubouchi, M.; Whitaker, B. J.; Wang, L.; Kohguchi, H.; Suzuki, T. *Phys. Rev. Lett.* **2001**, *86*, 4500–4503.

[116] Dantus, M.; Bowman, R. M.; Zewail, A. H. *Nature* **1990**, *343*, 737–739.

[117] Pedersen, S.; Zewail, A. H. *Molec. Phys.* **1996**, *89*, 1455–1502.